JOINT INSTITUTE FOR AERONAUTICS AND ACOUSTICS

NASA/CR-97-208349

National Aeronautics and
Space Administration
Ames Research Center

Stanford University

JIAA TR 120

EXPERIMENTS IN AIRCRAFT ROLL-YAW CONTROL USING FOREBODY TANGENTIAL BLOWING

Nelson Pedreiro

Department of Aeronautics and Astronautics
Stanford University
Stanford, CA 94305

November 1997

Abstract

Advantages of flight at high angles of attack include increased maneuverability and lift capabilities. These are beneficial not only for fighter aircraft, but also for future supersonic and hypersonic transport aircraft during take-off and landing. At high angles of attack the aerodynamics of the vehicle are dominated by separation, vortex shedding and possibly vortex breakdown. These phenomena severely compromise the effectiveness of conventional control surfaces. As a result, controlled flight at high angles of attack is not feasible for current aircraft configurations. Alternate means to augment the control of the vehicle at these flight regimes are therefore necessary.

The present work investigates the augmentation of an aircraft flight control system by the injection of a thin sheet of air tangentially to the forebody of the vehicle. This method, known as Forebody Tangential Blowing (FTB), has been proposed as an effective means of increasing the controllability of aircraft at high angles of attack. The idea is based on the fact that a small amount of air is sufficient to change the separation lines on the forebody. As a consequence, the strength and position of the vortices are altered causing a change on the aerodynamic loads. Although a very effective actuator, forebody tangential blowing is also highly non-linear which makes its use for aircraft control very difficult.

In this work, the feasibility of using FTB to control the roll-yaw motion of a wind tunnel model was demonstrated both through simulations and experimentally. The wind tunnel model used in the experiments consists of a wing-body configuration incorporating a delta wing with 70-degree sweep angle and a cone-cylinder fuselage. The model is equipped with forebody slots through which blowing is applied. There are no movable control surfaces, therefore blowing is the only form of actuation. Experiments were conducted at a nominal angle of attack of 45 degrees. A unique apparatus that constrains the model to two degrees-of-freedom, roll and yaw, was designed and built. The apparatus was used to conduct dynamic experiments which showed that the system was unstable, its natural motion divergent.

A model for the unsteady aerodynamic loads was developed based on the basic physics of the flow and results from flow visualization experiments. Parameters of the aerodynamic model were identified from experimental data. The model was validated using data from dynamic experiments. The aerodynamic model completes the equations of motion of the system which were used in the design of control laws using blowing as the only actuator. The unsteady aerodynamic model was implemented as part of the real-time vehicle control system. A control strategy using asymmetric blowing was demonstrated experimentally.

A discrete vortex method was developed to help understand the main physics of the flow. The method correctly captures the interactions between forebody and wing vortices. Moreover, the trends in static loads and flow structure are correctly represented.

Flow visualization results revealed the vortical structure of the flow to be asymmetric even for symmetric flight conditions. The effects of blowing, and roll and yaw angles on the flow structure were determined. It is shown that superimposing symmetric and asymmetric blowing has a linearizing effect on the actuator characteristics. Transient responses of roll and yaw moments to step input blowing were characterized, and their differences were explained based on the physical mechanisms through which these loads are generated.

Acknowledgments

This work has been supported by the Joint Institute for Aeronautics and Acoustics, between the Department of Aeronautics and Astronautics of Stanford University and the NASA Ames Research Center, under Grant NCC 2-55.

Contents

List of Figures

List of Tables

~

List of Symbols

$\boldsymbol{A}$	state transition matrix of linearized system
$\boldsymbol{B}$	input transmission matrix of linearized system
A_F	flowmeter cross-sectional area
A_j	area of the forebody slot through which blowing is applied
AR	wing aspect ratio, b^2/S_{ref}
b	wing span
c	radius of the vehicle cross-section in the circle plane
C_B	linearized actuator gain, $\frac{\partial C_l}{\partial \Delta C_\mu}$
C_F	friction coefficient characterizing the effect of the bearings and the potentiometer of the roll subsystem
C_l	roll moment coefficient, $\frac{\text{roll moment}}{q_\infty S_{ref} b}$
$C_{l_{dm}}$	roll moment due to direct jet momentum
C_n	yaw moment coefficient, $\frac{\text{yaw moment}}{q_\infty S_{ref} b}$
$C_{n_{wj}}$	yaw moment due to wall-jet effect
C_p	pressure coefficient, $\frac{p-p_\infty}{q_\infty}$
C_ϕ	static stability derivative, $\frac{\partial C_l}{\partial \phi}$
C_γ	static stability derivative, $\frac{\partial C_l}{\partial \gamma}$
$C_{\dot{\phi}}$	dynamic stability derivative, $\frac{\partial C_l}{\partial \dot{\phi}}$
$C_{\dot{\gamma}}$	dynamic stability derivative, $\frac{\partial C_l}{\partial \dot{\gamma}}$
$C_{\ddot{\phi}}$	dynamic stability derivative, $\frac{\partial C_l}{\partial \ddot{\phi}}$
C_μ	jet momentum coefficient, $\frac{\dot{m}_j V_j}{q_\infty S_{ref}}$
$C_{\mu_{CMD}}$	commanded value of the jet momentum coefficient

$C_{\mu_{MIN}}$	minimum value of asymmetric blowing used in the closed-loop control logic
$C_{\mu_{SYM}}$	jet momentum coefficient for symmetric blowing, *i.e.* blowing on both sides of the forebody
D	wind tunnel model fuselage diameter
D_B	linearized actuator gain, $\frac{\partial C_n}{\partial \Delta C_\mu}$
D_F	friction coefficient characterizing the effects of the bearings and the potentiometer of the yaw subsystem
D_ϕ	static stability derivative, $\frac{\partial C_n}{\partial \phi}$
D_γ	static stability derivative, $\frac{\partial C_n}{\partial \gamma}$
$D_{\dot{\phi}}$	dynamic stability derivative, $\frac{\partial C_n}{\partial \dot{\phi}}$
$D_{\dot{\gamma}}$	dynamic stability derivative, $\frac{\partial C_n}{\partial \dot{\gamma}}$
$D_{\ddot{\gamma}}$	dynamic stability derivative, $\frac{\partial C_n}{\partial \ddot{\gamma}}$
g	acceleration of gravity (9.81 m/sec^2)
I_A	inertia of the model support system about the γ-axis
I_M	inertia characteristics of the wind tunnel model with respect to reference frame $X_M Y_M Z_M$ with origin at point P
k_F	flowmeter calibration constant
$\boldsymbol{K}$	gain matrix obtained from LQR design
K_G	coefficient characterizing the gravity restoring moment
K_T	coefficient characterizing the moment about the γ-axis due to the air-supply tubing
L	coordinate along the longitudinal axis of the wind tunnel model with origin at the tip of the forebody and positive towards the rear of the model (same as η)
L/D	distance from a given cross-section of the wind tunnel model from the tip of the forebody measured in terms of wind tunnel model fuselage diameter
$\dot{m}_j$	jet mass flow rate
M_ϕ	moment about the ϕ-axis
M_ϕ^A	aerodynamic moment about the ϕ-axis
M_ϕ^{AS}	static aerodynamic moment about the ϕ-axis
M_ϕ^T	moment about the ϕ-axis caused by the air-supply tubing

M_{ϕ}^{F}	moment about the ϕ-axis caused by friction on the bearings and potentiometer
M_{γ}	moment about the γ-axis
M_{γ}^{A}	aerodynamic moment about the γ-axis
M_{γ}^{AS}	static aerodynamic moment about the γ-axis
M_{γ}^{T}	moment about the γ-axis caused by the air-supply tubing
M_{γ}^{F}	moment about the γ-axis caused by friction on the bearings and potentiometer
M_{γ}^{G}	moment about the γ-axis caused by gravity
M_{γ}^{M}	moment about the γ-axis applied by the motor of the active cancellation system
P	point defined by the intersection of the ϕ-axis and the γ-axis
p	pitch rate, or static pressure at a given point
p_{∞}	static pressure at freestream conditions
q	roll rate
q_{∞}	freestream dynamic pressure, $\frac{1}{2}\rho_{\infty}V_{\infty}^{2}$
$\boldsymbol{Q}$	matrix of state weights used in LQR design
Q_k	strength of three-dimensional point source
r	yaw rate
r_c	vortex core radius
$\boldsymbol{R}$	matrix of input weights used in LQR design
s	Laplace transform variable
S_{ref}	reference area (wing plan-form area)
$\boldsymbol{u}$	input vector used in state-space representation of linearized system
U_{∞}	freestream air speed (same as V_{∞})
$\mathbf{v}$	velocity field
ϑ_F	output signal from the flowmeter
V_{axial}	component of the freestream velocity parallel to the longitudinal axis of the vehicle
V_j	jet speed at exit of the plenum
V_x	component of the cross-flow velocity in the x-axis direction
V_y	component of the cross-flow velocity in the y-axis direction

V_∞	freestream air speed (same as U_∞)
$\boldsymbol{x}$	state vector used in state-space representation of linearized system
$X_M Y_M Z_M$	orthogonal reference frame fixed to the wind tunnel model with origin at point P, with the X-axis coincident with the model's longitudinal axis, the Y-axis in the plane of the wings and positive towards the starboard, and the Z-axis given by the cross-product: $\vec{X} \times \vec{Y}$
z	complex variable
α	angle of attack
α_0	nominal incidence angle (angle of attack for $\phi = \gamma = 0$)
β	side slip angle
δ_ϕ	ϕ angle measured from static equilibrium position, $\phi - \phi_E$
δ_γ	γ angle measured from static equilibrium position, $\gamma - \gamma_E$
ΔC_μ	incremental value of jet momentum coefficient
η	coordinate along the longitudinal axis of the wind tunnel model with origin at the tip of the forebody and positive towards the rear of the model (same as L)
ϕ	apparatus first degree-of-freedom (roll)
ϕ_E	value of ϕ at static equilibrium position
ϕ_m	measured value of the angle ϕ
$\phi_m(t)$	measured roll angle time history
$\phi_s(t)$	simulated roll angle time history
$\hat{\phi}$	estimated value of the angle ϕ
ϕ-axis	axis through which the rotation defining the first degree-of-freedom of the apparatus occurs (longitudinal axis of the wind tunnel model)
Φ	velocity potential
γ	apparatus second degree-of-freedom
γ_E	value of γ at static equilibrium position
γ_m	measured value of the angle γ
$\gamma_m(t)$	measured gamma angle time history
$\gamma_s(t)$	simulated gamma angle time history

$\hat{\gamma}$	estimated value of the angle γ
γ-axis	axis through which the rotation defining the second degree-of-freedom of the apparatus occurs
Γ	circulation of two-dimensional point vortex
ν	kinematic viscosity
ν_k	position of vortex k in the circle plane
ν_{-k}	position of image of vortex k in the circle plane
ψ	stream function
ρ_∞	freestream air density
ρ_j	jet air density
Λ	wing leading-edge sweep angle
ω	complex potential
τ_c	convective time
τ_l	time constant characterizing the roll moment response to blowing
τ_n	time constant characterizing the yaw moment response to blowing
τ_{lc}	time constant characterizing the roll moment response to blowing command
τ_{nc}	time constant characterizing the yaw moment response to blowing command
τ_ϕ	time constant associated to the roll moment response to vehicle motion
τ_γ	time constant associated to the yaw moment response to vehicle motion

~

Chapter 1

Introduction

This dissertation presents theoretical and experimental research on the use of forebody tangential blowing to control the roll-yaw motion of aircraft at high angles of attack. Phenomena such as flow separation, vortex shedding and breakdown, which dominate the aerodynamics in the high angle of attack regime, cause the onset of lateral loads and decrease the effectiveness of conventional control surfaces. Consequently, for conventional aircraft, operation in these regimes is difficult or unfeasible. Augmented means of control are therefore necessary for controlled flight at high angles of attack to be achieved. Forebody tangential blowing is a solution to achieve this augmented control.

In this work, the effects of forebody tangential blowing were characterized in detail and the mechanisms through which it works were identified. A basic understanding of the physics of the flow was obtained and used to formulate an unsteady aerodynamic model which includes the effects of blowing and is suitable for the design and implementation of control logic. A control approach has been developed and the feasibility of roll-yaw control at high angles of attack was demonstrated using forebody tangential blowing as the only actuator.

This research was conducted under the Joint Institute for Aeronautics and Acoustics (JIAA) between the Department of Aeronautics and Astronautics of Stanford University and the NASA Ames Research Center from 1992 to 1995.

1.1 Motivation

The potential benefits of flight in the high angle of attack regime include an increase in maneuverability for fighter aircraft and an increase in lift for future supersonic and hypersonic transport aircraft during take-off and landing. However, there are difficulties associated with flight at high angles of attack. The reduction in control authority and simultaneous development of lateral loads cause a lack of controllability of the vehicle which represents the main obstacle for flight at these regimes. As the angle of attack increases, separation occurs both on the leeside of the wing and forebody. As a consequence, conventional control surfaces such as rudder and ailerons, became less effective. For moderate angles of attack, steady symmetric vortices are formed on the leeside of the forebody. As the angle of attack increases, the vortices become asymmetric, and this causes the onset of lateral loads which can cause departure from controlled flight. It is therefore necessary to find alternate means to increase the controllability of the vehicle.

1.2 Flow Control at High Angles of Attack

Several methods have been proposed to alleviate side forces and to increase vehicle controllability both by passive and active flow control techniques. The use of specific forebody geometry, such as a blunt tip, has been proposed to alleviate lateral loads by diffusing the vorticity [1]. Fixed strakes also provide the required alleviation by forcing the separation to occur at the strakes and forcing some symmetry to the flow. Pneumatic means have also been shown to be effective in decreasing lateral loads on the vehicle. In addition to lateral load alleviation, research has shown that increased control authority can be achieved using active flow control. Installing movable strakes as opposed to fixed ones allows some control of the separation over the forebody. In this case not only alleviation can be achieved, but also asymmetry can be introduced and lateral loads generated in a controlled manner [2]. Similar effects can be obtained using pneumatic means. Varying a jet of fluid in both intensity and direction causes changes in flow structure and consequently generates lateral loads that can be used to control the vehicle.

A promising pneumatic technique that uses tangential leading-edge blowing has been studied experimentally [3, 5] and numerically [6, 7]. The method consists of injecting a thin jet of air tangentially to the rounded leading-edge of a wing. Mittleman [8] developed a low order panel method to predict the unsteady aerodynamic loads of wings with leading and side edge separation, and incorporated the effect of tangential leading-edge blowing. Through simulation it was shown that the method could be used to control the oscillatory motion of a low aspect ratio delta wing. Wong [9, 10] experimentally demonstrated the use of this method to control the roll oscillations of a delta wing at 55 degrees angle of attack. Wind tunnel experiments were conducted in which a delta wing model was free to roll and blowing was the only actuator.

Skow [11] investigated the concept of forebody vortex blowing as a means to alter the asymmetric vortices on the leeside of an aircraft forebody. In this case, nozzles located at the leeside of the forebody were used to inject a jet of air directed to the rear of the vehicle. Experimental results showed that the method could generate significant yawing moments for angles of attack between 25 and 55 degrees. Simulations indicated that the method could enhance departure recovery characteristics of aircraft.

Another pneumatic technique is the concept of forebody tangential blowing (FTB), which was used in this work and is illustrated in Figure 1.1. The idea is based on the fact that a small amount of air injected tangentially to the surface is sufficient to cause a change in the separation lines on the forebody. As a consequence, vortex position and strength change, and large lateral loads are generated. The method is effective because small changes introduced in the flow near the tip of the forebody have an amplification effect caused by the vortex growth. Celik and Roberts [12, 13, 14] conducted experimental investigations on the use of forebody tangential blowing as a means to generate side forces on a slender body and on a delta-wing-body combination. They showed that roll moment and side force could be generated for angles of attack from 20 to 50 degrees. Celik *et al* [15, 16] demonstrated that forebody tangential blowing could be used to suppress wing rock of a delta wing-body configuration. Font [17] conducted a numerical

study of forebody tangential blowing on a tangent-ogive cylinder configuration. Solutions of the thin-layer, Navier-Stokes equations were compared to experimental results and used to investigate the mechanisms through which forebody tangential blowing works. Adams [18] used experimental data on the effects of forebody blowing on the static roll and yaw moments to augment the yaw control of a modified VISTA F16 aircraft in simulation. Assumptions were made that blowing provided additional control, and that vehicle characteristics were not affected by blowing. The blowing system was actuated in an on-off mode, and non-linear control laws were derived. Simulation results showed significant improvement in high angle of attack performance.

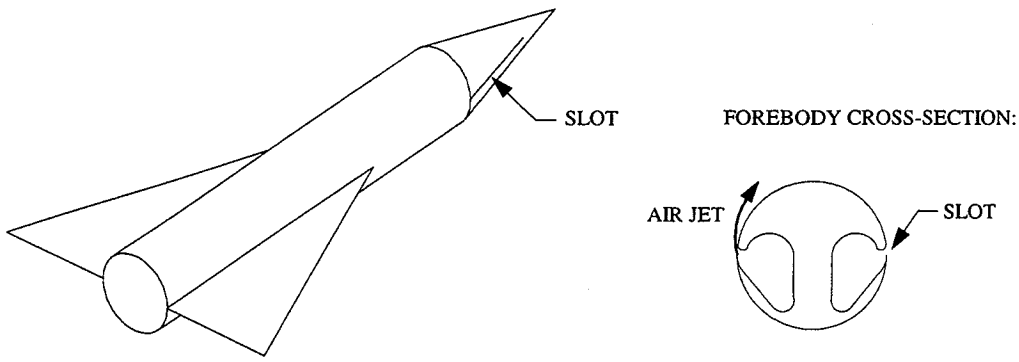

Figure 1.1: Forebody tangential blowing - Concept.

As indicated, previous research showed forebody tangential blowing as an effective actuator being able to generate side force, roll and yaw moments. However, results from previous work are mainly from static experiments and from simulations and do not make clear that FTB can be treated as an incremental effect. It is important to access its impact on the vehicle dynamic characteristics. Also, static experiments revealed that blowing is a highly non-linear effector, but a comprehensive study of how these characteristics vary for various flight conditions did not exist.

This research addressed these issues. The effects of forebody tangential blowing on the flow structure and aerodynamic loads have been fully characterized. Also, the effects of vehicle attitude on the effectiveness of blowing as an actuator were determined. This information was used to formulate an aerodynamic model that includes transient effects and the effects of blowing. The aerodynamic model was then used to develop and implement control logic which uses blowing as the only actuator. The control approach was demonstrated experimentally in the wind tunnel and established the feasibility of using forebody tangential blowing for roll-yaw control at high angles of attack.

1.3 Research Objectives

The main objectives of this research were:

- Obtain a fundamental physical understanding of the aerodynamic loads acting on aircraft at high angles of attack during vehicle maneuvers and in the presence of forebody tangential blowing.

- Demonstrate the feasibility of using forebody tangential blowing for aircraft roll-yaw control at high angles of attack.

In order to achieve these objectives, a model of the aerodynamics that incorporates forebody tangential blowing and includes transient effects was necessary. Moreover, since the main goal was to use blowing to control the vehicle, the aerodynamic formulation had to be suitable for control logic design and real-time implementation. The formulation of such an aerodynamic model required both theoretical and experimental research. In particular, high angle of attack aerodynamics entail some of the unresolved problems in fluid mechanics, such as the onset of symmetric and asymmetric vortices and vortex breakdown. Consequently, given the state of the art of aerodynamic prediction methods, experimental data are necessary to validate numerical results. In this research experiments were conducted to reveal the nature of the flow, characterize the effects of

vehicle attitude and forebody blowing, and support and validate the development of an aerodynamic model.

Driven by the objective of demonstrating the control methods developed, and by the need to conduct dynamic experiments, a unique experimental apparatus was designed and built that allows a wind tunnel model two degrees-of-freedom, roll and yaw. Using the apparatus, dynamic experiments were conducted in which both the natural motion and the closed-loop response of the system were demonstrated.

1.4 Contributions

In meeting the objectives of this research, the following contributions have been made to the understanding of the flow and the control of aircraft in the high angle of attack regime:

- The feasibility of using forebody tangential blowing to control the roll-yaw motion of a delta wing-body model at high angle of attack has been experimentally demonstrated in the wind tunnel.

- A semi-empirical unsteady aerodynamic model, which includes the effects of blowing, has been developed that predicts both static and transient aerodynamic loads acting on the vehicle. The structure of the model was formulated based on the main physics of the flow and experimental observations. The model provides good agreement with experiments, and is suitable for the design of control laws and their real-time implementation.

- A discrete vortex model has been developed that captures the interaction between forebody and wing vortices. The model shows the correct trends in the static aerodynamic loads and provides insight into the main flow structure.

- A unique apparatus has been designed and constructed that constrains a wind tunnel model to two degrees-of-freedom, roll and yaw. Active cancellation of external effects due to the model support system is an integral part of the apparatus. The apparatus was used to perform dynamic experiments which revealed the natural motion of the system, supported the development of the aerodynamic model, and validated the developed control approach.

- Transient response of roll and yaw moments to blowing have been determined. Their characteristics were explained based on the different mechanisms that generate each of these moments.

- It has been demonstrated that the highly non-linear characteristics associated with asymmetric forebody blowing can be linearized by superimposing symmetric and asymmetric blowing.

- It has been shown that forebody tangential blowing affects the characteristics of an aircraft, and that the effects of blowing depend on the vehicle roll and yaw angles. Therefore, the equations of motion of an aircraft incorporating FTB should be viewed as $\dot{x} = f(x,u)$ rather than the more conventional approach $\dot{x} = f(x) + g(u)$.

1.5 Thesis Outline

In this chapter the motivation, objectives and contributions of the research presented in this dissertation have been discussed. The remaining chapters, containing a presentation of the methods, experiments, theoretical developments, and results that form the body of this work, are organized as follows:

The experimental apparatus used in these investigations is described in Chapter 2. The characteristics of the wind tunnel, wind tunnel model, air injection system, and model support system are presented, as well as the sensors and actuators that are an integral part

of the apparatus. Also included is a description of the equipment used for the flow visualization experiments and the measurements of the aerodynamic loads. The equations of motion of the system are derived, and the operation of the apparatus during dynamic experiments is described in detail. The goals are to make the reader familiar with the capabilities and limitations of the apparatus, and to provide a clear understanding of how the experimental results presented in later chapters were obtained.

Chapter 3 contains a presentation of experimental results aimed at characterizing: (1) the flow over the wind tunnel model, and (2) the effects that vehicle attitude and forebody tangential blowing have on the flow structure and the aerodynamic loads. Results from flow visualization experiments are used to provide insight into the physics of the flow. Transient responses of aerodynamic loads to blowing are presented, and used to provide an understanding of the mechanisms through which forebody tangential blowing works. The natural motion of the two degrees-of-freedom system is presented, and is used to demonstrate the need for control.

In Chapter 4 a steady-state aerodynamic model is derived based on first principles plus the knowledge obtained through experimental observations of the vortical nature of the flow (Chapter 3). The development of a discrete vortex model is presented. It is shown that the model captures the interactions between forebody and wing vortices and provides further understanding of the flow structure and the generation of roll and yaw moments. Although the model has proven to be an invaluable tool in understanding the flow over the vehicle, phenomena such as flow asymmetry for symmetric flight conditions, and vortex breakdown limit its use as a predicting tool.

A semi-empirical model for the unsteady aerodynamic loads is presented in Chapter 5. This model was developed to provide fast prediction of the aerodynamic loads, including transient effects, and is therefore suitable for control law design and real-time implementation. The structure of the model was determined from the basic physics of the flow as observed during the flow visualization experiments. Static aerodynamic loads are

an integral component of this model and can be obtained using the discrete vortex method of Chapter 4 or through measurements. Parameters of the model describing transient effects were determined using data from dynamic experiments and parameter identification techniques. The model was validated against data from dynamic experiments, and provided the necessary formulation required to complete the equations of motion of the system.

In Chapter 6 a control approach that uses forebody tangential blowing as the only actuator to control the roll-yaw motion of the wind tunnel model is presented. The unsteady aerodynamic model was linearized and used to design a control logic that stabilizes the naturally divergent system. This linearized version of the aerodynamic model was also used in the real-time implementation of the control to provide an estimate of the states of the dynamic system. The control approach was demonstrated through a dynamic experiment in the wind tunnel which established the feasibility of using forebody tangential blowing to control the roll-yaw motion of the model.

In Chapter 7 the conclusions of this research are summarized. Recommendations for future work, necessary to further the application of forebody tangential blowing as a means to augment aircraft control in the high angle of attack regime, are also presented.

Appendix A contains information on the detailed geometry and mass properties of the wind tunnel model.

Appendix B contains information on the dimensions and mass properties of the model support system, as well as a list of the sensors and actuators that are an integral part of the experimental apparatus.

Appendix C describes the method used to identify the parameters of the semi-empirical aerodynamic model.

~

Chapter 2

Experimental Apparatus

In this chapter the apparatus used to conduct the experiments reported in this dissertation is described. The objectives are to present the characteristics and capabilities of the apparatus and provide a context for the experimental results discussed in the following chapters. The main characteristics of the wind tunnel facilities and wind tunnel model are presented. The equations of motion for the two degrees-of-freedom model support system are derived. Its main sub-systems are described in detail and their performance evaluated. The air injection system, sensors and actuators, and flow visualization equipment are described. The chapter concludes with an overview of the fundamental components of the real-time control system.

2.1 Wind Tunnel Facilities

The wind tunnel facility of the Aeronautics and Astronautics Department at Stanford University was used for the experiments conducted in this research. It consists of a closed circuit low speed wind tunnel. The top view of the wind tunnel is shown in Figure 2.1. The maximum freestream centerline speed at the test section is 60 m/sec. The air speed is controlled by a variable speed motor to which a variable pitch fan is attached. Screens are located upstream of the test section which reduce the mean turbulence level at the test section to approximately 0.1% [9]. Three independent measurements are made of the

freestream air speed using the reference static pressure difference from two stations in the contraction, and two pitot static tubes located in the test section upstream of the model. For the experiments conducted in this research a nominal freestream speed of 19.5 m/sec was used.

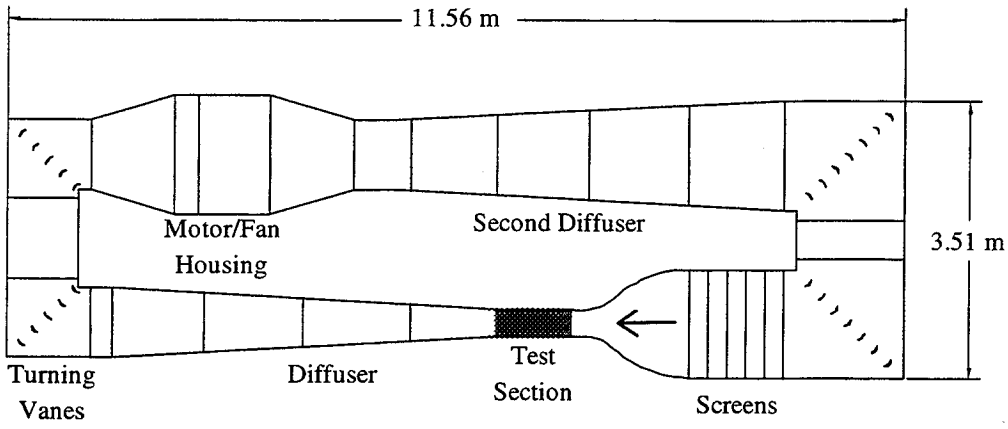

Figure 2.1: Top view of the wind tunnel.

Test section dimensions are: 0.45 m X 0.45 m X 0.91 m, width, height and length respectively. It consists of a welded cast-iron frame. The bottom wall is made of sheet metal and top and side walls are made of plexiglass. The entire section is mounted on a cast-iron cart with castors so that it can be attached or removed from the rest of the wind tunnel. When in place, the test section is bolted to the exit of the tunnel contraction section.

2.2 Wind Tunnel Model

The wind tunnel model used in these experiments consists of a sharp leading-edge delta wing with 70 degrees sweep angle and a cone-cylinder fuselage[1]. This model is shown in

[1] Designed by Dr. Zeki Celik (Research Associate, Aero/Astro Department, Stanford University); machined by Mr. Tom Hasler (Former Aero/Astro Machine Shop, Stanford University).

Figure 2.2, and has no movable control surfaces. Slots through which blowing is applied are located on both sides of the conical section of the forebody. For the experiments conducted in this research, the portions of the slots that extend to the cylindrical section of the forebody were covered from the inside. Air is provided to the forebody plena through flexible tubing that enters the model through the rear end of the fuselage. Tests were conducted at a nominal incidence angle of 45 degrees. Tunnel blockage at this configuration is 7%, including blockage from the model and the model support system. Details on the dimensions and mass properties of the model as well as the geometry of the slots are given in Appendix A.

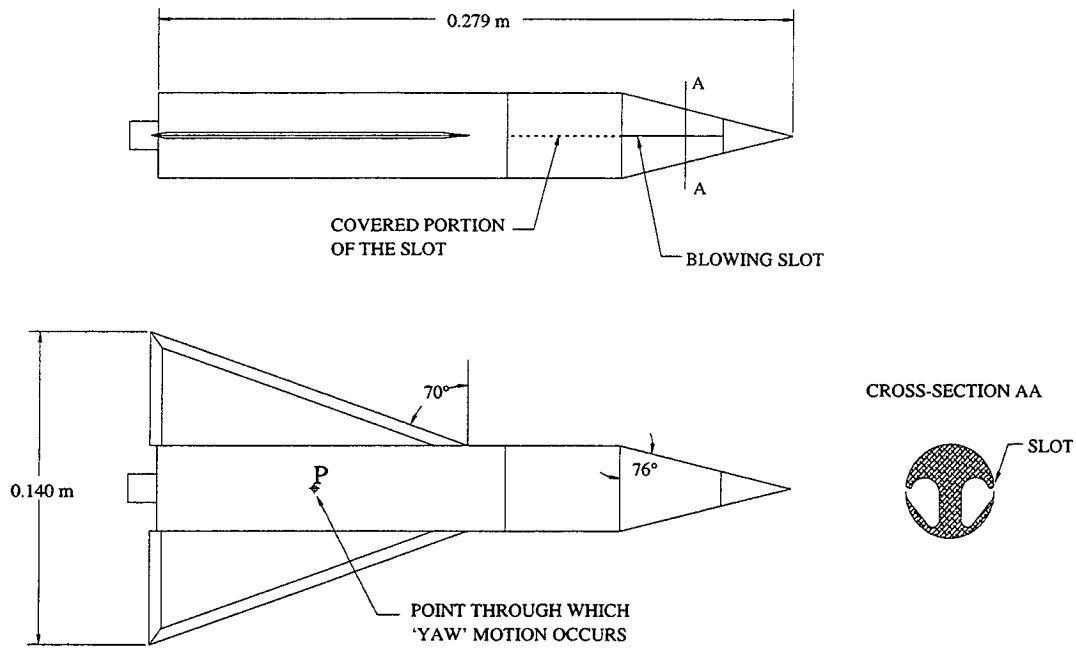

Figure 2.2: Wind tunnel model and detail of forebody slots.

2.3 The Two Degrees-of-Freedom Model Support System

A unique support system was designed and constructed that constrains the model to two degrees-of-freedom[2] [19]. The objective is to approximate the lateral-directional dynamics of an aircraft. Of particular interest is the roll-yaw coupling at high angles of attack. The support system can be divided into two main sub-systems. The first implements the roll degree-of-freedom[3], ϕ, and consists of a shaft mounted on bearings. The wind tunnel model is attached to this roll shaft and hence rotates freely about its longitudinal axis. This entire roll sub-system is mounted on the second sub-system which consists of a mechanical arm that can rotate about an axis perpendicular to the longitudinal axis of the model. This sub-system provides the second degree-of-freedom, γ (Figure 2.3).

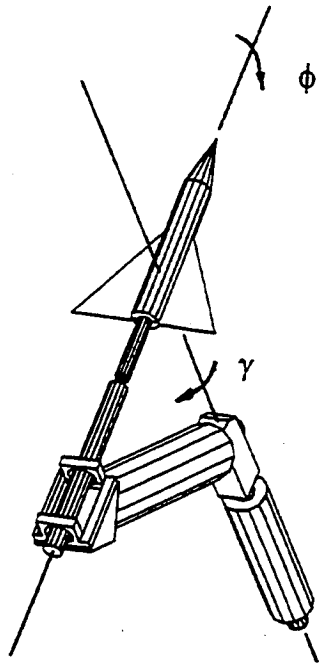

Figure 2.3: Two degrees-of-freedom model support system.

[2] Designed by the author; machined by Mr. Tom Hasler and Mr. Matthew Chuck (Former Aero/Astro Machine Shop, Stanford University).
[3] Roll about the longitudinal axis of the model.

Low friction precision potentiometers[4] are used to measure ϕ and γ with a precision of a tenth of a degree. $\dot{\phi}$ and $\dot{\gamma}$ are related to roll, pitch and yaw rates (p, q and r) as

$$\begin{aligned} p &= \dot{\phi} \\ q &= \dot{\gamma}\ \sin\phi \\ r &= \dot{\gamma}\ \cos\phi \end{aligned} \tag{2.1}$$

The apparatus degrees-of-freedom, ϕ and γ, can be related to the angle of attack, α, and the side slip angle, β. If α_0 is used to represent the nominal incidence angle, *i.e.* the angle between the longitudinal axis of the model and the freestream velocity for $\phi = \gamma = 0$, the following expressions result.

$$\begin{aligned} \cos\alpha\ \cos\beta &= \cos\alpha_0\ \cos\gamma \\ \sin\beta &= \sin\alpha_0\ \sin\phi - \cos\alpha_0\ \sin\gamma\ \cos\phi \\ \sin\alpha\ \cos\beta &= \sin\alpha_0\ \cos\phi + \cos\alpha_0\ \sin\gamma\ \sin\phi \end{aligned} \tag{2.2}$$

Mechanical constraints limit the degrees-of-freedom to the following ranges: $|\phi| < 105$ degrees and $|\gamma| < 30$ degrees. It is possible to vary the nominal incidence angle, α_0, in the range from 37 to 55 degrees. In the experiments conducted in this research α_0 was equal to 45 degrees. The reasons for selecting this value for α_0 are discussed in Chapter 3.

During dynamic experiments, the system is allowed to move in the two degrees-of-freedom, ϕ and γ. Provisions exist to lock each of the degrees-of-freedom independently at any position within the envelope of the apparatus. This feature is used during static experiments. Figure 2.4 shows a picture of the test section with the wind tunnel model mounted to the two degrees-of-freedom model support system. Detailed characteristics of the model support system are given in Appendix B.

---

[4] Precision potentiometer MKV-F78S. Conductive plastic RESISTOFILM®. New England Instrument Company. Woonsocket, RI 02895-1129.

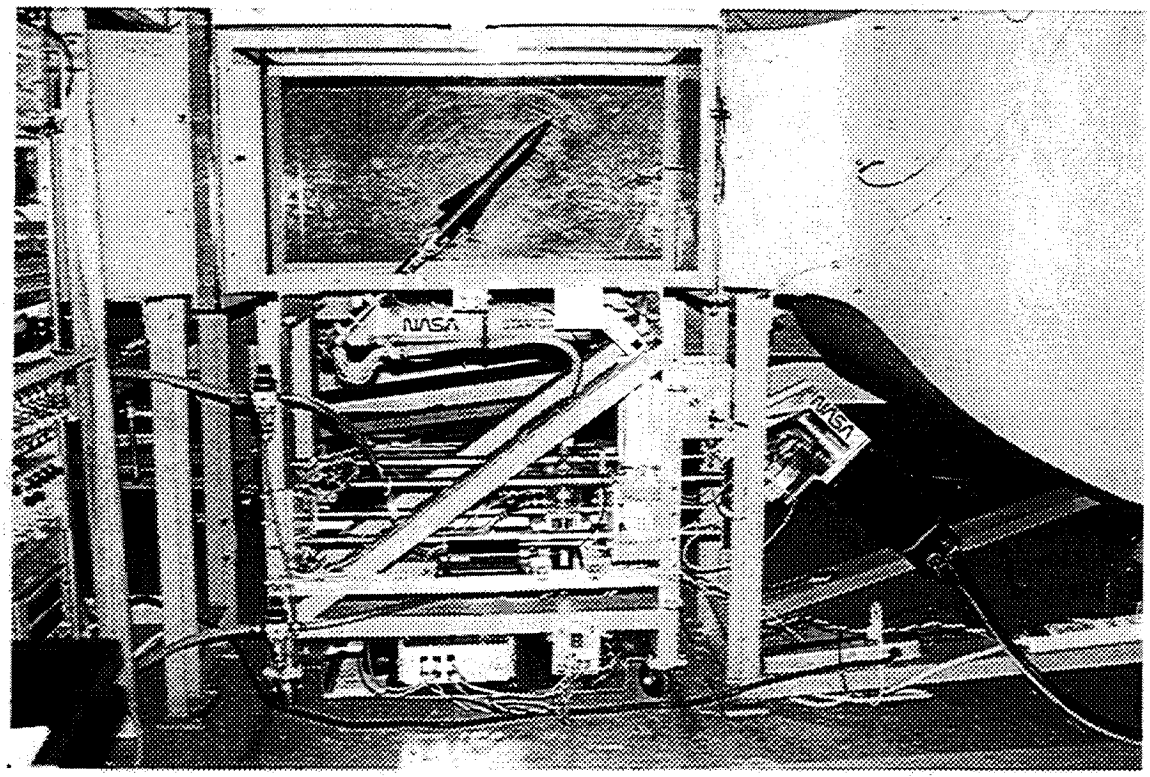

Figure 2.4: View of wind tunnel facilities and experimental apparatus.

2.3.1 Equations of Motion

The ϕ-axis and the γ-axis intersect at point P which is located at 0.46 mac (mean aerodynamic chord). Point P is shown in Figure 2.2. The equations of motion of the system in terms of the two degrees-of-freedom, ϕ and γ, can be written as:

$$\begin{aligned} &I_{M_x}\ddot{\phi} + (I_{M_z} - I_{M_y})\sin\phi\cos\phi\,\dot{\gamma}^2 + I_{M_{xz}}\cos\phi\,\ddot{\gamma} = M_\phi \\ &(I_A + I_{M_y}\sin^2\phi + I_{M_z}\cos^2\phi)\ddot{\gamma} + (I_{M_y} - I_{M_z})2\sin\phi\cos\phi\,\dot{\phi}\dot{\gamma} \\ &\qquad + I_{M_{xz}}(\ddot{\phi}\cos\phi - \dot{\phi}^2\sin\phi) = M_\gamma \end{aligned} \tag{2.3}$$

Where I_M is used to represent the inertia characteristics of the model with respect to a body fixed frame $X_M Y_M Z_M$ centered at point P. The X_M axis is oriented along the

longitudinal axis of the model. The Z_M axis is in the vertical symmetry plane of the model and oriented towards the pressure side of the model. The Y_M axis is given by the cross-product of Z_M by X_M. I_A is the inertia of the support system about the γ-axis. M_ϕ is the moment acting about the longitudinal axis of the model, *i.e.* ϕ-axis or X_M. M_γ represents the moment acting about the γ-axis.

For the model configuration used in this research, a vertical stabilizer is not present and the product of inertia is negligible, *i.e.*

$$I_{M_{xz}} \cong 0 \tag{2.4}$$

2.3.2 Roll and Yaw Sub-Systems

An important aspect of the design of the experimental apparatus is that the dynamic properties of the support system should not dominate the dynamic response of the model. The effects of the support mechanism on the dynamic behavior of the system can be understood through an examination of Equations 2.3. Expressions for the moments M_ϕ and M_γ are:

$$\begin{aligned} M_\phi &= M_\phi^A + M_\phi^T + M_\phi^F \\ M_\gamma &= M_\gamma^A + M_\gamma^T + M_\gamma^F + M_\gamma^G \end{aligned} \tag{2.5}$$

Where superscripts indicate the origin of the moments as follows:

A = Aerodynamics
T = Tubing for the air supply
F = Friction from bearings and potentiometers
G = Gravity restoring moment

Moments about the ϕ-axis are examined first. For $|\phi| < 40$ degrees M_ϕ^T is negligible. This is shown by the experimental data in Figure 2.5 where the dimensionless moment about the ϕ-axis caused by the tubing is plotted versus ϕ. A freestream velocity of 19.5 m/sec was used to calculate the non-dimensionalization factor defined as the product of the freestream dynamic pressure by the wing plan-form area and by the wing span.

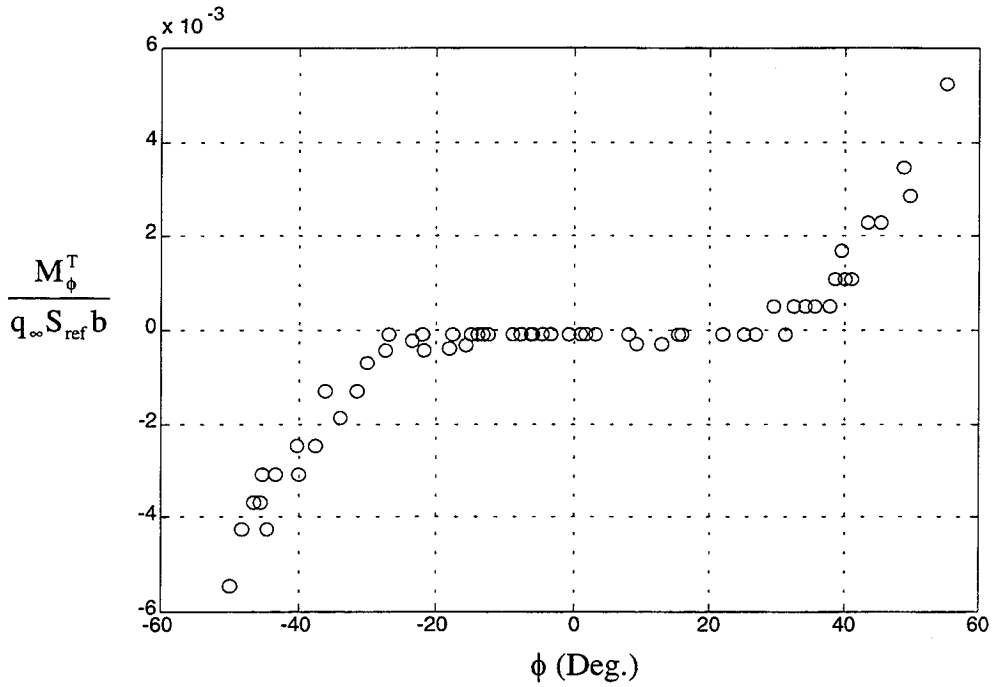

Figure 2.5: Measured moment about ϕ-axis due to spring effect of the air supply tubing.

The moment, M_ϕ^F , can be represented as:

$$M_\phi^F = -C_F\dot{\phi} \tag{2.6}$$

The coefficient C_F was identified from measurements of the torque about the ϕ-axis assuming M_ϕ^F given by Equation 2.6. Experimental results indicate that its value is equal to $(1.1 \pm 0.3) \times 10^{-3}$ Nm sec.

M_ϕ^T and M_ϕ^F represent disturbance moments about the ϕ-axis. To evaluate the impact of these moments on the dynamics of the system, an experiment was conducted with the model constrained at $\gamma = 0$ and free to move in roll. The model was released from rest for $\phi \cong 0$ and the amplitude of the roll oscillation increased until the limit cycle that characterizes the wing rock was reached. Figure 2.6 shows the dynamic aerodynamic loads and the measured disturbance moment caused by the air supply tubing, the bearings, and the potentiometer. As seen, the disturbance moment is about five percent of the aerodynamic loads. Although not negligible, the disturbance is not large enough to affect fundamentally the dynamic response of the system, *i.e.* the aerodynamic loads dominate the system dynamics. Therefore, no effort was directed to cancel these disturbances. The disturbances are known, they were measured, and were accounted for whenever necessary to resolve for the aerodynamic loads and the motion of the system.

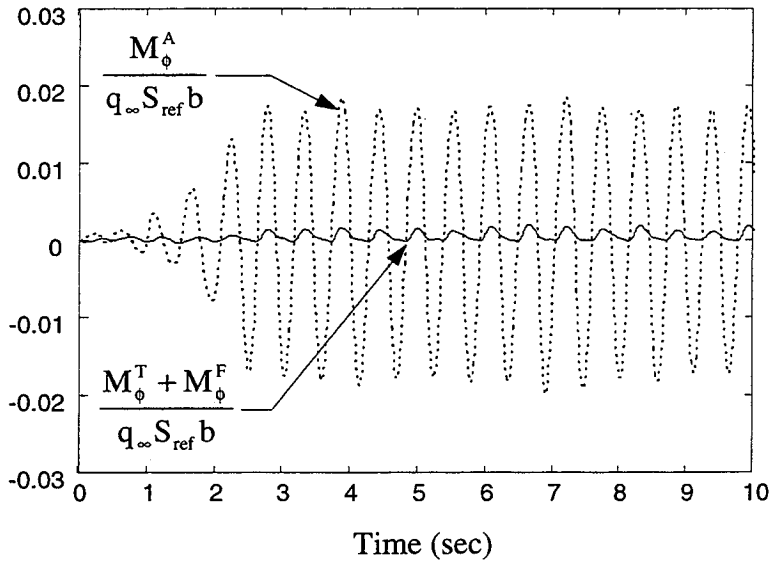

Figure 2.6: Aerodynamic moment and disturbance moment about ϕ-axis during roll oscillations. Model constrained to $\gamma = 0$ and free to roll.

For the motion about the γ-axis, the inertia, I_A, and the gravity restoring moment of the support system, M_γ^G, are the dominant factors in determining the dynamics of the system.

For this reason, a system to provide active cancellation of these effects was designed and built[5]. The idea consists of applying a torque to the γ-axle that cancels the undesired effects. An electric brushless motor[6] is used to generate a torque, M_γ^M, which is applied to the γ-axle. Adding this torque to the second of Equations 2.5, yields

$$M_\gamma = M_\gamma^A + M_\gamma^T + M_\gamma^F + M_\gamma^G + M_\gamma^M \tag{2.7}$$

The torque caused by the spring effect of the tubing, friction effect of the bearings and potentiometer, and gravity restoring moment are, respectively:

$$M_\gamma^T = -K_T\gamma \tag{2.8}$$

$$M_\gamma^F = -D_F\dot{\gamma} \tag{2.9}$$

$$M_\gamma^G = -K_G \sin\gamma \tag{2.10}$$

K_T , D_F and K_G are constants determined experimentally, and their numerical values are given in Appendix B. The torque commanded to the motor is given by:

$$M_\gamma^{M_c} \equiv I_A\hat{\ddot{\gamma}} + K_T\hat{\gamma} + K_G \sin\hat{\gamma} \tag{2.11}$$

where $\hat{\gamma}$ and $\hat{\ddot{\gamma}}$ are estimates of the angle γ and the angular acceleration $\ddot{\gamma}$. Using M_{error}^M to represent errors in the torque control loop, the actual torque applied to the shaft can be written as:

$$M_\gamma^M \equiv M_\gamma^{M_c} + M_{error}^M \tag{2.12}$$

---

[5] Designed by the author; machined by Mr. Tom Hasler and Mr. Matthew Chuck (Former Aero/Astro Machine Shop, Stanford University).

[6] Electro-Craft® Brushless Servo System: DM-30 drive, S-4075-R-H00AA motor. Reliance Motion Control, Inc. Eden Prairie, MN 55344.

Substituting Equations 2.5 through 2.10 into 2.3 results in the equations of motion for the two degrees-of-freedom system.

$$I_{M_x}\ddot{\phi} + (I_{M_z} - I_{M_y})\sin\phi\cos\phi\,\dot{\gamma}^2 + I_{M_{xz}}\cos\phi\,\ddot{\gamma} = M_\phi^A - C_F\dot{\phi}$$

$$(I_A + I_{M_y}\sin^2\phi + I_{M_z}\cos^2\phi)\ddot{\gamma} + (I_{M_y} - I_{M_z})2\sin\phi\cos\phi\,\dot{\phi}\dot{\gamma}$$

$$+I_{M_{xz}}(\ddot{\phi}\cos\phi - \dot{\phi}^2\sin\phi) = M_\gamma^A - D_F\dot{\gamma} - K_T\gamma - K_G\sin\gamma + M_\gamma^M \qquad (2.13)$$

where M_γ^M is given by Equations 2.11 and 2.12.

2.3.3 Implementation of Active Cancellation

To implement the active cancellation described in the previous section it is necessary to compute the torque to be applied to the system by the electric motor, $M_\gamma^{M_c}$. This torque is given by Equation 2.11 in terms of the estimates for the angle γ and its angular acceleration.

The angle γ is measured directly through the use of a potentiometer. This measured value, γ_m, is used as the estimate for γ, *i.e.* $\hat{\gamma} \equiv \gamma_m$. To estimate $\ddot{\gamma}$, two high precision linear accelerometers[7] were mounted to the γ-axle. They are located in the vertical plane that contains the γ-axis at equal distances on opposite sides of the γ-axle as shown in Figure 2.7. Adding the signals from the two accelerometers cancels the effect of specific weight and provides a signal that is proportional to $\ddot{\gamma}$. This measurement of the angular acceleration, $\ddot{\gamma}_m$, is accurate to 0.01 rad/sec^2 and is used as the estimate value for that quantity, *i.e.* $\hat{\ddot{\gamma}} \equiv \ddot{\gamma}_m$. In this way the torque required to cancel the external effects is computed according to Equation 2.11, using the measurements for γ and $\ddot{\gamma}$ as their estimates.

---

[7] Systron Donner 4310A-1-P116 Linear Servo Accelerometer. Systron Donner Company. Inertial Division. Concord, CA 94518.

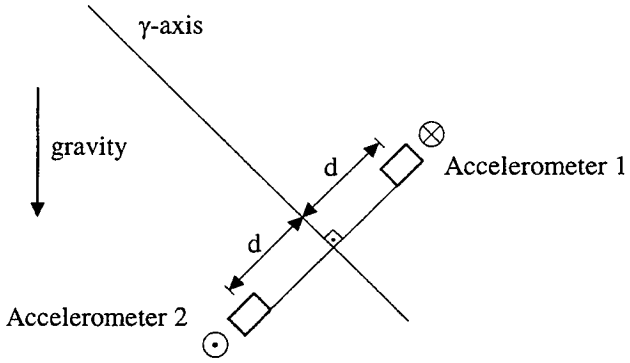

Figure 2.7: Measurement of angular acceleration $\ddot{\gamma}$ using two linear accelerometers.

A torque sensor was designed to satisfy the specific requirements of this application. The sensor connects the electric motor to the γ-axle and provides a measurement of the torque that the motor applies to the system. Figure 2.8 shows a side view of the test section with the two degrees-of-freedom model support and part of the active cancellation system.

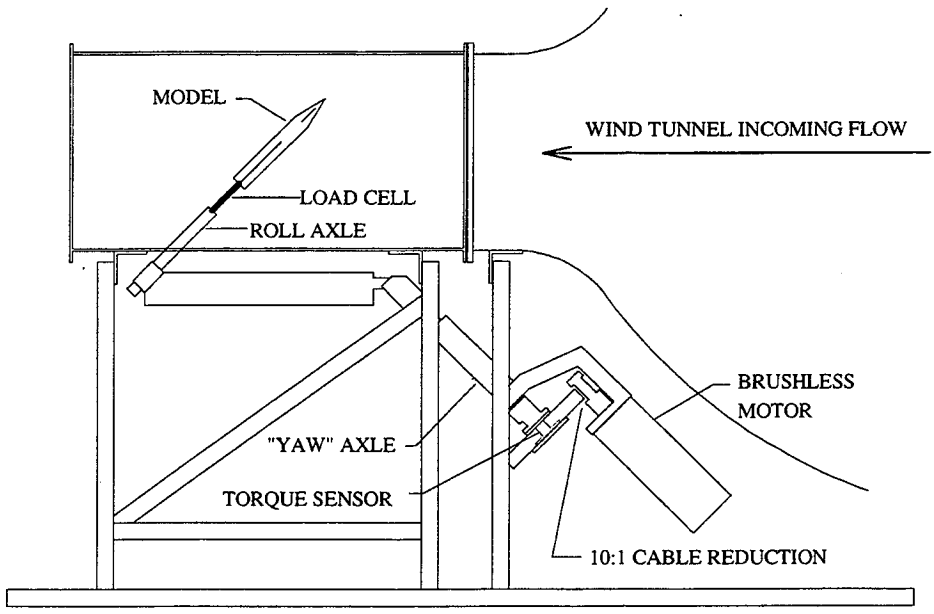

Figure 2.8: Side view of test section and components of the active cancellation system.

A torque control loop was implemented to minimize errors between the commanded torque and the actual torque applied to the γ-axle. A micro-computer, equipped with A/D and D/A converters, was used to implement the closed-loop control logic and command the electric motor drive. Figure 2.9 illustrates the concept and implementation of the active cancellation in block diagram form.

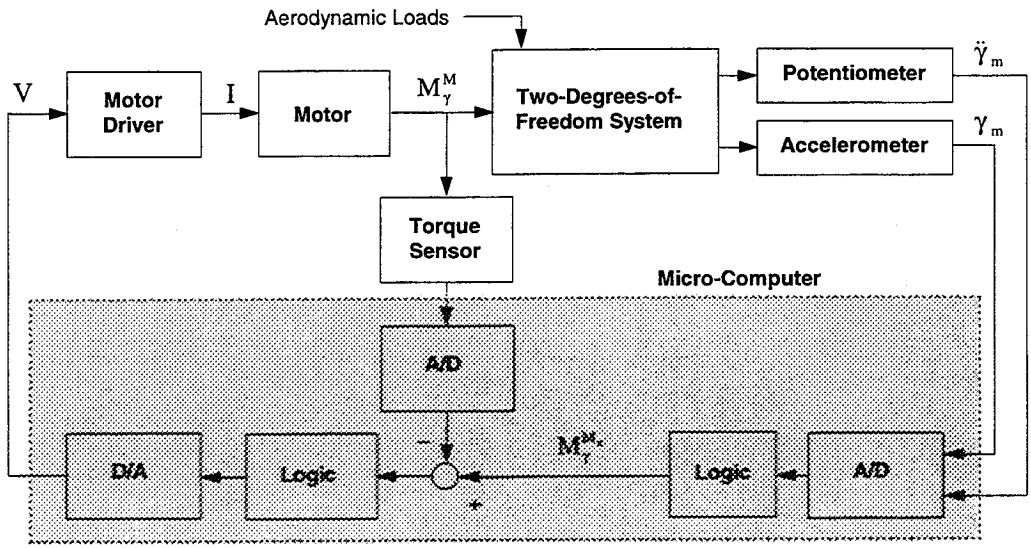

Figure 2.9: Concept and implementation of the active cancellation loop.

Conceptually, the active cancellation of external effects would produce a system driven only by the aerodynamic loads. In reality, the cancellation is not perfect due to limitations of the actual implementation. Errors occur in the torque closed-loop control and in the measurements of γ and $\ddot{\gamma}$. To assess the performance of the cancellation loop, the error between the commanded torque, as given by Equation 2.11, and the actual torque measured during the natural motion of the system is shown in Figure 2.10. The unsteady aerodynamic moment about the γ-axis, M_γ^A , is also shown for comparison. The torque due to errors in the cancellation loop is up to 14% of the aerodynamic moment. This indicates that although the aerodynamics is the main factor determining the motion of the system about the γ-axis, the errors in the cancellation loop need to be included in

describing the dynamics of the system. The main reason for the large errors in the cancellation loop is the large inertia of the support system[8] which requires the application of a large torque to the γ-axle. This means that even a small percentage error in the applied torque translates into a significant moment as compared to the aerodynamic loads. For these reasons, when using the equations of motion for the two degrees-of-freedom system either the moment applied by the motor was explicitly included or the cancellation error was treated as a disturbance.

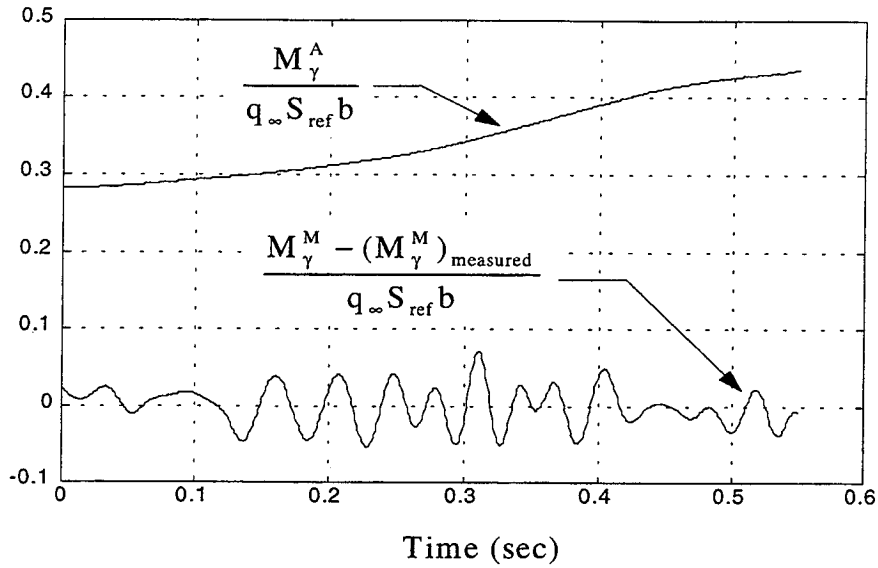

Figure 2.10: Performance of the active cancellation loop.

2.4 Air Injection System

Since the model had no movable control surfaces, the injection of air, *i.e.* blowing, was the only actuator available in the experiments. The use of this actuator to control the motion of the two degrees-of-freedom system required the capability of injecting a known amount of air through the slots located at the forebody of the model. The amount of air injected was quantified by the jet momentum coefficient, C_μ, defined as:

[8] The inertia of the support about the γ-axis is approximately 50 times the inertia of the model in yaw.

$$C_\mu \equiv \frac{\dot{m}_j V_j}{q_\infty S_{ref}} \tag{2.14}$$

where $\dot{m}_j$ is the jet mass flow rate through the slot , V_j is the jet velocity at the exit of the plenum, q_∞ is the freestream dynamic pressure and S_{ref} is a reference area (wing planform area).

Specially designed flowmeters were used to measure the mass flow rate from which the jet momentum coefficient was calculated. They were located outside the test section and connected to the exit of the servo-valves which control the air flow rate and the tubing which brought air to the model. The flowmeters were built around miniature pressure transducers[9] as shown in Figure 2.11.

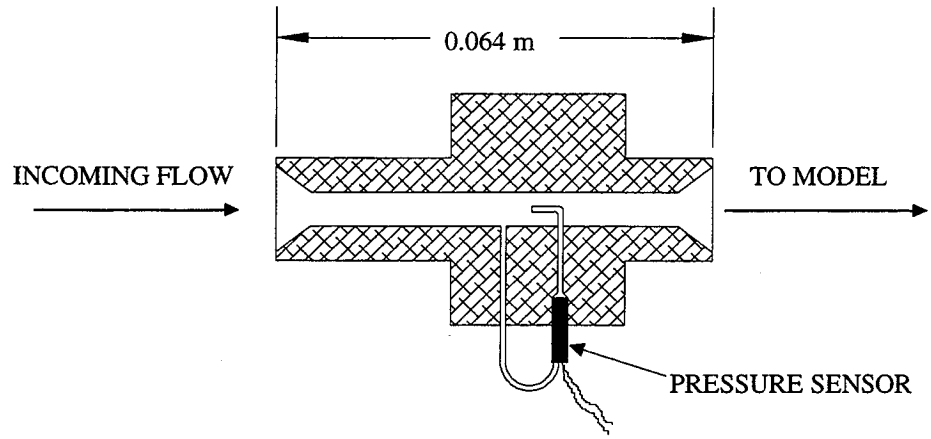

Figure 2.11: Specially designed flowmeters used to measure C_μ.

The transducer measures the dynamic pressure along the center line inside the flowmeter from which the mass flow rate was obtained through a calibration of the device [19, 20]. C_μ was calculated directly from the output of the transducer as

[9] Kulite Miniature IS® Silicon Diaphragm Pressure Transducer - XCS-093 Series. Kulite Semiconductor Products, Inc. Leonia, NJ 07605.

$$C_\mu \cong 2k_F \frac{A_F^2}{A_j q_\infty S_{ref}} \vartheta_F \tag{2.15}$$

k_F is a constant obtained from the calibration of the flowmeter, A_F is the flowmeter cross-sectional area, ϑ_F is the output signal from the flowmeter, and A_j is the area of the forebody slot through which air is injected.

Air was provided to the model through flexible tubing. Two servo-valves[10] were used to vary the amount of injected air on each plenum independently. The valves were mounted to the structure supporting the test section. Their input lines were connected to a high-pressure air supply and their output lines were connected to the flowmeters. A detailed description of the servo valves is given by Wong [9]. A closed-loop control system was used to control the amount of air that was injected through each slot on the model. Figure 2.12 shows the block diagram for the closed-loop control of C_μ. Feedforward was used to compensate for the non-linear characteristic of the valves, and feedback control was used to generate adequate transient C_μ response and to reject errors caused, for example, by pressure fluctuations on the source line.

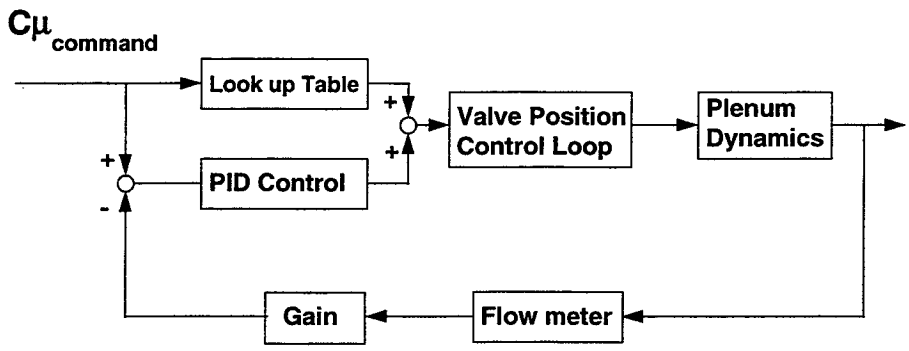

Figure 2.12: C_μ closed-loop control.

[10] Designed by Dr. Grant S. Wong [9]; machined by Mr. Tom Hasler (Former Aero/Astro Machine Shop).

The performance of the C_μ closed-loop control is shown in Figure 2.13 in terms of the response to a step input. The rise time of 0.006 seconds corresponds to a bandwidth of approximately 50 Hz. In steady state the closed-loop control maintained the value of C_μ constant within ± 0.0018 ($\pm 3\sigma$).

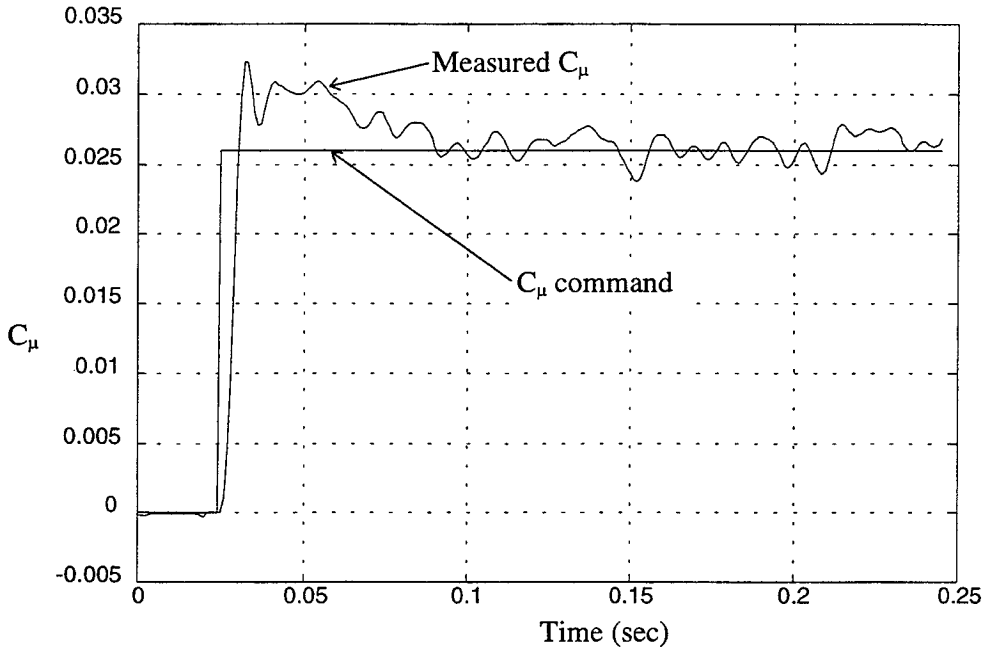

Figure 2.13: Performance of C_μ control loop.

2.5 Force-Torque Sensor

A six-component force-torque sensor[11] was used for static and dynamic measurements of the aerodynamic loads. The sensor was used to connect the model to the roll axle and to provide measurements of forces and moments in a body-fixed coordinate frame. Experience in using the sensor showed that it was adequate for all components except for the measurements of the axial force component, for which the resolution was not adequate for these experiments. Figure 2.14 shows the six-component sensor assembled to the roll shaft and the model.

[11] Mini 90N/4.2Nm. Serial #FT3253. Assurance Technologies, Inc. Garner, NC 27529.

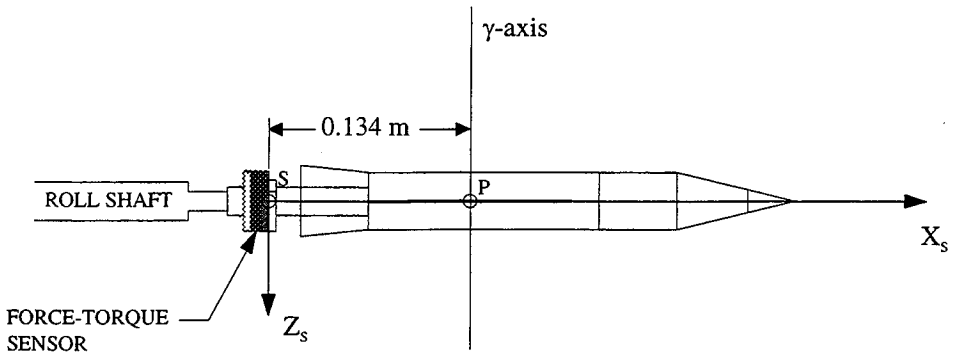

Figure 2.14: Assembly of the six-component force-torque sensor to model and roll shaft.

The maximum operational loads and the resolution of each component are listed in Table 2.1 with respect to frame $X_sY_sZ_s$ centered at point S on the sensor[12].

Component	Range	Resolution
Forces along Y_s , Z_s	± 90 N	0.045 N
Force along X_s	± 90 N	0.135 N
Moments about X_s, Y_s, Z_s	± 4.2 Nm	0.0011 Nm

Table 2.1: Characteristics of the six-component force-torque sensor.

2.6 Flow Visualization Equipment

For the flow visualization experiments, an argon-ion laser and an optical system were used to generate a laser sheet perpendicular to the model longitudinal axis. The optics were mounted on a traversing system allowing the laser sheet to be moved over the full length of the model. This capability was used to perform axial scans starting from the forebody and moving downstream to characterize the development of the flow structure.

[12] Point S is defined in Figure 2.14.

A smoke generator located upstream of the model was used to seed the flow. A video camera was placed outside of the test section aligned with the model longitudinal axis. The camera was used to record the results from the flow visualization experiments and also the motion of the system during dynamic experiments. The location of the laser sheet, smoke generator and video camera are illustrated in Figure 2.15.

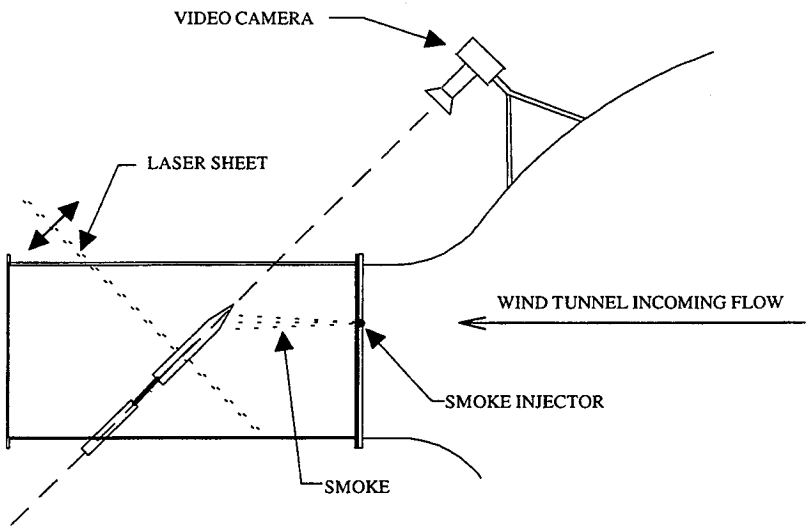

Figure 2.15: Setup for flow visualization experiments.

2.7 Real-Time Control System and Data Acquisition

Three micro-computers equipped with data acquisition boards were used in the experiments. One computer was dedicated to the active cancellation loop. A second computer was used to implement the closed-loop control of the vehicle, *i.e.* to control the amount of air injected in each plenum according to the logic used to control the two degrees-of-freedom system. A third computer was used for data acquisition.

Figure 2.16 illustrates the operation of the real-time vehicle control. Two of the elements represented in the block diagram have been described in this chapter: The dynamics of the two degrees-of-freedom system and the closed-loop control of C_μ. The other two

blocks in the diagram, the aerodynamic loads and the control logic, are developed in the following chapters. A model of the aerodynamic loads was required before a solution to the control problem could be pursued.

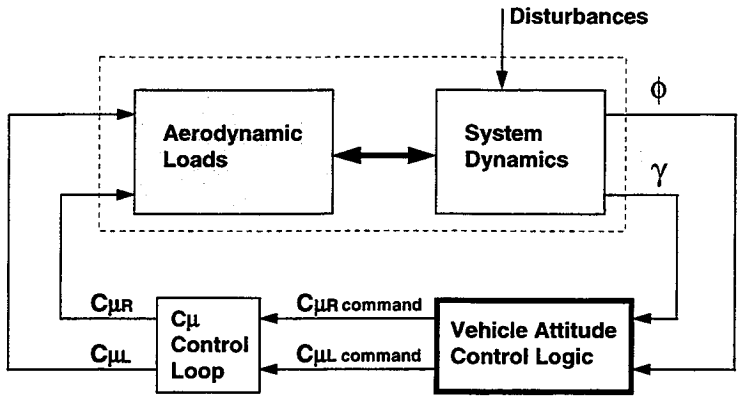

Figure 2.16: Vehicle real-time control.

The next three chapters, Chapters 3, 4 and 5, address the problems of understanding and deriving an aerodynamic model which includes the effects of blowing and is suitable for controls. In Chapter 6 the aerodynamic model is used in the development of a control approach that uses blowing to control the wind tunnel model in two degrees-of-freedom.

Chapter 3

Experimental Observations

The main characteristics of the flow over the wind tunnel model are presented in this chapter. The objectives are to obtain insight into the physics of the flow and to create the basis for the formulation of an aerodynamic model that can be used to predict the loads acting on the vehicle. In particular, the effects of forebody tangential blowing on the structure of the flow and on the roll and yaw moments are determined. It is also determined to what extent the characteristics of the vehicle vary with blowing, as well as the dependence of blowing effectiveness on the attitude of the vehicle.

Flow visualization experiments were conducted to reveal the flow structure and how it is affected by the roll and yaw angles and blowing. Static measurements of the roll and yaw moments are presented for various blowing intensities and roll and yaw angles. The highly non-linear characteristics of asymmetric blowing are examined. It is shown that superposition of symmetric and asymmetric blowing linearizes the blowing effect. The mechanisms through which forebody tangential blowing works are identified, and their relative importance for the given model configuration and testing conditions is determined. Transient responses of roll and yaw moments to step input blowing are determined and characterized in terms of time constants. Differences in the time constants are explained based on the mechanisms through which roll and yaw moments are generated. A dynamic experiment conducted to characterize the natural motion of the two

degrees-of-freedom system showed that the system was unstable. Time histories are presented for the roll and yaw angles. The experiments were conducted at a nominal incidence angle of 45 degrees and freestream velocity of 19.5 m/sec. At this velocity the Reynolds number based on the wing root chord is 260,000.

Static experiments showed that for the nominal incidence angle, α_0 , in the range from 20 to 50 degrees, minimum control authority occurs at 45 degrees, *i.e.* the roll and yaw moments generated by blowing are minimum for $\alpha_0 = 45$ degrees. If control is demonstrated for this worst case condition, a stronger argument can be made that it could also be demonstrated at other incidence angles. This rationale guided the selection of α_0. Proper correlation of the results from flow visualization, static and dynamic measurements of the loads, and dynamic experiments requires that these experiments be conducted at the same conditions, in particular at the same freestream velocity. This limited the freestream velocity to 19.5 m/sec which is the maximum value at which flow visualization experiments could be conducted using the available equipment.

The chapter is organized as follows: The results from flow visualization are presented first, followed by the measurements of static aerodynamic loads. After that, effects due to the particular geometry of the wind tunnel model are discussed, and the mechanisms through which blowing works are identified and analyzed. Finally, the transient responses of roll and yaw moments to blowing are presented, as well as the natural motion of the system in two degrees-of-freedom.

3.1 Flow Structure

In this section a discussion about the flow structure is presented based on results from flow visualization experiments. The equipment used in the experiments was described in Chapter 2. Results presented here consist of pictures of the flow at different cross-sections of the model. The pictures provide a view along the longitudinal axis of the

model[1]. At high angles of attack flow separation occurs at the wing and forebody. It is known that, for slender bodies at incidences greater than two times the nose semi-apex angle, an asymmetric vortex system is formed and is oriented in one of two stable mirror-image positions [11]. Therefore, it is expected that the forebody vortices are asymmetric. On the other hand, the sharp edges of the wing induce some symmetry in the flow by forcing separation at the wing leading-edges. The resulting flow field depends on the interaction of forebody and wing vortices and was determined through flow visualization experiments.

3.1.1 Axial Scan Experiments

In Figure 3.1 results of flow visualization experiments are presented for $\phi = \gamma = 0$ and $C_\mu = 0$. Pictures are shown for several stations along the model. The flow is asymmetric and vortical structures were observed on all stations along the model. The asymmetry starts on the forebody and becomes more evident downstream. As the flow develops downstream, the vortex that is close to the forebody remains close to the fuselage, and on that side no distinct wing vortex was observed. On the opposite side, the vortex that is away from the forebody becomes even more distant as the flow progresses downstream. At stations where the wing is present, this vortex is distant enough that its effect on the wing vortices might not be significant. On these stations, a distinct wing vortex was observed on the side where the forebody vortex is far away from the fuselage. Experiments demonstrated that a dominant three-vortex structure was observed at stations where the wing is present.

3.1.2 Roll Angle Effect

Figure 3.2 presents results from flow visualization experiments for $\gamma = 0$, $C_\mu = 0$ and various values of the roll angle. An asymmetric three-vortex structure was observed in all cases. Comparing the cases for which $\phi = 20$ degrees and $\phi = 0$ it is seen that the asymmetry favors the same side but the relative positions of the vortices are different. For

[1] See Figure 2.15.

$\phi = -20$ degrees the asymmetry favors the opposite side as compared to $\phi = 0$ and $\phi = 20$ degrees. Although the changes in flow structure are more noticeable at the wing-body section they are also seen at the forebody section. There is a minimum value of the roll angle for which the asymmetry changed into its mirror-image configuration. For the wind tunnel model and test conditions used in these experiments this value is approximately -15 degrees.

3.1.3 Effects of Asymmetric Blowing

The effect of asymmetric blowing on the flow structure is shown in Figure 3.3 for $\phi = \gamma = 0$. The term asymmetric blowing is used to indicate that blowing was applied either to the right or to the left side of the model. Comparing Figures 3.3 (a) and (c) it is seen that applying blowing to the right side (starboard) moves the right side separation line to the leeside of the vehicle, while on the left side the separation line moves towards the pressure side of the model. Although the flow structure is similar for the cases with no blowing and with right side blowing, Figures 3.3 (a) through (d), it is clearly seen that the positions of the vortices are different. Most likely their strengths are also different. As a consequence of varied vortices positions and strengths, the aerodynamic loads on the model are altered by blowing. Figures 3.3 (e) and (f) show the flow structure for the case where blowing was applied to the left side of the model (port side). In this case, the asymmetric vortex structure has changed into its mirror-image configuration as compared to the cases with no blowing and with right side blowing. There is a minimum amount of blowing that is required to cause this change, for the current configuration and test conditions this minimum value is given by $C_\mu = 0.0045$.

3.1.4 Effects of Symmetric Blowing

In this case, blowing was applied simultaneously on both sides of the forebody. The effect on the flow structure is shown in Figure 3.4, for $\phi = \gamma = 0$. Pictures for the no blowing case are included for comparison. A major change in the flow structure was observed as compared to the case where no blowing was applied. Figures 3.4 (a) and (c)

show that symmetric blowing moves the separation lines towards the leeside of the forebody. For large values of blowing, the flow over the forebody can be considered attached. Figures 3.4 (b) and (d) show a cross-section of the model where the wing is present. It is seen that, the asymmetric three-vortex structure present in the no blowing case, Figure 3.4 (b), is replaced by a more symmetric two-vortex structure when symmetric blowing is applied, Figure 3.4 (d). As a consequence, it is expected that symmetric blowing causes alleviation of the lateral loads. This effect will be examined in more detail later in this chapter.

Experiments showed that superimposing asymmetric blowing to symmetric blowing results in an asymmetric two-vortex flow structure as illustrated in Figure 3.5.

3.2 Static Aerodynamic Loads

Results for the static aerodynamic loads are presented in this section. Whenever possible these results are correlated to the flow visualization observations presented in the previous section. This correlation of quantitative and qualitative results provides a more in-depth understanding of the aerodynamic phenomena.

Several questions regarding the characteristics of forebody tangential blowing as an actuator can be addressed by analyzing the static aerodynamic loads. In particular the effects of blowing on the static forces and moments acting on the vehicle can be determined, and the possibility of including blowing as an incremental effect can be investigated.

The effects of roll and yaw angles and blowing on the roll and yaw moment coefficients, C_l and C_n respectively, are presented for a nominal angle of attack of 45 degrees and freestream speed of 19.5 m/sec. For clarity, error bars are not included in the plots. The accuracy of the measurements of C_l and C_n are respectively: $\pm$ 0.0025 and $\pm$ 0.016.

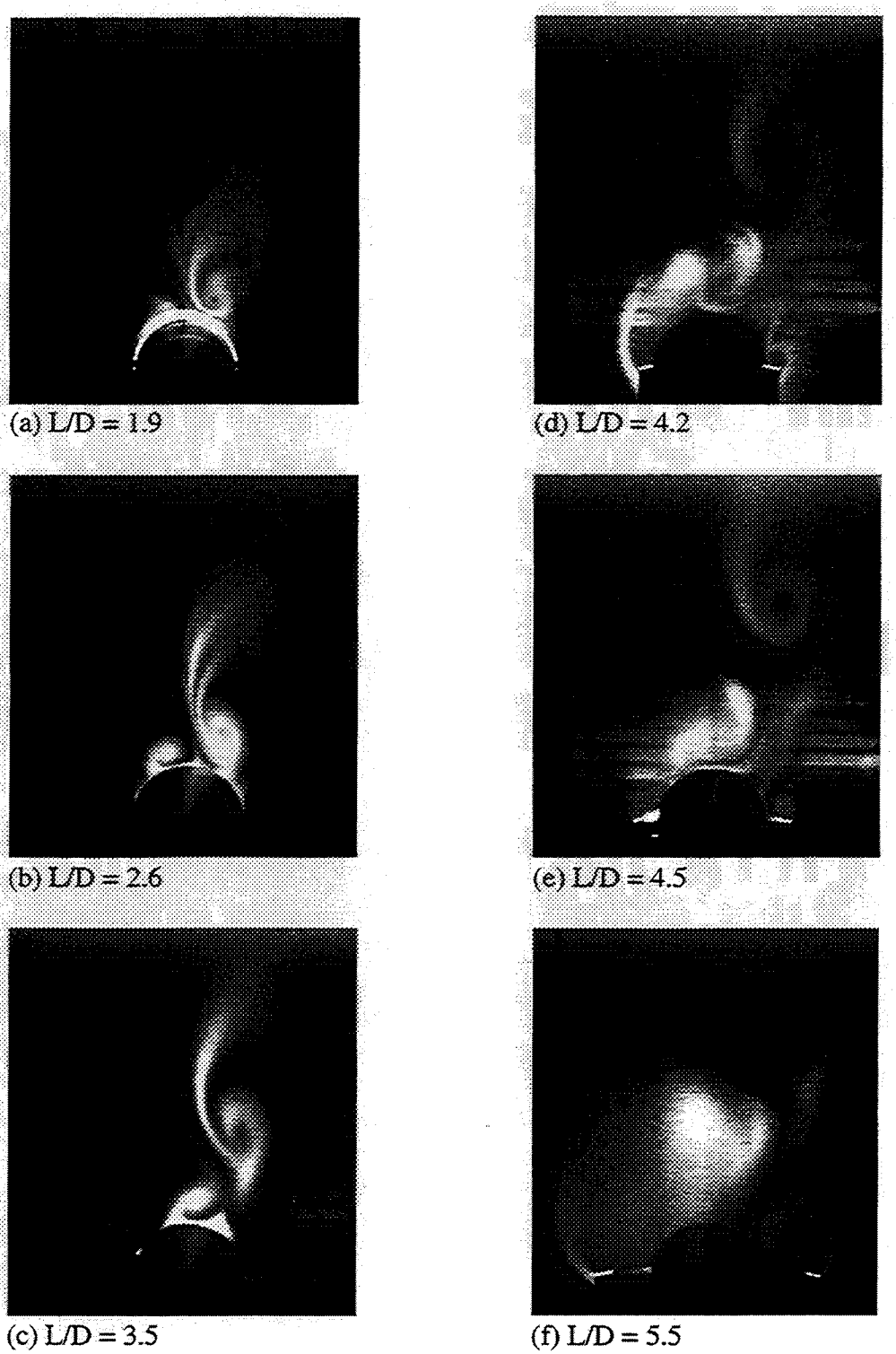

Figure 3.1: Flow visualization results from axial scan experiments. $\phi = \gamma = 0$ and $C_\mu = 0$. $\alpha = 45$ degrees and $U_\infty = 19.5$ m/sec.

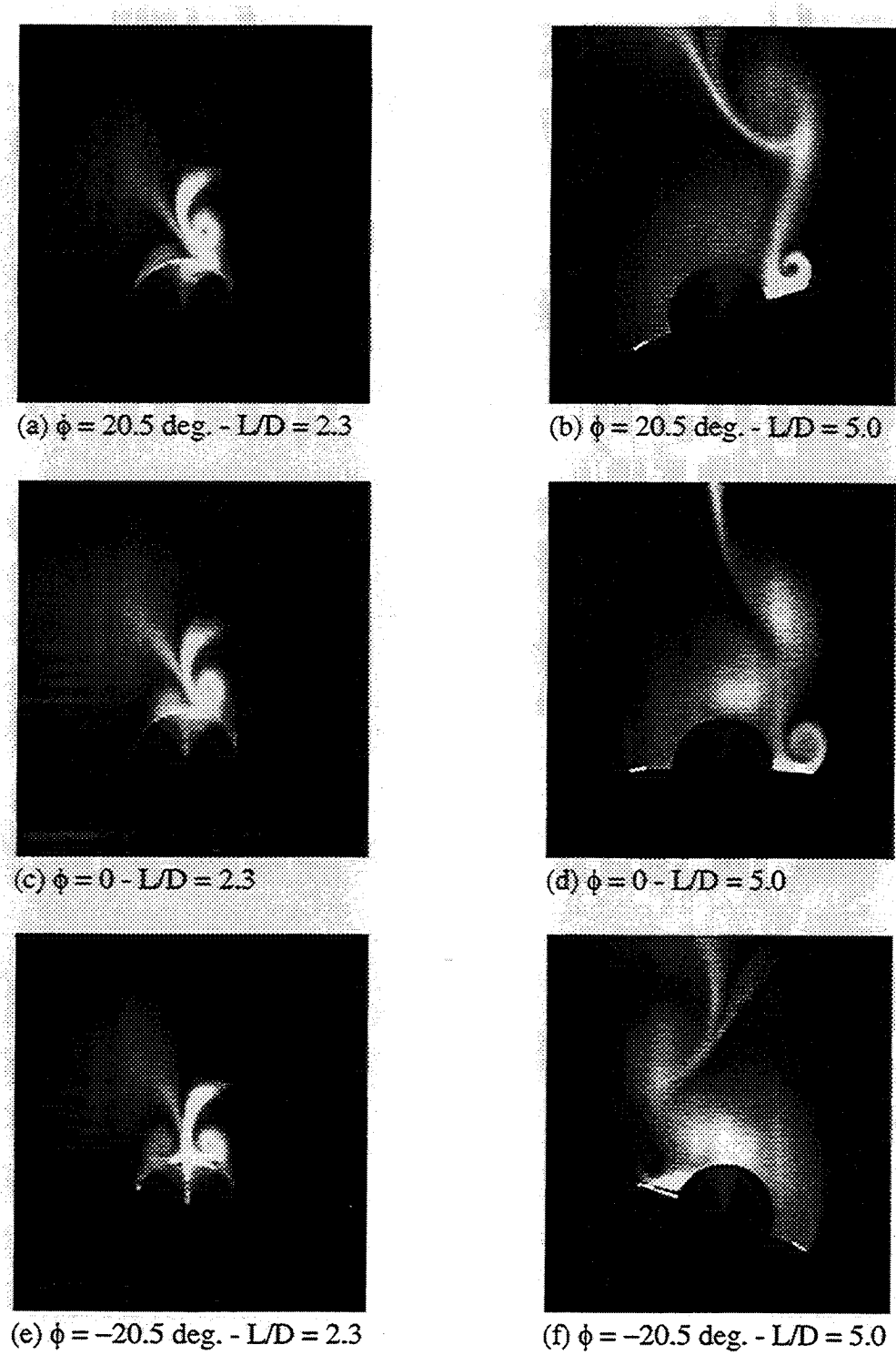

Figure 3.2: Roll angle effect on the structure of the flow for $\gamma = 0$ and $C_\mu = 0$. Nominal incidence angle, α_0 , is 45 degrees and U_∞ = 19.5 m/sec.

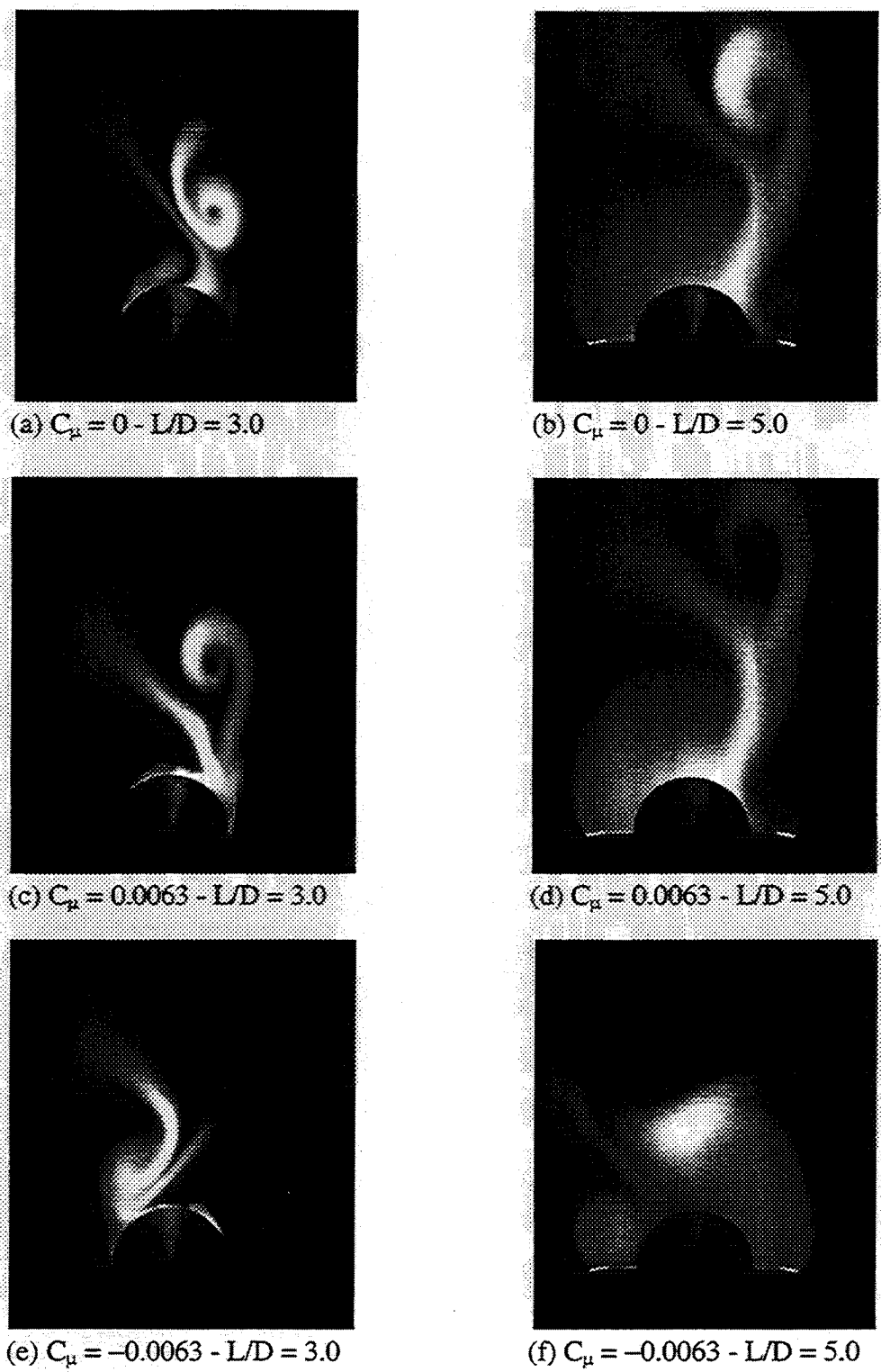

Figure 3.3: Effect of asymmetric blowing on the structure of the flow for $\phi = \gamma = 0$. $\alpha = 45$ degrees and $U_\infty = 19.5$ m/sec.

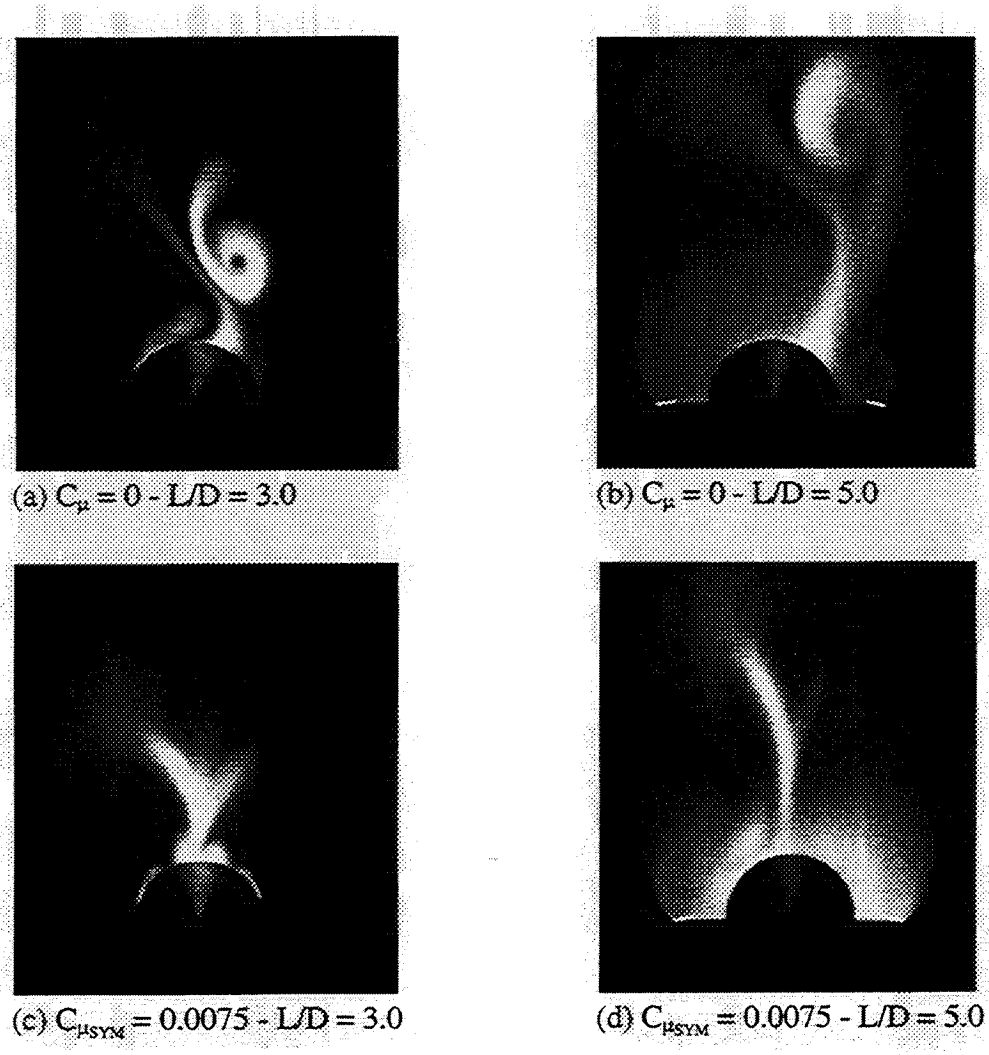

Figure 3.4: Effect of symmetric blowing on the structure of the flow for $\phi = \gamma = 0$. $\alpha = 45$ degrees and $U_\infty = 19.5$ m/sec.

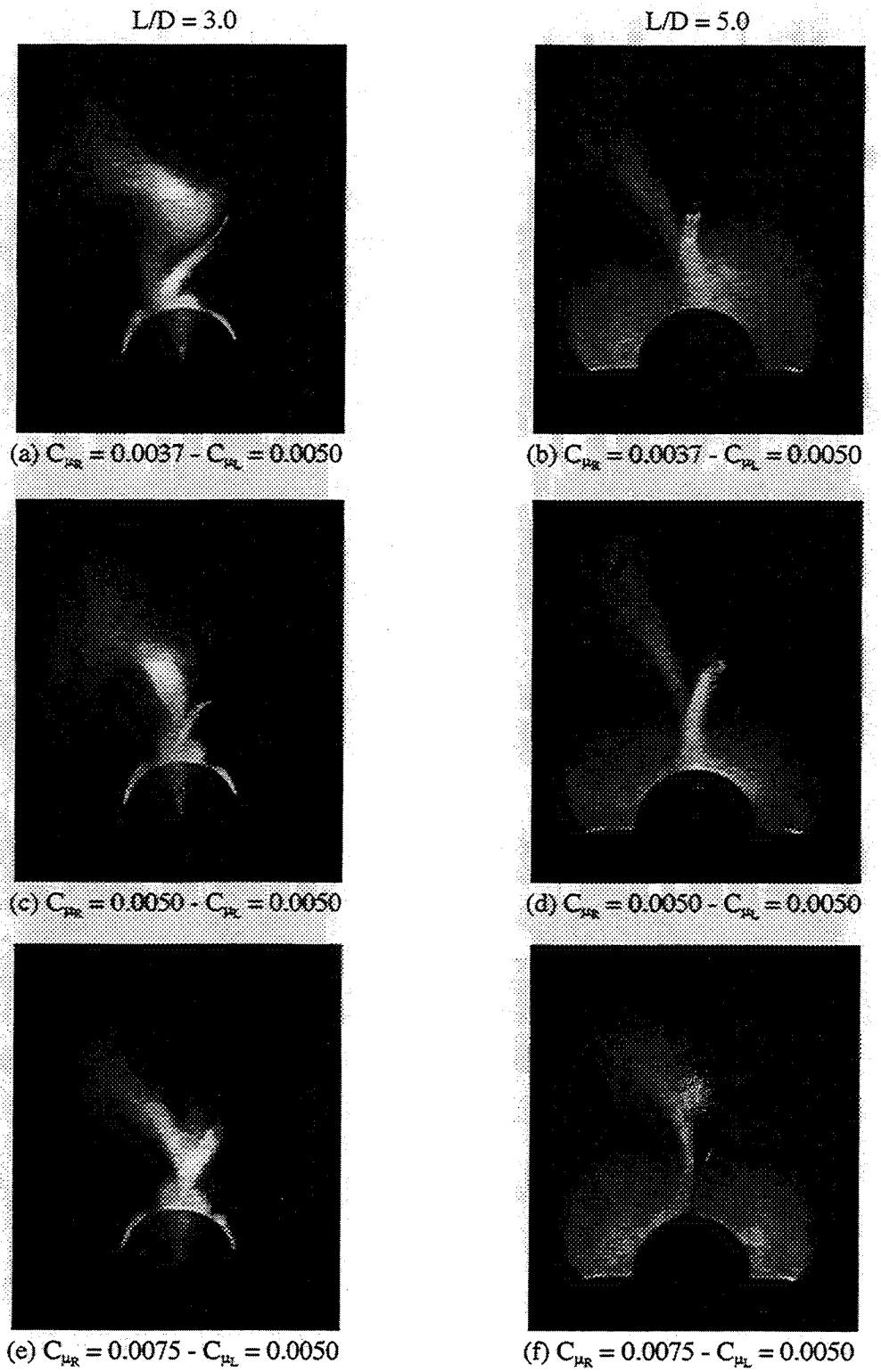

Figure 3.5: Effect of superimposed symmetric and asymmetric blowing on the structure of the flow for $\phi = \gamma = 0$. $\alpha = 45$ degrees and $U_\infty = 19.5$ m/sec.

3.2.1 Cause of Asymmetry

The results from the flow visualization experiments showed that the flow is asymmetric when no blowing is applied and $\phi = \gamma = 0$. As a consequence, it is expected that at these conditions the roll and yaw moments acting on the model are non-zero. This is confirmed in Figure 3.6 where the roll and yaw moment coefficients, C_l and C_n, are plotted versus roll angle for zero yaw angle and $C_\mu = 0$.

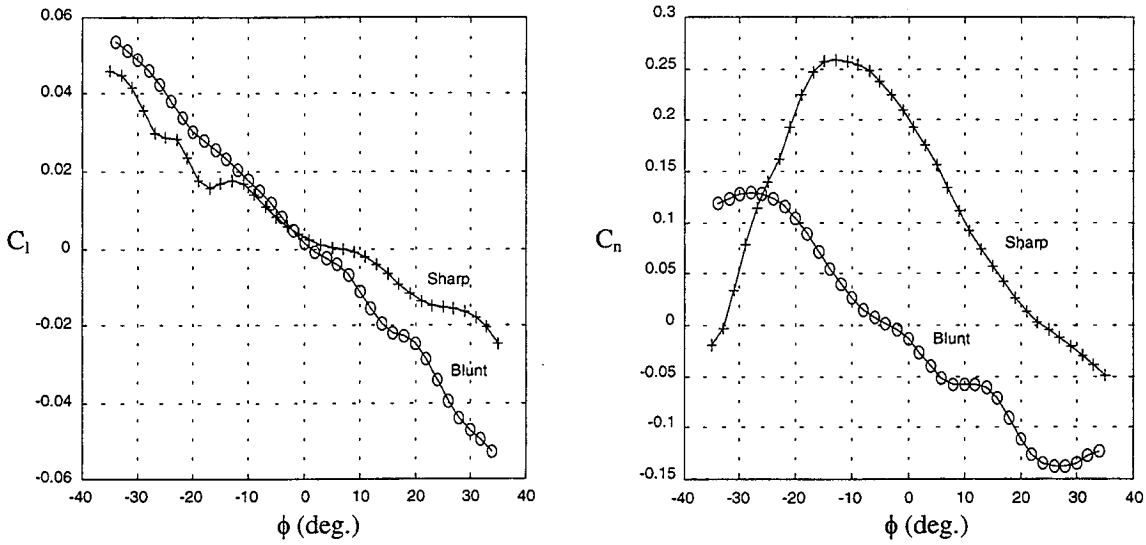

Figure 3.6: Effect of forebody tip geometry on the roll and yaw moment coefficients, C_l and C_n, for $\gamma = 0$ and $C_\mu = 0$. $\alpha_0 = 45$ degrees and $U_\infty = 19.5$ m/sec.

The asymmetry observed in the C_l and C_n curves is attributed to small geometric imperfections near the tip of the forebody. To verify that this is actually the cause of asymmetry, the conical tip of the forebody was replaced by a blunt tip, which consists of a semi-sphere with a radius of 0.00762 m (0.3 inches). The results for such configuration are also shown in Figure 3.6 for $\gamma = 0$ and $C_\mu = 0$. It is seen that for the model with the blunt forebody tip, the roll and yaw moments are close to zero at $\phi = \gamma = 0$. This is in contrast to the large moments obtained when the conical tip is used. Also, when the blunt tip is used, the curves for C_l and C_n versus roll angle present a large degree of symmetry

as opposed to the highly asymmetric curves obtained with the conical tip. These results support the hypothesis that the asymmetries were caused by small geometric imperfections near the tip of the conical forebody.

3.2.2 Effects of Roll and Yaw Angles

In Figure 3.7 the roll and yaw moment coefficients are plotted versus the roll angle for $C_\mu = 0$ and various values of γ. For $\gamma = 0$, the C_l curve presents a change in slope for $\phi \cong -15$ degrees while the slope of the C_n curve changes sign at about this same roll angle. These changes correlate well with results from the flow visualization experiments which showed that the asymmetric three-vortex structure changed into its mirror-image configuration for $\phi \cong -15$ degrees. The slopes of the curves C_l and C_n versus roll angle represent the static stability derivatives C_{l_ϕ} and C_{n_ϕ} respectively. It is seen that in general these quantities depend on the attitude of the vehicle, *i.e.* ϕ and γ.

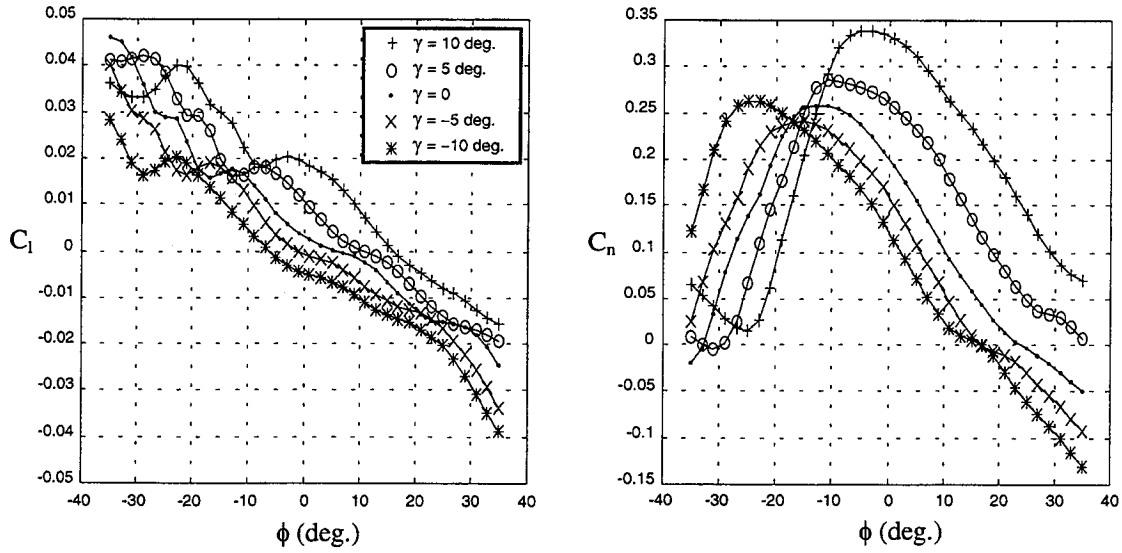

Figure 3.7: Roll and yaw moment coefficients, C_l and C_n, versus roll angle ϕ for various γ and $C_\mu = 0$. $\alpha_0 = 45$ degrees and $U_\infty = 19.5$ m/sec.

Shown in Figure 3.8 are plots for C_l and C_n versus γ for various values of the roll angle and for $C_\mu = 0$. In this case, the slopes of the curves represent the static stability derivatives in γ, C_{l_γ} and C_{n_γ}. It is seen that these quantities are functions of ϕ and γ.

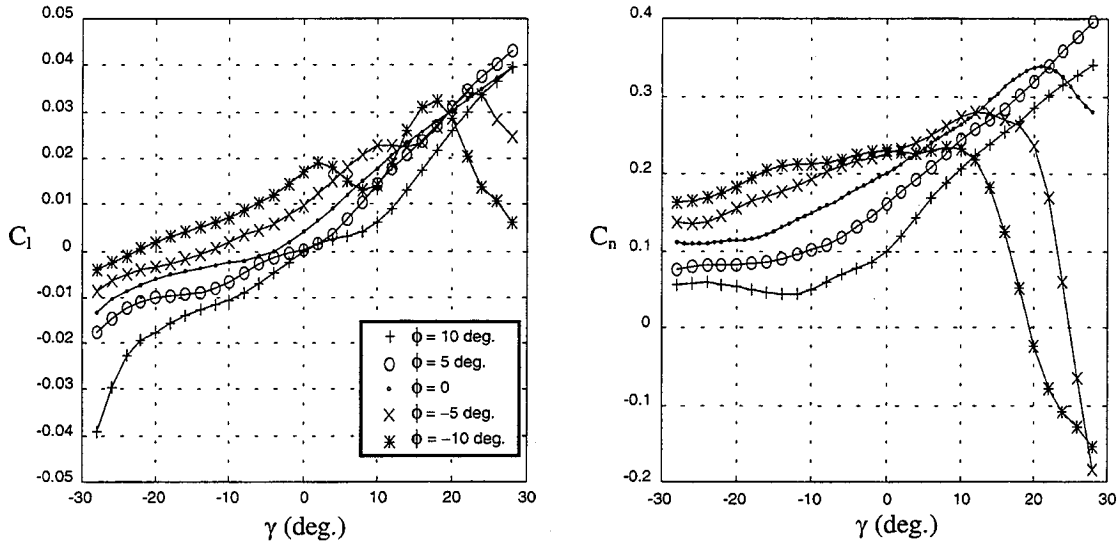

Figure 3.8: Roll and yaw moment coefficients, C_l and C_n, versus γ for various ϕ and $C_\mu = 0$. $\alpha_0 = 45$ degrees and $U_\infty = 19.5$ m/sec.

The plots in Figures 3.7 and 3.8 indicate that, in general, the stability derivatives are a function of the attitude of the vehicle. The data in these figures show that within limited regions of the $\phi\gamma$-plane the stability derivatives do not present large variations. For example, for $|\phi|$ and $|\gamma|$ less than 5 degrees it is reasonable to assume that stability derivatives in ϕ and γ are constant.

3.2.3 Effects of Asymmetric Blowing

Application of blowing either to left or to the right side of the model is referred to as asymmetric blowing. Its effects on the roll and yaw moments are discussed in this section. A convention is adopted that right side, *i.e.* starboard blowing is positive, and left side, *i.e.* port side blowing negative, Table 3.1.

	Starboard Blowing - C_{μ_R}	Port Side Blowing - C_{μ_L}
$C_\mu > 0$	C_μ	0
$C_\mu = 0$	0	0
$C_\mu < 0$	0	$\lvert C_\mu \rvert$

Table 3.1: Sign convention for asymmetric blowing.

In Figure 3.9 the roll and yaw moment coefficients, C_l and C_n , are plotted versus roll angle for $\gamma = 0$ and different values of asymmetric blowing, C_μ. Taking the curves for $C_\mu = 0$ as the reference, it is seen that, for $|\phi| < 20$ degrees, blowing on the left side produced a larger variation in the roll and yaw moments as compared to right side blowing. This can be understood by recalling the results from the flow visualization experiments. Figure 3.3 shows that the cases for no blowing and right side blowing present an asymmetry that favors the same side. On the other hand, left side blowing has the effect of changing the flow asymmetry into its mirror image configuration. Therefore, the observed behavior of the static loads is expected since the more radical change in the flow structure would generate larger changes in the aerodynamic loads.

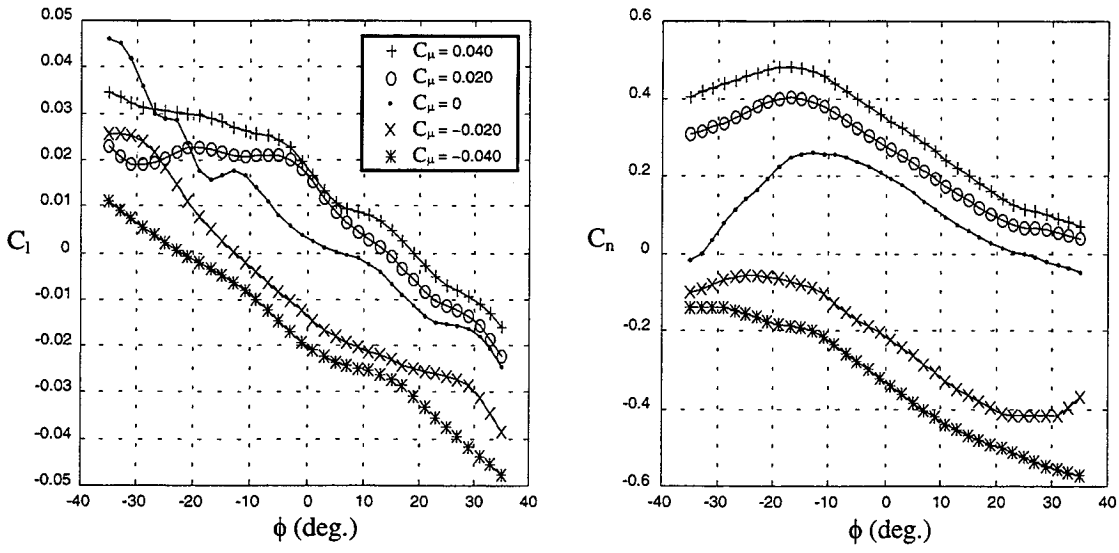

Figure 3.9: Roll and yaw moment coefficients, C_l and C_n , versus roll angle ϕ for $\gamma = 0$ and various C_μ. $\alpha_0 = 45$ degrees and $U_\infty = 19.5$ m/sec.

Further analyses of the data in Figure 3.9 show that the stability derivatives C_{l_ϕ} and C_{n_ϕ} are a function of C_μ. For example, for $\phi = -10$ degrees and no blowing $C_{l_\phi} < 0$ while for the same roll angle and $C_\mu = 0.02$, $C_{l_\phi} \cong 0$. For $\phi \cong -20$ degrees, the stability derivative C_{n_ϕ} changes sign depending on the amount of blowing.

Figure 3.10 shows plots for the roll and yaw moment coefficients versus yaw angle for $\phi = 0$ and different values of asymmetric blowing, C_μ. As in the plots of Figure 3.9, these show a larger change in moments when blowing was applied to the left side as compared to the right side. In this case, the slopes of the curves represent the stability derivatives in γ. It is seen that, they are less dependent on blowing than the stability derivatives in ϕ.

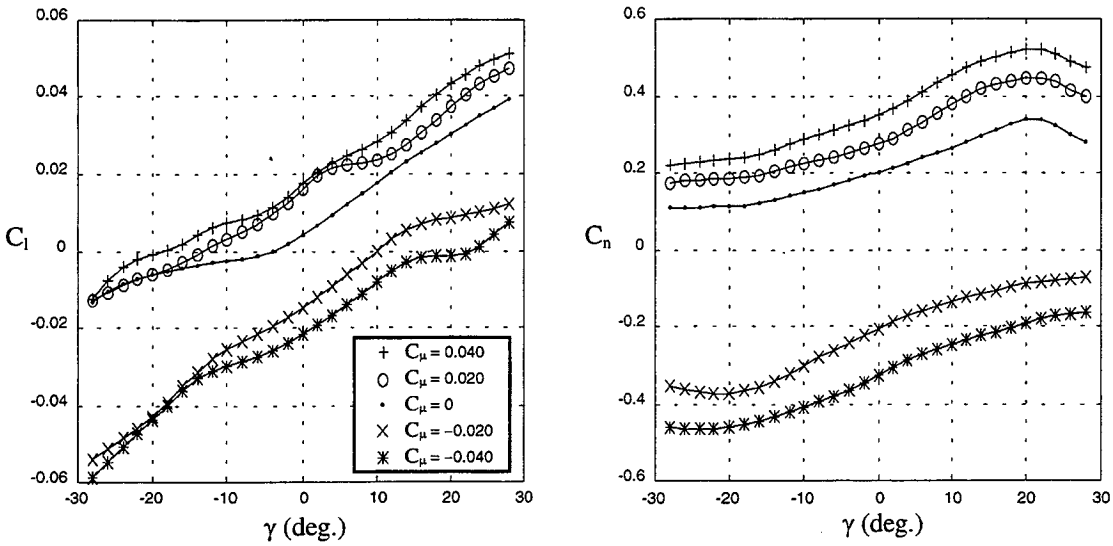

Figure 3.10: Roll and yaw moment coefficients, C_l and C_n, versus γ for $\phi = 0$ and various C_μ. $\alpha_0 = 45$ degrees and $U_\infty = 19.5$ m/sec.

In Figure 3.11 C_l and C_n are plotted versus asymmetric blowing, C_μ, for $\gamma = 0$ and various values of the roll angle. These plots show the highly non-linear characteristics of forebody tangential blowing as an actuator. It is also seen that the effects of blowing on the roll and yaw moments are a function of the roll angle, especially for small amounts of blowing.

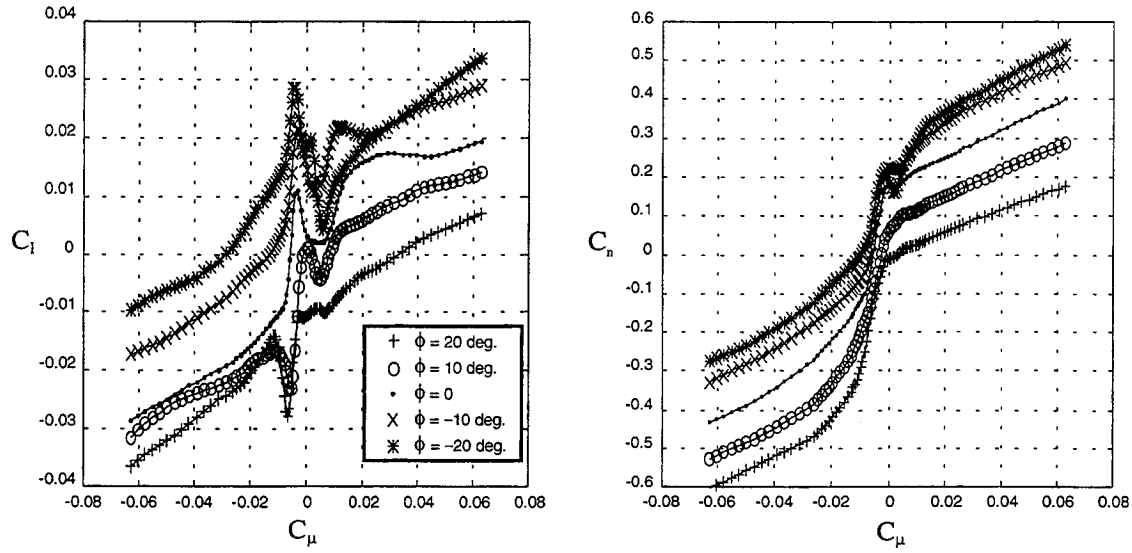

Figure 3.11: Roll and yaw moment coefficients, C_l and C_n, versus asymmetric blowing, C_μ, for various ϕ and $\gamma = 0$. $\alpha_0 = 45$ degrees and $U_\infty = 19.5$ m/sec.

For completeness, roll and yaw moment coefficients are plotted versus C_μ in Figure 3.12 for $\phi = 0$ and various values of γ.

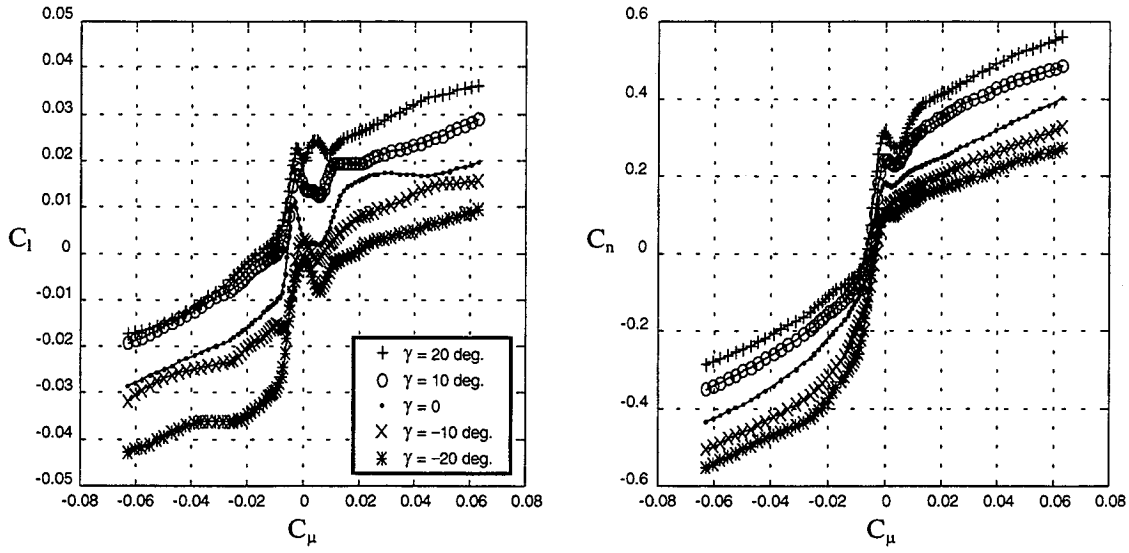

Figure 3.12: Roll and yaw moment coefficients, C_l and C_n, versus asymmetric blowing, C_μ, for $\phi = 0$ and various γ. $\alpha_0 = 45$ degrees and $U_\infty = 19.5$ m/sec.

A plausible explanation for the highly non-linear behavior of C_l and C_n is that small values of blowing have an effect similar to the geometric imperfections near the tip of the forebody and can cause asymmetry in the flow. The effects of disturbances like forebody geometric asymmetry or a small jet blowing normal to the surface of the forebody were investigated by Degani [21, 22]. It was shown that either disturbance can cause flow instabilities that generate vortex asymmetry. It was also shown that the level of asymmetry is dependent upon the size and location of the disturbance.

3.2.4 Effects of Superimposed Symmetric and Asymmetric Blowing

In this section results are presented for the roll and yaw moment coefficients when symmetric blowing, $C_{\mu_{SYM}}$, and asymmetric blowing, ΔC_μ , are superimposed. Table 3.2 specifies how blowing was applied. Starboard or right side blowing is represented by C_{μ_R} and port side or left side blowing by C_{μ_L}.

	Starboard Blowing - C_{μ_R}	Port Side Blowing - C_{μ_L}
$\Delta C_\mu > 0$	$C_{\mu_{SYM}} + \Delta C_\mu$	$C_{\mu_{SYM}}$
$\Delta C_\mu = 0$	$C_{\mu_{SYM}}$	$C_{\mu_{SYM}}$
$\Delta C_\mu < 0$	$C_{\mu_{SYM}}$	$C_{\mu_{SYM}} + \lvert\Delta C_\mu\rvert$

Table 3.2: Superimposed symmetric and asymmetric blowing.

Figure 3.13 shows plots of C_l and C_n versus asymmetric blowing, ΔC_μ , for various values of symmetric blowing and $\phi = \gamma = 0$. These plots show that symmetric blowing produces side load alleviation. This is expected and is in agreement with flow visualization experiments which showed that symmetric blowing brings symmetry to the flow. For $C_{\mu_{SYM}} = 0.01$ the roll and yaw moment present an almost linear dependence on asymmetric blowing, ΔC_μ. Experiments have shown that using larger values of $C_{\mu_{SYM}}$ produces an even more linear characteristic, but decreases the slope of the C_n versus ΔC_μ

curve which indicates a less efficient actuator[2]. Also, larger values of $C_{\mu_{SYM}}$ means larger consumption of air. These results demonstrate a physical means of linearizing the highly non-linear characteristics of forebody tangential blowing.

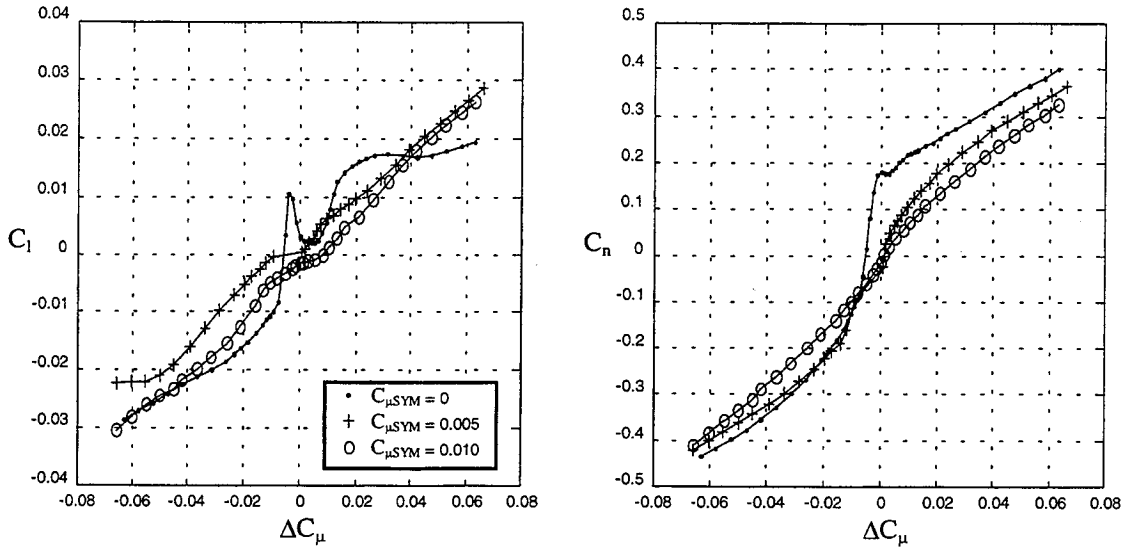

Figure 3.13: Effect of superimposed symmetric blowing, $C_{\mu_{SYM}}$, and asymmetric blowing, ΔC_μ, on the roll and yaw moment coefficients, C_l and C_n, for $\phi = \gamma = 0$ and various values of $C_{\mu_{SYM}}$. $\alpha_0 = 45$ degrees and $U_\infty = 19.5$ m/sec.

Figure 3.14 presents data for roll and yaw moment coefficients versus ΔC_μ for $C_{\mu_{SYM}} = 0.01$ and various values of the roll and yaw angles. It is seen that the linearization effect obtained by the addition of symmetric blowing is effective over a broad range of roll and yaw angles.

In Figure 3.15, C_l and C_n are plotted versus ϕ and γ for $C_{\mu_{SYM}} = 0.01$ and different values of ΔC_μ. The slope of the curves (static stability derivatives in ϕ and γ) do not present large changes due to ΔC_μ. This is in contrast with the case where only asymmetric blowing is applied.

[2] When large values of symmetric blowing are used the flow can be considered attached over the forebody. In this case, generation of yaw moment is mainly due to change in circulation on the forebody which is achieved by superimposing asymmetric blowing. In this case, starboard and port side blowing have opposite effects, and the larger the value of symmetric blowing used the less efficient the generation of yaw moment will be.

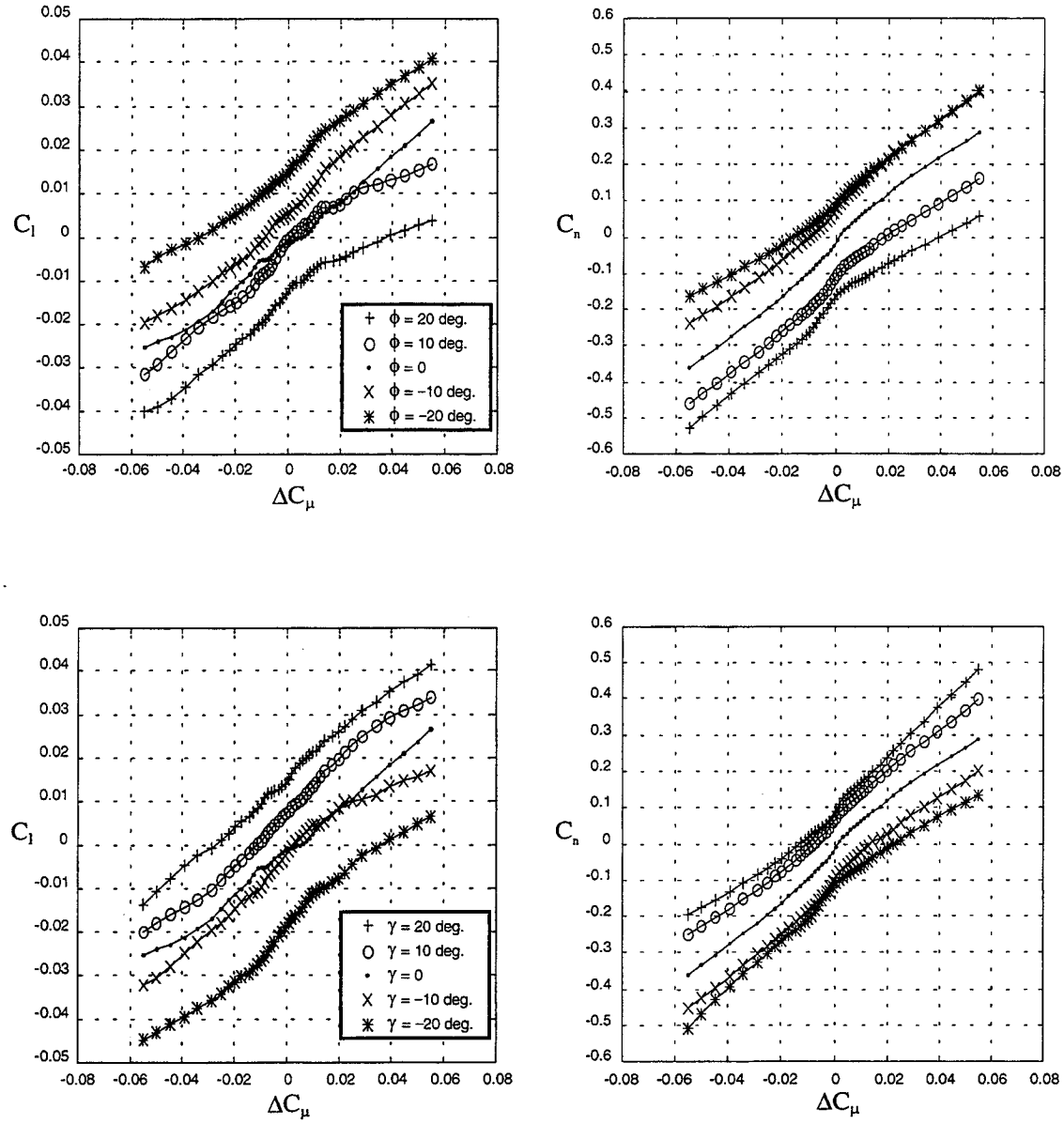

Figure 3.14: Roll and yaw moment coefficients versus asymmetric blowing for $C_{\mu_{SYM}} = 0.01$ and various ϕ and γ. $\alpha_0 = 45$ degrees and $U_\infty = 19.5$ m/sec.

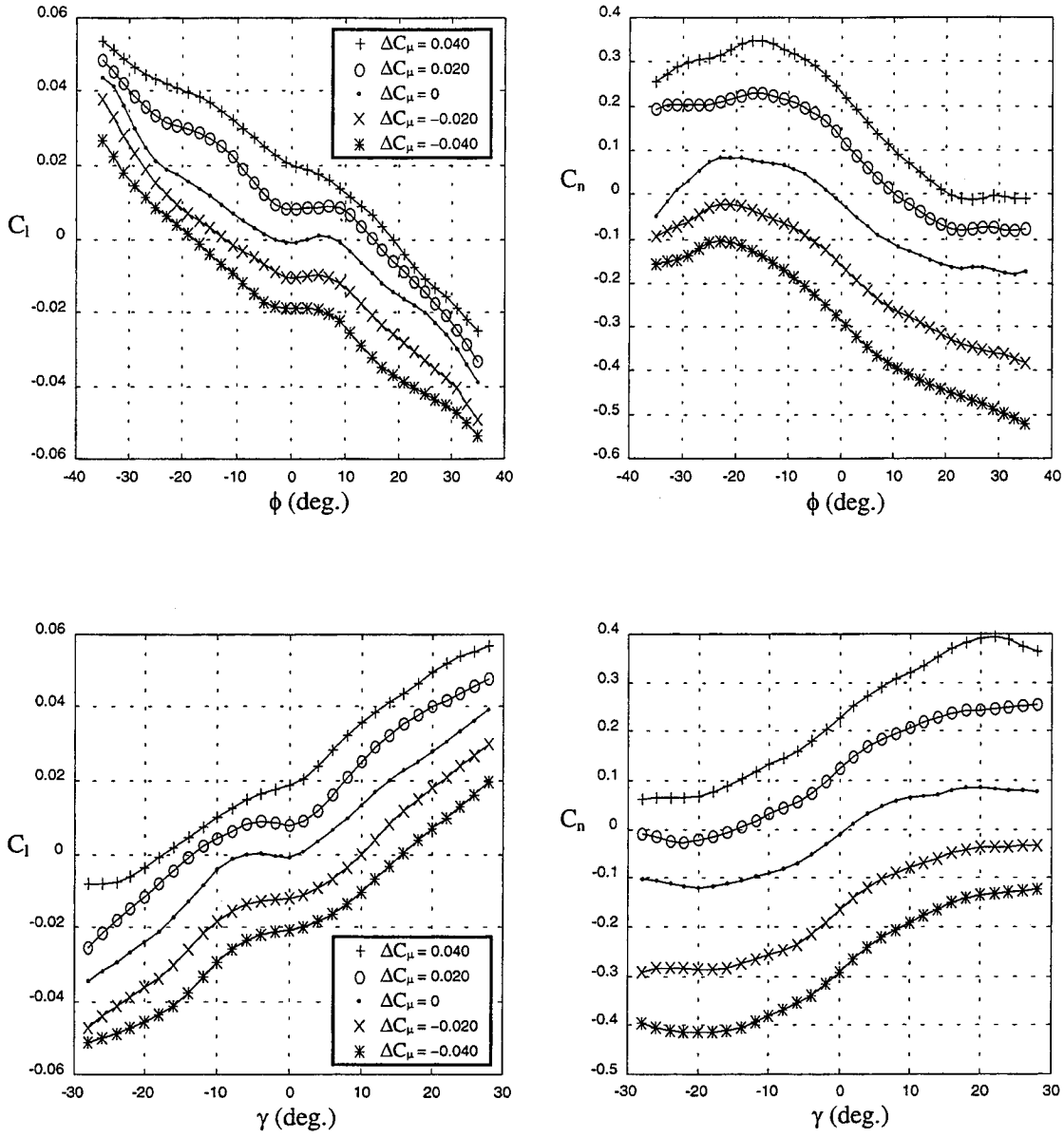

Figure 3.15: Roll and yaw moment coefficients versus roll and yaw angles for $C_{\mu_{SYM}} = 0.01$ and various ΔC_μ. $\alpha_0 = 45$ degrees and $U_\infty = 19.5$ m/sec.

3.3 Effects of Geometry

In studying the behavior of the aerodynamic loads presented in the previous sections it is important to realize some particular features associated with the geometric configuration of the wind tunnel model used in this research. As described in Chapter 2, the model consists of a cone-cylinder fuselage and a sharp leading-edge delta wing.

Because the fuselage is of circular cross-section, integrating the pressure over the fuselage produces zero roll moment. Therefore, for $C_\mu = 0$ roll moment is generated only at sections where the wing is present. When asymmetric blowing is applied, there also is a contribution to the roll moment caused by the direct jet momentum.

The wings do not contribute to the yaw moment because they are thin and only offer area perpendicular to the yaw axis. As a consequence, yaw moment is only generated at the fuselage.

3.4 Forebody Tangential Blowing - Mechanisms

Results from the flow visualization experiments and analysis of the basic physics of the phenomena, allow the identification of the main mechanisms through which forebody tangential blowing alters the loads acting on the vehicle. Those are

1. Displacement of the forebody separation lines
2. Centrifugal or wall-jet effect
3. Direct jet momentum

The basic idea of forebody tangential blowing as an effective actuator relies on the fact that a small change in the forebody separation lines produces large variations in the aerodynamic loads due to the flow amplification effect caused by vortex growth. This is the main mechanism through which FTB works. The wall-jet effect and the direct jet momentum are secondary effects, that only become important when large amounts of

blowing are applied. A discussion of these effects and their relative importance is presented in the following sections.

3.4.1 Displacement of the Forebody Separation Lines

The change in the position of the forebody separation lines caused by blowing was observed during flow visualization experiments, as shown in Section 3.1.3. On the side which blowing is applied the jet energizes the boundary layer and the separation line moves towards the leeside of the vehicle. On the opposite side, the separation line moves towards the vehicle's pressure side. The displacement of the separation lines has a local effect of altering the regions where flow is attached, and an outer flow effect due to the change in the vortices positions and strengths.

Local Effect

For stations of the model where the slots are present, and for some stations downstream of the slots, partial recovery of attached flow occurs on the side where blowing is applied. These regions of recovered attached flow are subject to lower pressure as compared to separated flow, and as a consequence, side force and yaw moment are generated. The early separation on the opposite side causes an increase in pressure over that region of the forebody and also contributes to the generation of side force and yaw moment. This mechanism of load generation can also be explained by a change in circulation in the forebody caused by the displacement of the separation lines.

Outer Flow Effect

When the forebody separation line moves towards the leeside of the vehicle, a weaker vortex is generated because of the lower vorticity level at that region. In contrast, the levels of vorticity on the forebody are highest in the direction normal to the incoming flow. Therefore, as blowing changes the separation lines, it alters the positions and strengths of the vortices. A second mechanism of change is the vorticity introduced by

the jet directly into the flow. As shown by Font [17], a tangential jet introduces both positive and negative vorticity into the flow.

Varied positions and strengths of the vortices changes the pressure field and the aerodynamic loads over the forebody. Also, the trajectories of the vortices are modified and their interaction with wing vortices produces a modified flow field. Ultimately, the entire flow over the vehicle is changed, as well as the aerodynamic loads.

3.4.2 Centrifugal or Wall-Jet Effect

The term wall-jet effect is used to represent the normal pressure gradient that counteracts the centrifugal force developed as the jet curves to follow the surface of the forebody. This effect is only important if the jet remains attached over a significant portion of the forebody. Therefore, at high angles of attack and lower values of blowing this effect is not important. For the current model configuration, the wall-jet effect contributes mainly to the yaw moment. It has no effect on the roll moment.

Assuming two dimensional flow and carrying out a force balance on a fluid element in the cross-flow plane result in the following expression for the normal pressure gradient.

$$\Delta P = \rho_j w_j \frac{V_j^2}{R} \tag{3.1}$$

Using the above expression for the pressure gradient, the wall-jet contribution to the yaw moment coefficient is given by:

$$C_{n_{wj}} = \frac{1}{q_\infty S_{ref} b} \int_{\theta=0}^{\theta_{sep}} \int_{x_1}^{x_2} \rho_j V_j^2 w_j x \cos\theta \, dx \, d\theta \tag{3.2}$$

Where x and θ are defined in Figure 3.16.

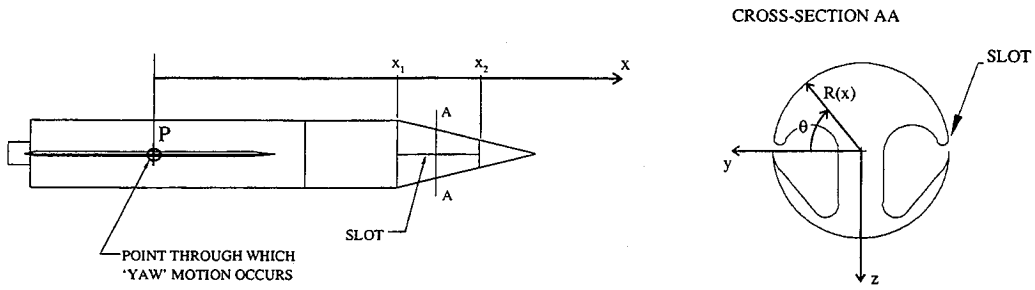

Figure 3.16: Definition of variables for cross-flow analysis of the wall-jet effect.

Assuming complete expansion of the jet, the quantity $\rho_j V_j^2$ which is a function of x and θ becomes independent of x, *i.e.*

$$\rho_j V_j^2(x,\theta) = \rho_j V_j^2(\theta) \tag{3.3}$$

Because of the assumption of two dimensional flow, the jet width function, w_j , can be written as

$$w_j(x,\theta) = f(\theta)\, w_j(x,\theta{=}0) = f(\theta)\, w_{slot}(x) \tag{3.4}$$

Note that f(θ) represents the jet width profile in the cross-flow plane for a slot of unit width and f(θ = 0) = 1.

Substituting Equations 3.3 and 3.4 into 3.2 yields,

$$C_{n_{wj}} = \frac{GA_{slot}}{q_\infty S_{ref}} \int_{\theta=0}^{\theta_{scp}} \rho_j V_j^2 f(\theta) \cos\theta \, d\theta \tag{3.5}$$

Where G is a constant that depends on the slot geometry and is given by:

$$G = \frac{1}{bA_{slot}} \int_{x_1}^{x_2} w_{slot}(x)\, x\, dx \tag{3.6}$$

If compressibility effects in the jet flow are assumed small, the quantity $\rho_j V_j f(\theta)$ is independent of θ and can be moved out of the integral in Equation 3.5. Further simplification is introduced by assuming that the jet is decelerated by friction proportional to the jet velocity. With this assumption the jet velocity profile is linear in θ.

$$V_j(\theta) = (1 - \frac{\theta}{\theta_{sep}}) V_{j_{slot}} \tag{3.7}$$

Including the above simplifications in Equation 3.5, and recalling that at the slot exit $\theta = 0$ and $f(\theta = 0) = 1$, yields

$$C_{n_{wj}} = C_\mu G \int_{\theta=0}^{\theta_{sep}} (1 - \frac{\theta}{\theta_{sep}}) \cos\theta \, d\theta = G \frac{1 - \cos\theta_{sep}}{\theta_{sep}} C_\mu \tag{3.8}$$

Equation 3.8 shows that the wall-jet effect on the yaw moment coefficient can be expressed as a function of the separation point times C_μ. A plot of the ratio $C_{n_{wj}}/C_\mu$ versus θ_{sep} is presented in Figure 3.17. It is seen that as the jet remains attached longer, the wall-jet effect becomes more significant.

In this work, the values used for C_μ are generally smaller than 0.03. Therefore, $C_\mu = 0.03$ is chosen as a typical value. Using a conservative value of 80 degrees for the separation angle, θ_{sep} , gives $C_{n_{wj}} \cong 0.02$. The average variation in the yaw moment coefficient generated by asymmetric blowing with intensity $C_\mu = 0.03$ is $\Delta C_n \cong 0.3$ (Figure 3.11). These results indicate that for $C_\mu = 0.03$ the contribution of the wall-jet effect to the yaw moment variation is less than 7%. This simplified analysis provides an estimate for the

wall-jet effect, and reveals that for the values of blowing used in this research this effect is of secondary importance.

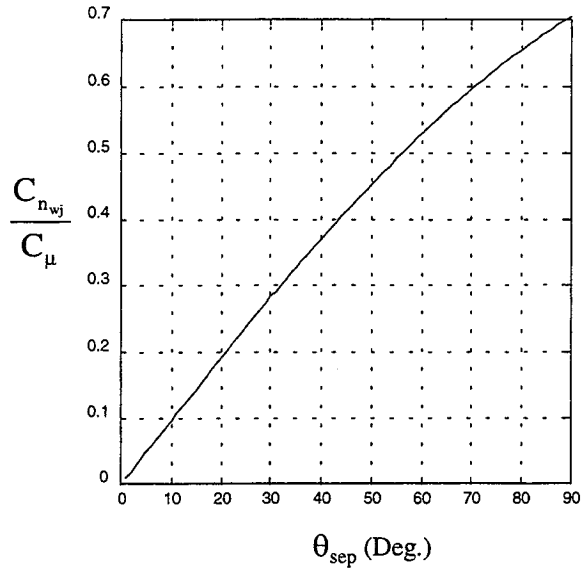

Figure 3.17: Wall-jet contribution for the yaw moment coefficient. Result from simplified analysis, Equation 3.7, with numerical values for the model used in the experiments.

3.4.3 Direct Jet Momentum

As the jet exits the slot, a force is applied to the model as a direct reaction to the jet momentum. This effect has no contribution to the yaw moment because the jet exit velocity is parallel to the yaw axis of the model. On the other hand, the roll moment generated by this direct momentum effect is given by:

$$C_{l_{dm}} = \frac{1}{q_\infty S_{ref} b \cos\varepsilon} \int_{x_1}^{x_2} \rho_j V_j^2 w_j R \, dx \tag{3.9}$$

Assuming two dimensional flow at stations where the slot is present, and complete expansion of the jet, the quantity $\rho_j V_j^2$ becomes independent of x and Equation 3.9 can be written as

$$C_{l_{dm}} = BC_{\mu} \tag{3.10}$$

B is a constant that depends on the geometry of the slot and of the model and is given by:

$$B = \frac{1}{A_{slot} b \cos\varepsilon} \int_{x_1}^{x_2} w_j(x) R(x)\, dx \tag{3.11}$$

For $C_{\mu} = 0.03$, the contribution to the roll moment coefficient is $C_{l_{dm}} = 0.003$. From the data in Figure 3.11 it is seen that this value is about one tenth of the total change in roll moment caused by $C_{\mu} = 0.03$. Hence, for the range of C_{μ} used in this research the direct jet momentum is a secondary effect with respect to the generation of roll moment.

3.5 Transient Response to Blowing

The following experiment was conducted to determine the transient response of roll and yaw moments to blowing. The wind tunnel model was clamped at specified roll and yaw angles and blowing was applied in the form of a step input. Data were recorded for C_{μ} and roll and yaw moments as a function of time. For this particular experiment, miniature pressure sensors located inside the plena were used to provide a time accurate measurement of C_{μ}. In this way, when relating roll and yaw moments to blowing, only the effects of the unsteady aerodynamics were included in the data. Note that, because the flowmeters were located outside of the test section, away from the plena, their measurements included effects of the air supply system dynamics and therefore, were not adequate as a means to isolate the aerodynamic transient effect.

Results from these experiments are presented in Figure 3.18 for the case where, $\phi = \gamma = 0$. Shown are the time histories for ΔC_{μ} and the variations in the roll and yaw moment coefficients, ΔC_l and ΔC_n respectively. It is seen that, roll and yaw moment responses lag

the curve for ΔC_μ . This is expected, since blowing was applied at the forebody and convection is necessary for the changes in the flow to affect stations downstream of the slots.

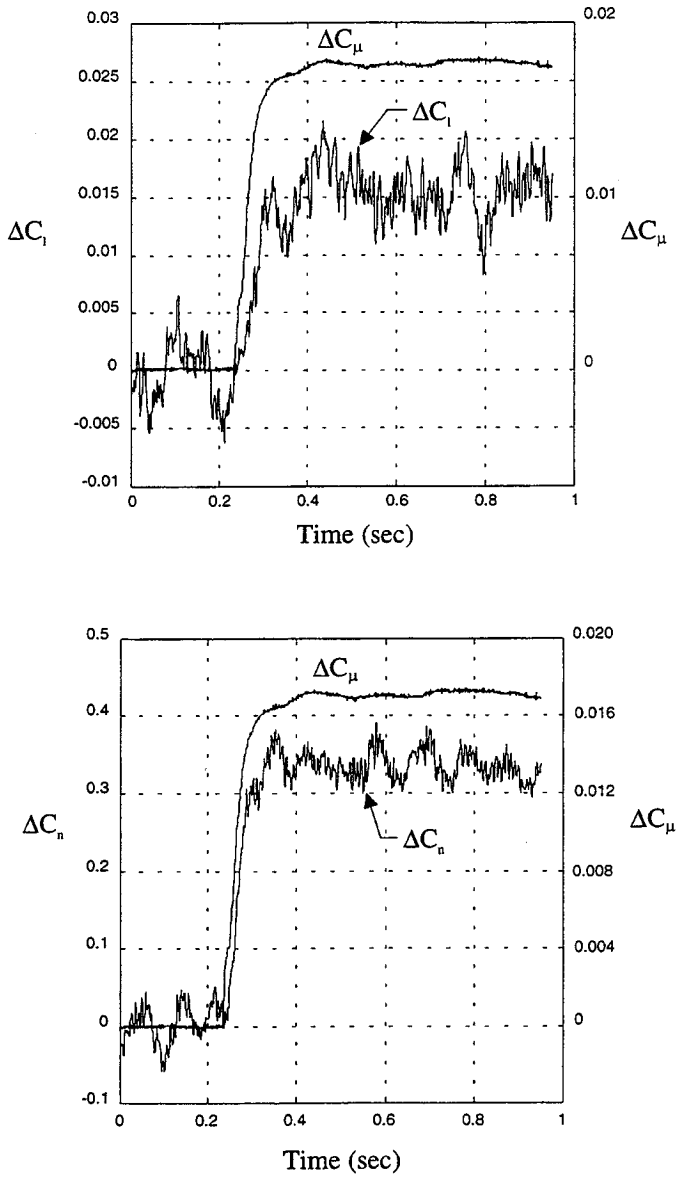

Figure 3.18: Roll and yaw moment transient responses to blowing. $\phi = \gamma = 0$. $\alpha_0 = 45$ degrees and $U_\infty = 19.5$ m/sec.

In Chapter 5, where an unsteady aerodynamic model is developed, it is shown that this lag effect can be represented by first order models characterized by time constants τ_l and τ_n. Values for these time constants, identified in Chapter 5, are:

$$\tau_l = 0.018 \pm 0.001 \text{ sec} \qquad \tau_n = 0.005 \pm 0.001 \text{ sec} \tag{3.12}$$

Where the error bounds are given in terms of one standard deviation. These results show that, the yaw moment response is about 3.5 times faster than the roll moment response.

Recall, from Section 3.3, that roll moment is generated only at stations where the wing is present, while yaw moment is generated at the fuselage. This explains the larger time constant for the roll moment response being caused by the fact that the wings are located at the rear portion of the model, and changes in the flow field caused by blowing have to travel downstream to affect the roll moment. This explanation suggests that the time it takes for a fluid particle to travel from the forebody to the rear of the model should approximate τ_l.

A convective time constant, τ_c , is defined in Equation 3.13 and its value calculated for the conditions of the experiment.

$$\tau_c \equiv \frac{\ell}{U_\infty \cos\alpha_0} = 0.016 \text{ sec} \tag{3.13}$$

Where ℓ is the distance between the slot mid-point and the rear of the model.

The value of 0.016 seconds obtained for τ_c is close to the 0.018 seconds obtained for τ_l. This suggests that the convective time can be used as an approximation to the time constant that characterizes the roll moment response. The faster response of the yaw moment indicates that a large contribution to C_n is generated near the forebody due to the partial recovery of attached flow, and the change in the vortices strengths and positions

3.6 Natural Motion

The natural motion of the two degrees-of-freedom system is shown in Figure 3.19. The model was released from $\phi \cong 1.5$ degrees, $\gamma \cong 0$ and zero roll and yaw rates. No blowing was applied during this experiment. Because of mechanical limits and safety reasons, the motion was stopped when γ approached 20 degrees. The plots demonstrate that the system is dynamically unstable. Its natural motion is divergent. This result clearly demonstrates the need of an approach to stabilize and control the system.

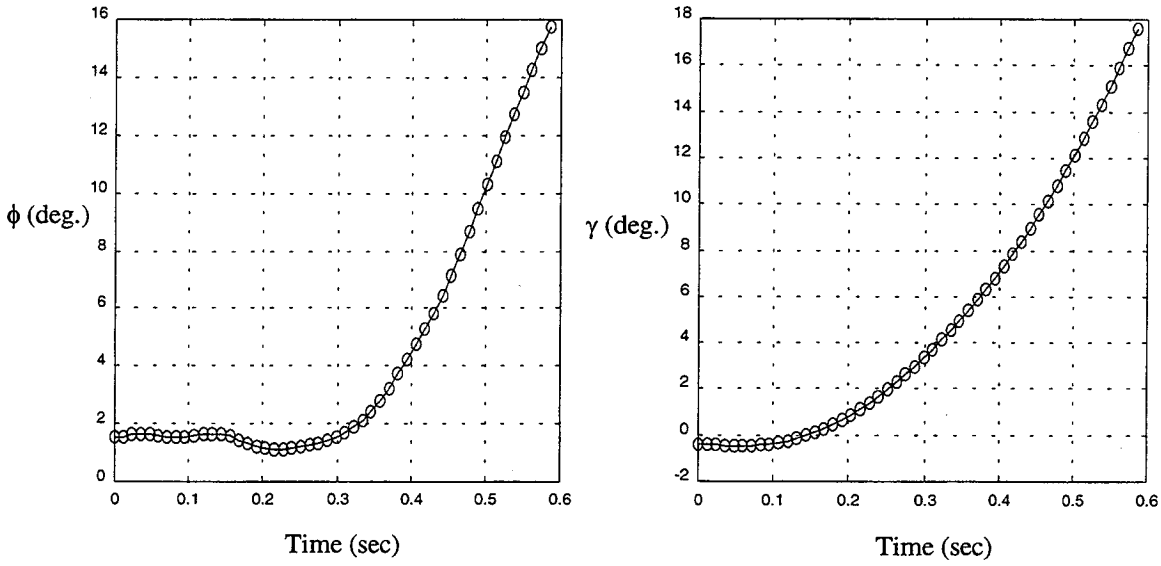

Figure 3.19: Natural motion of the two degrees-of-freedom system. $\alpha_0 = 45$ degrees and $U_\infty = 19.5$ m/sec.

3.7 Summary

In this chapter, results from several experiments have been presented and analyzed to provide insight into the aerodynamic phenomena. In particular, the effects of forebody tangential blowing on the roll and yaw moments have been determined. The following is a summary of the main results and observations.

Flow visualization experiments revealed that the flow is characterized by asymmetric vortical structures over the entire length of the vehicle. The asymmetry starts at the forebody where two distinct vortices are observed. For stations of the model where the wings are present, the flow is characterized by a dominant three-vortex structure. Asymmetric blowing changes the positions and strengths of the vortices. Symmetric blowing produces partial recovery of attached flow on the forebody, and changes the three-vortex structure over the wings into a more symmetric two vortex-structure.

Comparison of the aerodynamic loads for the wind tunnel model with a conical versus a blunt forebody tip indicated that the flow asymmetry is caused by small geometric imperfections of the conical forebody. Small amounts of blowing have an effect similar to the geometric imperfections and can significantly alter the flow asymmetry.

Measurements of the static roll and yaw moments showed that: (1) The characteristics of the vehicle depend on the blowing intensity. (2) The effects of blowing on the roll and yaw moments are a function of the vehicle attitude, *i.e.* roll and yaw angles. (3) Asymmetric forebody tangential blowing is a highly non-linear actuator, especially in the regions of small blowing intensities. (4) Symmetric blowing alleviates lateral loads. Moreover, superimposing symmetric and asymmetric blowing linearizes the blowing effects on roll and yaw moments.

Analysis of the experimental data and simplified modeling of the jet effects showed that the displacement of separation lines is the main mechanism through which blowing alter the loads acting on the vehicle. The other identified mechanisms are the wall-jet effect and the direct jet momentum. For the range of blowing used in this research, the contributions from wall-jet effect and direct jet momentum are an order of magnitude smaller than the effect of the displacement of the separation lines.

Measurement of transient aerodynamic loads showed that the roll and yaw moment responses lag the blowing input. The lags can be represented by first order models

characterized by time constants. The time constant for the roll moment can be approximated by the time it takes for a fluid particle to travel from the forebody to the rear of the model. For the model configuration used in these experiments, the yaw moment response to blowing is about 3.5 times faster than the roll moment response. This difference in time constants was explained by the different mechanisms through which roll and yaw moments are generated.

Results from dynamic experiments showed that the two degrees-of-freedom system is unstable. Its natural motion is divergent. This demonstrates the need for control.

These results are used to help formulate and verify the aerodynamic model that is developed in the next two chapters.

Chapter 4

Discrete Vortex Model

In this chapter a steady-state aerodynamic model based on first principles is presented. The objective is to obtain a description of the aerodynamics that captures the main physics of the flow, explains the experimental results, and is suitable for the design and implementation of control logic. The model is developed within the framework of slender body theory, and uses discrete vortices to model the separated flow. It incorporates both boundary-layer separation on the forebody and separation at the sharp leading-edges of the wings. The development of this steady-state discrete vortex model is presented, and experimental observations are used to support the basic assumptions included in the mathematical formulation. In implementing and using the aerodynamic model, several numerical problems were identified. The techniques used to alleviate those problems are discussed in detail. Results from the model were compared with experimental results to verify the validity of the aerodynamic model and determine its applicability as a prediction tool. It is shown that, the model captures the interactions between forebody and wing vortices, and provides proper representation of the large scale flow structure. Predicted roll and yaw moments are in qualitative agreement with experiments, but numerical differences exist which limit its use as a prediction tool.

The chapter is organized as follows: Section 4.1 contains a discussion of various theoretical methods used to describe the aerodynamics in the high angle of attack regime.

This provides a context for the selection of the modeling approach used in this work. In Section 4.2, the main components of the discrete vortex method are described in detail. In Section 4.3, the implementation of the method is discussed, as well as the numerical problems encountered and the methods used to mitigate those problems. Results obtained with the aerodynamic model are presented in Section 4.4, and are compared with experimental data to validate the model and determine its limits of application. A conclusion to the chapter is presented in Section 4.5.

4.1 Introduction

The governing equations obtained from the theoretical analysis of a fluid-dynamics problem depend on the simplifying assumptions made in the formulation of the problem. The most accurate representation is through the Navier-Stokes equations. They incorporate compressibility and viscosity effects. For laminar flows the viscous laws are known and the results from the equations are correct. For transitional and turbulent flows the viscous laws are not well known and the accuracy of the solutions depends on the approximations used for the viscous effects. If the flow is assumed inviscid, the Euler equations are obtained. However, in solving these equations, there are several issues such as the effects of numerical dissipation and grid resolution which can be significant [17, 23], and create difficulties in separating physical from numerical effects. The potential equation is obtained if the flow is assumed irrotational. Vortex-lattice methods and panel methods are used to solve three-dimensional potential flow problems [24]. If the vehicle is slender, the axial variation of the axial velocity is much smaller than the lateral variations of the lateral velocities, and the linearized potential equation reduces to the Laplace's equation. This formulation is known as Slender Body Theory [25, 26, 27, 28]. In this case the solution to a steady three-dimensional problem is approximated by the solution to an equivalent unsteady two-dimensional problem in the cross-flow plane. The discrete vortex model presented in this chapter falls under the Slender Body Theory. This selection for the formulation of an aerodynamic model is

discussed in the following paragraphs in view of the flow characteristics observed experimentally and of the configuration of the wind tunnel model.

Results from flow visualization experiments showed that the flow field was characterized by vortical structures over the whole length of the wind tunnel model. The axial scan experiments, presented in Section 3.1.1, did not reveal a sudden change in vortex diameter, which is characteristic of vortex breakdown. This evidence suggests that the separated flow was dominated by a vortical field.

Potential flow theory has been extensively used to represent flows dominated by vortices [24]. The basic assumption is that viscous effects are only important in a small region near the center of the vortex, known as the vortex core, and in regions near the surface of the vehicle, *i.e.* the boundary layer. Under this assumption, potential flow theory can be used to describe the flow everywhere outside the boundary layer and the core of the vortices.

The geometry of the wind tunnel model is elongated. The delta wings have a large sweep angle, $\Lambda = 70$ degrees, and small aspect ratio, $AR = 1.46$. Therefore, it is expected that slender body theory provides an adequate framework to calculate the flow field and the aerodynamic characteristics for the experiments conducted in this research.

It should be noted that even if vortex breakdown occurs it is reasonable to use a vortical field to represent the flow because the experiments revealed the existence of a vortical flow structure. The mechanisms of vortex breakdown are not yet fully understood, and a theory to predict its occurrence and its effects on the aerodynamic characteristic of aircraft does not exist. It is generally agreed that vortex breakdown is characterized by an increase in the size of the vortex core, and a diffusion of vorticity over a larger region. A detailed discussion of the phenomena is given by Wedemeyer [29], and its effects on the aerodynamic loads of delta wings were studied by Hummel and Srinivasan [30].

4.2 Discrete Vortex Method

The basic idea of the discrete vortex method presented here is to solve a three dimensional problem for an equivalent axisymmetric body subject to the axial component of the flow, and a two-dimensional problem for the cross-flow component. This represents a partition of the original problem into two simpler ones as indicated in Figure 4.1. The combined velocity field from the two solutions is used to calculate an absolute pressure field from which the loads acting on the vehicle are obtained. The cross-flow solution encompasses the component of the freestream velocity in the cross-flow plane, a doublet to represent the cross-section of the vehicle in the circle plane, and vortices to represent the separated flow. The cross-flow solution is obtained in several sections along the length of the vehicle taking into account the effect of the upstream separated flow. In this way, the assumption of conical flow is not required.

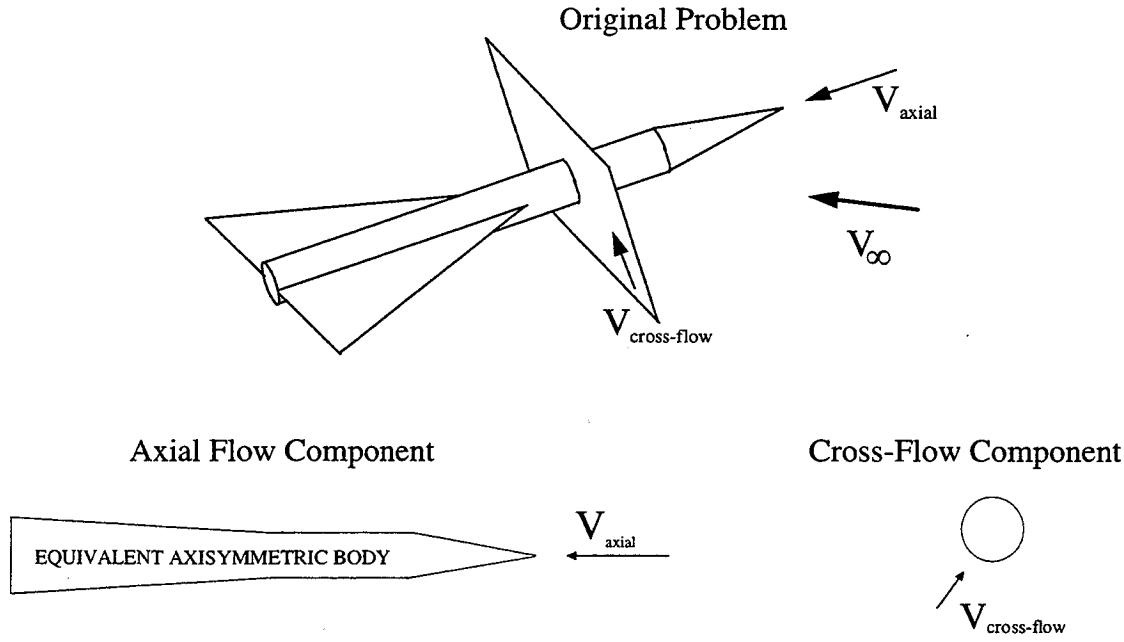

Figure 4.1: Slender body theory. Partition of original problem into axial and cross-flow components.

Methods that use discrete vortices to represent the separated flow are known as discrete vortex methods and have been used extensively to model separated flows. In particular, Sacks *et al* [31] used a discrete vortex model to calculate the normal force and center of pressure on wing-body combinations exhibiting leading-edge separation. Angles of attack of up to 20 degrees were studied and forebody separation was not considered. Mendenhall *et al* [32, 33] used a similar idea of releasing vortices into the freestream to represent the separated flow over slender bodies at high angles of incidence, $\alpha \leq 37.5$ degrees. An important feature of their model is the inclusion of a boundary layer type of separation that occurs at the surface of the slender body. Semi-empirical flat plate separation criteria derived by Stratford [34] were used to predict laminar and turbulent separation.

In the present research, the geometry of the vehicle and the flight conditions create a more complex problem in which forebody and wing vortices interact to generate an asymmetric flow structure. The problem is further complicated by the addition of blowing. To address these issues, the aerodynamic model presented here includes both boundary-layer separation at the forebody of the vehicle, and leading-edge separation at the wings.

In the analysis to follow the flow is assumed to be incompressible. This is appropriate for the experimental conditions used in this work where the freestream Mach number is low, $M_\infty \cong 0.06$. Extension of the method to higher Mach numbers requires corrections for compressibility effects. Those can be found in many textbooks on fluid dynamics.

4.2.1 Axial Flow Component

In solving for the axial component of the flow, the vehicle is approximated by an equivalent axisymmetric body of the same cross-sectional area. This is known as the body or volume problem. Selection of a proper coordinate frame makes it possible to solve this three-dimensional problem in two variables. Figure 4.2 shows the cylindrical coordinates

η, r and φ used in formulating the problem. Because of the axisymmetry, flow quantities are independent of φ and the problem can be solved in two dimensions, η and r.

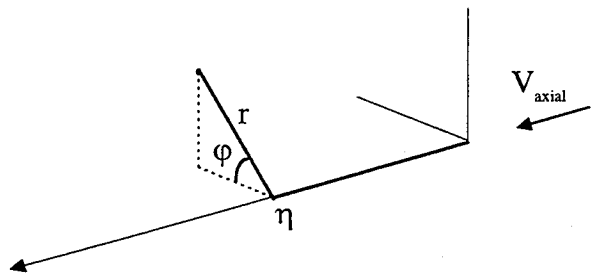

Figure 4.2: Cylindrical coordinates used in the solution of the volume problem.

If the motion is irrotational, a velocity potential, Φ, always exists from which the velocity components are obtained

$$\vartheta_\eta = \frac{\partial \Phi}{\partial \eta} \qquad \vartheta_r = \frac{\partial \Phi}{\partial r} \qquad \vartheta_\varphi = \frac{1}{r}\frac{\partial \Phi}{\partial \varphi} \tag{4.1}$$

A distribution of three-dimensional discrete sources and sinks placed along the longitudinal axis can be used to represent an axisymmetric body in uniform flow. The velocity potential for a three-dimensional uniform flow along η plus q three-dimensional sources of strength Q_k located at η_k on the longitudinal axis is

$$\Phi = \eta V_{axial} - \frac{1}{4\pi}\sum_{k=1}^{q} \frac{Q_k}{\sqrt{(\eta - \eta_k)^2 + r^2}} \tag{4.2}$$

Where Q_k is the flux of a fluid with unit density. $Q_k > 0$ represents a source and $Q_k < 0$ a sink.

The solution to the body problem is obtained by arbitrarily placing q sources along the body symmetry axis and solving for their strengths. One equation is obtained from the fact that the total source strength within the volume of a closed body is zero. Two other equations result because the flow is considered attached, and the tip and tail of the model are stagnation points. The missing $q-3$ equations are obtained by applying the boundary condition, *i.e.* at the body's surface the resulting flow should be tangent to the body, to $q-3$ points along the body. The result is a set of q linear equations that can be solved for the source strengths, Q_k.

In this work, 64 point sources were used to represent the equivalent body. The first source was placed at 0.00254 m (0.1 inches) from the tip of the forebody. The other sources were placed downstream at distances equal to 0.6 times the local radius of the cross-sectional circumference. Boundary conditions were satisfied at points midway between the source locations.

The concept of a stream function, Ψ, which is defined for two-dimensional flows can be extended for three-dimensional flows which are axisymmetrical [35]. The shape of the body that results from its representation through the discrete sources is given by making the stream function equal to zero. The stream function for the axial uniform flow and the q point sources is

$$\Psi = -\frac{1}{2}r^2 V_{axial} + \frac{1}{4\pi}\sum_{k=1}^{q}\frac{Q_k(\eta-\eta_k)}{\sqrt{(\eta-\eta_k)^2+r^2}} \tag{4.3}$$

The resulting equivalent body is shown in Figure 4.3. Note that a conical section was used to close the rear end of the body. Also shown are streamlines determined by numerically solving Equation 4.3 for various values of Ψ.

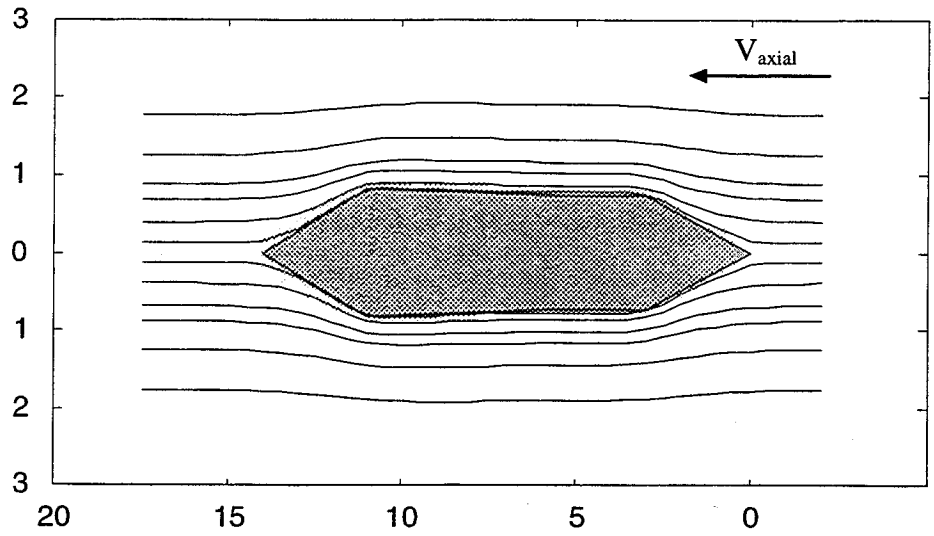

Figure 4.3: Equivalent body and streamlines obtained from the calculated distribution of three-dimensional sources.

4.2.2 Cross-Flow Component

In solving for the two-dimensional velocity field due to the cross-flow component, it is convenient to define the complex potential

$$\omega(z) = \Phi + i\,\Psi \tag{4.4}$$

Where $z = x + i\,y$ is the complex variable. The velocity components are obtained from the complex potential through the relationship

$$\frac{d\omega}{dz} = u - i\,v \tag{4.5}$$

The cross-flow solution consists of superimposing the simple flows, which are solutions to Laplace's equation, to obtain the complex separated flow observed in the experiments. The cylinder in uniform flow is used to represent the attached flow and various discrete vortices are used to model the separated wake. For stations of the model where the wing

is present the cross-section is mapped into a circle and the known solution for a cylinder in uniform flow can be applied.

In order to satisfy boundary conditions each vortex placed into the flow requires an image vortex to be introduced inside the cylinder. The circulation, Γ, associated with a vortex provides a measure of the vortex strength. For a vortex of strength Γ_k placed at a position ν_k in the circle plane, an image vortex of strength $-\Gamma_k$ is introduced at ν_{-k} given by:

$$\nu_{-k} = \frac{c^2}{\bar{\nu}_k} \tag{4.6}$$

Where c is the radius of the cross-section in the circle plane. According to the circle theorem[1], a vortex of strength Γ_k is required at the center of the circle. This vortex does not affect the boundary conditions and is introduced or omitted solely on the basis of conservation of vorticity. Therefore, in the cross-section where the vortex is generated the center image is omitted. For vortices originated at stations upstream, the center image is used to account for the net vorticity that is brought to the current cross-section.

In the circle plane, the complex potential for the cross-section in the presence of n vortices of which n–2 are originated upstream of the given cross-section is

$$\omega(\nu) = V_x(\nu + \frac{c^2}{\nu}) - iV_y(\nu - \frac{c^2}{\nu}) - \sum_{k=1}^{n} i\frac{\Gamma_k}{2\pi}\ln(\nu - \nu_k) + \sum_{k=1}^{n} i\frac{\Gamma_k}{2\pi}\ln(\nu - \nu_{-k}) - \sum_{k=1}^{n-2} i\frac{\Gamma_k}{2\pi}\ln\nu \tag{4.7}$$

Where V_x and V_y are the components of the cross-flow freestream velocity $V_{\text{cross-flow}}$ on the real and imaginary axis respectively.

---

[1] See Milne-Thompson [35], p.154, 362.

In the real or physical plane the velocity components u_c and v_c at a generic point, due to the cross-flow solution, are obtained from the complex potential as

$$u_c - i\,v_c = \frac{d\omega}{dz} = \frac{d\omega}{d\nu}\frac{d\nu}{dz} \tag{4.8}$$

$d\omega/d\nu$ is calculated from Equation 4.7 and $d\nu/dz$ is calculated from the function used to map the real cross-section into a circle.

Conformal Mapping

The region outside the wing-body cross-section can be mapped into the region outside of a circle using the following conformal transformation.

$$\left(z+\frac{a^2}{z}\right)^2 = \left(\nu+\frac{c^2}{\nu}\right)^2 - \left(s-\frac{a^2}{s}\right)^2 \tag{4.9}$$

As shown in Figure 4.4, a is the radius of the fuselage, s is the local semi-span in the z-plane, and $c = \frac{s^2+a^2}{2s}$ is the radius of the circle in the ν-plane.

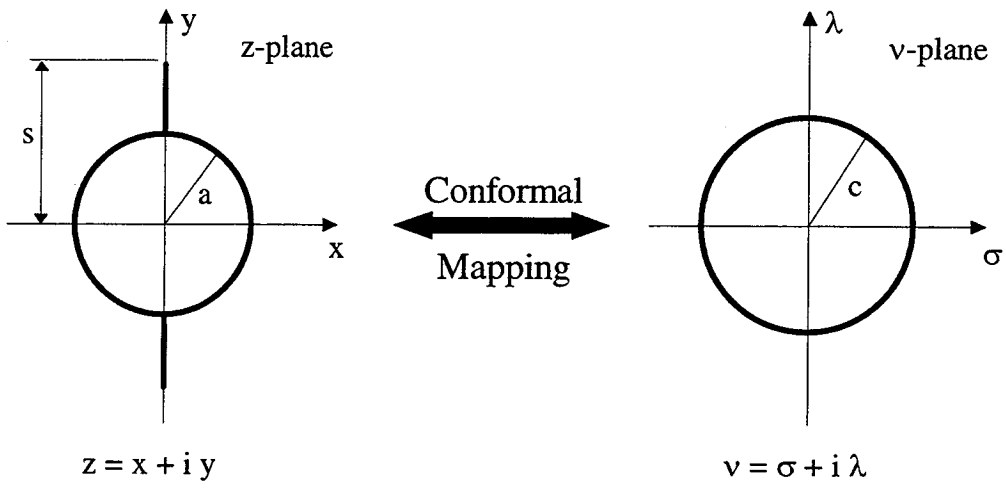

Figure 4.4: Conformal mapping. Definition of variables.

Similar transformations exist for more complex geometric forms. For example, the transformation for a fuselage of elliptic cross-section with wings and vertical fins can be found in References [36, 37]. A method to compute a conformal transformation for cross-sections of arbitrary shape is given by Skulsky [38].

4.2.3 Velocity Field and Vortex Motion

The resulting velocity field is obtained by the vector addition of the solution to the volume problem and the solution to the cross-flow problem. The total velocity, $\mathbf{v} = u\hat{x} + v\hat{y} + w\hat{z}$, at a generic point in the flow is given in terms of its components as

$$u = u_r + u_c \qquad v = v_r + v_c \qquad w = -\vartheta_\eta \tag{4.10}$$

ϑ_η is the velocity component along the model longitudinal axis and is obtained from the solution to the body problem. The vector $\hat{z}$ is oriented in the opposite direction of η. u_c and v_c are the contributions of the cross-flow solution given by Equation 4.8. u_r and v_r are the components of ϑ_r, in the x and y directions respectively, *i.e.*

$$\vartheta_r = u_r + i\, v_r \tag{4.11}$$

The motion of the discrete vortices, used to represent the separated flow, depends on the velocity field which in turn is determined by the freestream velocity, the shape of the model and the strengths and positions of the vortices. The velocity at the center of a vortex Γ_k can be calculated using the previously developed expressions for the velocity at a generic point in the flow. The only difference is that, in Equation 4.7 the contribution due to Γ_k is omitted, *i.e.* the vortex does not induce any velocity at its own center. The equations of motion for the vortex Γ_k are

$$\frac{dx_k}{d\eta_k} = \frac{u_k}{V_{axial} + \vartheta_{\eta_k}} \qquad \frac{dy_k}{d\eta_k} = \frac{v_k}{V_{axial} + \vartheta_{\eta_k}} \tag{4.12}$$

The motion of each vortex in the flow field is determined by two differential equations given by 4.12. At a certain station where n vortices are present in the flow field there are 2n differential equations that need to be solved simultaneously. These equations were integrated numerically to determine the motion of the vortices and ultimately the characteristics of the flow field.

4.2.4 Pressure Field

The pressure p_o at a point O in the flow field can be calculated using the Bernoulli equation for irrotational flow [39]

$$p_\infty + \frac{1}{2}\rho_\infty V_\infty^2 + \rho_\infty \left.\frac{d\Phi}{dt}\right|_\infty = p_o + \frac{1}{2}\rho_o V_o^2 + \rho_o \left.\frac{d\Phi}{dt}\right|_o \tag{4.13}$$

For a steady uniform flow upstream of the model, the last term on the left side of the equation is zero. In terms of the pressure coefficient C_p, Equation 4.13 is

$$C_p\Big|_o \equiv \frac{p_o - p_\infty}{q_\infty} = 1 - \left(\frac{V_o}{V_\infty}\right)^2 - \frac{2}{V_o^2}\left.\frac{d\Phi}{dt}\right|_o \tag{4.14}$$

In calculating the time derivative of the velocity potential, the following approximation was used

$$\frac{d\Phi}{dt} = \frac{d\eta}{dt}\frac{d\Phi}{d\eta} \cong V_{axial}\frac{d\Phi}{d\eta} \tag{4.15}$$

The term $d\Phi/d\eta$ is obtained from the complex potential given in Equation 4.7. Of particular interest are the values of C_p at the surface of the vehicle. These values are used to evaluate the separation criteria and to calculate the aerodynamic loads.

4.2.5 Vortex Shedding

A boundary layer type of separation occurs at the forebody of the wind tunnel model. It is necessary to calculate the positions where separation occurs and the amount of vorticity that is shed into the flow. For stations where the wing is present the separation point is fixed at the sharp leading-edges and a method to compute the vorticity released into the flow is required. The calculations involved in computing these two types of separations are described next.

Boundary-Layer Separation

A rigorous solution for the flow separation on the forebody requires solving the equations for the three-dimensional boundary layer. This would increase the complexity and required computational time of the aerodynamic model. Moreover, Mendenhall and Lesieutre [32] proposed an approximate method of computing the separation over a slender body at high angles of attack which produces results that are in reasonable agreement with experiments. Therefore, in this work, the calculation of the separation at the forebody follows the method of Mendenhall and Lesieutre [32]. Only the primary separation was considered. Semi-empirical separation criteria, developed by Stratford [34] for two-dimensional flows over a flat plate, were used to determine the separation point at a given cross-section of the forebody. The criteria are based on the cross-sectional pressure distribution and are modified to account for three-dimensional effects. Once the separation point is determined, the local velocity is used to compute the amount of vorticity that is shed into the flow.

According to Marshall and Deffenbaugh [40], the vorticity flux across the boundary layer assuming a no slip condition at the wall is given by

$$\frac{d\Gamma}{dt} = \frac{V_{c_s}^2}{2} \tag{4.16}$$

Where, $V_{c_s} = \sqrt{u_{c_s}^2 + v_{c_s}^2}$, is the magnitude of the cross-flow velocity at the separation point. The components u_c and v_c are calculated using Equation 4.8. The vorticity flux is

assumed constant over a period of time Δt and integrated to generate a discrete vortex of intensity, Γ, given by

$$\Gamma = \frac{V_{cs}^2}{2}\Delta t \cong \frac{V_{cs}^2}{2}\frac{\Delta\eta}{V_{axial}} \tag{4.17}$$

The approximation is justified on the basis of slender body theory which assumes that the disturbances on the axial component of the velocity are small. With the strengths given by the previous equation, the position of the new vortices are calculated such that the resulting cross-flow velocity at the separation points are zero.

Leading-Edge Separation

For stations downstream of the forebody the separation point is fixed at the sharp leading-edges of the wing. In this case, the boundary layer transport theorem can not be used to calculate the vorticity that is shed into the flow. The velocity at the leading-edge of the wing should be finite, this is known as the Kutta condition. The requirement of finite velocity on the z-plane translates into zero velocity in the ν-plane because the derivative $d\nu/dz$ is singular when evaluated at the leading-edge.

It is necessary to solve for the vortex strength and position but only one equation is available from the Kutta condition. To resolve this problem either the strength or position of the new vortex need to be specified. The approach taken here consists of assuming that the new vortex will travel in the cross-flow plane with a velocity proportional to an average velocity near the tip of the wing on the pressure side. The position of the new vortex is determined by the product of this average velocity, $\bar{v}$, by the time interval $\Delta t = \Delta\eta/V_{axial}$, where $\Delta\eta$ is the longitudinal distance between consecutive cross-sections. This is illustrated in Figure 4.5, where δ is the distance in the z-plane between the new vortex and the wing tip. Once the vortex position is known, it is mapped to the circle plane and the Kutta condition is applied at the wing leading-edges.

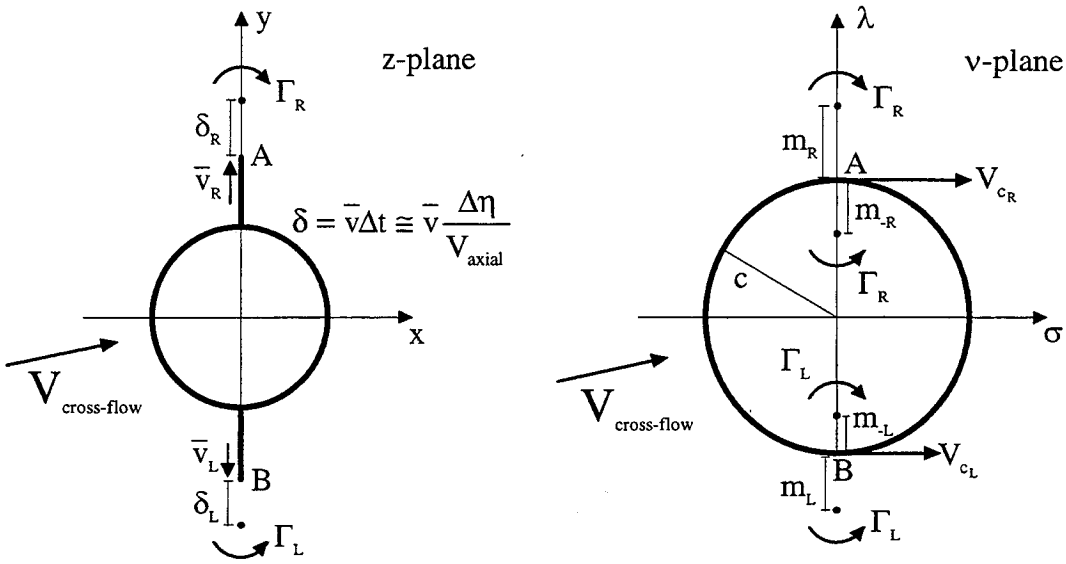

Figure 4.5: Position of new vortices generated at wing leading-edges.

At a given cross-section, two new vortices are generated one at each wing tip. In this case, because the new vortices lie in the plane of the wing their strengths can be calculated directly by applying the Kutta condition at the two wing tips. According to the nomenclature used in Figure 4.5, Γ_R and Γ_L are obtained from

$$\begin{aligned} |\Gamma_R|\left(\frac{1}{m_R}+\frac{1}{m_{-R}}\right)+|\Gamma_L|\left(\frac{1}{2c+m_L}-\frac{1}{2c-m_{-L}}\right) &= 2\pi V_{c_R} \\ |\Gamma_R|\left(\frac{1}{2c+m_R}-\frac{1}{2c-m_{-R}}\right)+|\Gamma_L|\left(\frac{1}{m_L}+\frac{1}{m_{-L}}\right) &= 2\pi V_{c_L} \end{aligned} \qquad (4.18)$$

4.3 Implementation

A FORTRAN program was written to implement the aerodynamic model described in the previous sections. The general flow of computations is shown in Figure 4.6. The vehicle geometry is specified in the main program. Flight conditions, axial position of the first station and the interval between consecutive stations are specified through an input file.

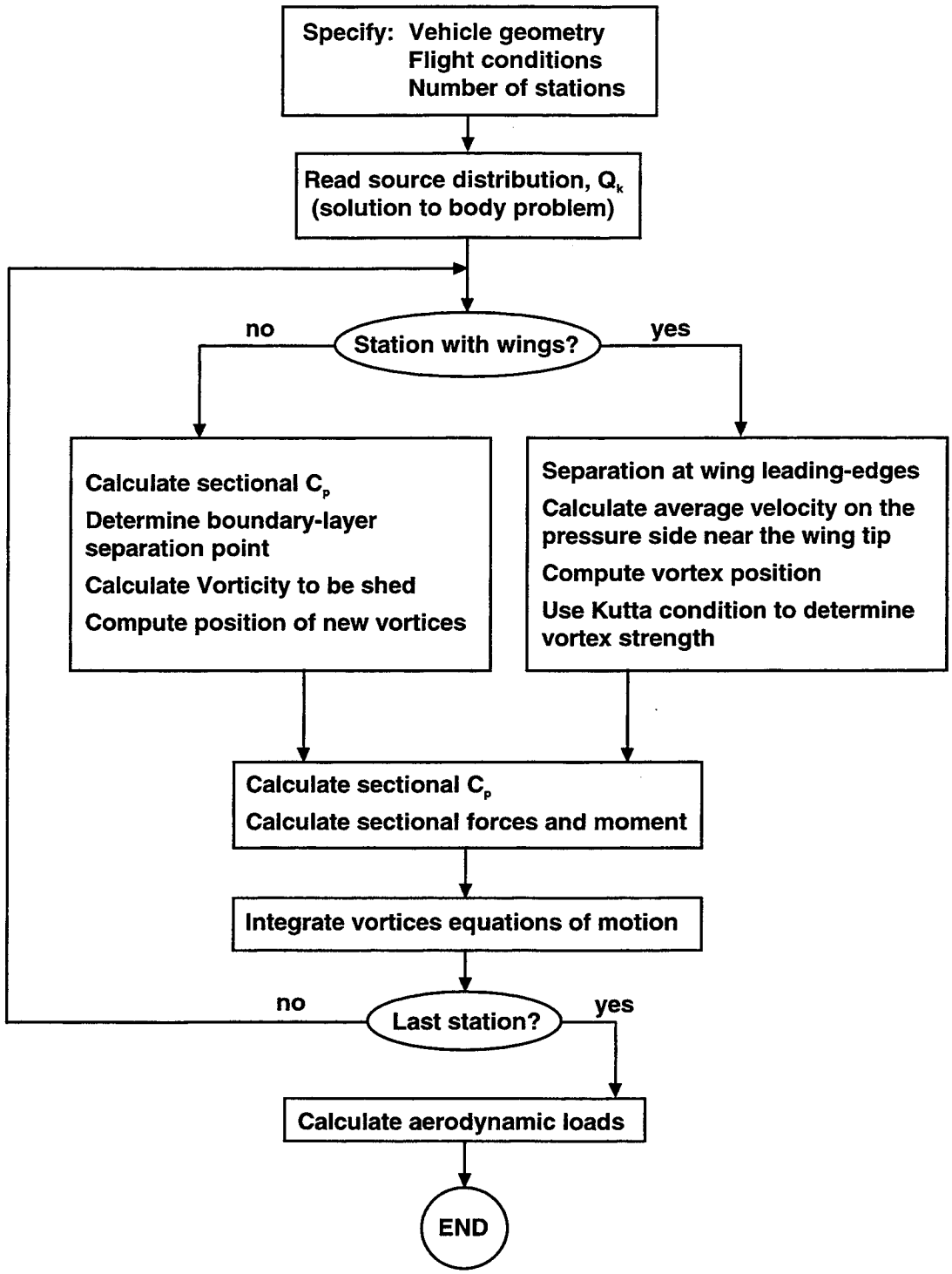

Figure 4.6: Discrete vortex model implementation. Flow of calculations.

The solution to the axial component of the flow was obtained using a separate program which calculates the distribution of sources for unit axial velocity, $\overline{Q}_k$, and saves the results in a data file. The main program reads the source distribution and adjusts their strengths to the current value of the axial component of the velocity, $Q_k = V_{axial}\overline{Q}_k$. Separate subroutines perform the mapping, calculate the vortex velocity and integrate the vortex equations of motion. A Kutta-Merson integration scheme with automatic variable step size was used to calculate the motion of the vortices. The value of the pressure coefficient, C_p, is calculated in the main program and used to compute the separation points. The pressure distribution is integrated in each cross-section to produce sectional forces and roll moment. Further integration along the length of the vehicle is conducted to generate the total aerodynamic loads.

Several issues have been addressed during the implementation of the method. They range from numerical problems to inherent limitations of the current approach. A discussion of some of these issues is important for the understanding and application of the method and is presented next.

4.3.1 Potential Vortex

The velocity induced by the potential vortex near its center is very large and is singular at the center of the vortex. This causes the following problems:

Mutual Orbiting. When two vortices are close, one induces a large tangential velocity on the other and the vortices start an orbiting motion. This causes large variations on the unsteady pressure term, $d\Phi/dt$, and consequently the values obtained for C_p are not reliable. To address this problem when two vortices get closer than a pre-specified distance, they are combined into a single vortex. The strength of the resulting vortex is equal to the sum of the individual strengths and its position is given by the average position of the individual vortices weighted by their strengths.

Surface Proximity. If a vortex gets too close to the surface of the vehicle it will induce large local velocities and the pressure distribution will be affected accordingly. This results in abrupt changes in C_p which are not consistent with experimental data. To avoid this problem when a vortex gets too close to the surface it is removed from the solution. This is justified because if a vortex is close to the surface, so is its image and their effects cancel except in a small region between them.

Number of Vortices. A large number of vortices is desired to produce a detailed representation of the separated flow. Increasing the number of cross-sections increases the number of vortices but the problems of mutual orbiting and surface proximity become more severe. Also, the integration of the vortices' equations of motion becomes more difficult. Simply increasing the number of vortices does not produce better results. There is a point beyond which numerical problems become dominant and a considerable number of vortices are merged together or are eliminated from the flow due to surface proximity.

Problems like mutual orbiting and surface proximity are inherent to the method in that they are caused by the discretization of a continuous quantity, the vorticity. They are made worse by the potential vortex model and its large induced velocities near the vortex center. Combining vortices and removing them from the flow are means of minimizing numerical problems. The results can be improved if a more realistic model is used for the vortex.

4.3.2 Viscous Vortex

Milne-Thomson [35] calculated the decay of vorticity for a viscous two-dimensional vortex. The tangential velocity induced by this vortex at a distance r from its center is

$$\vartheta_\theta = \frac{\Gamma}{2\pi r}\left(1 - e^{\frac{-r^2}{4\nu t}}\right) \tag{4.19}$$

Where ν is the kinematic viscosity and t is the time measured from the instant the vortex is originated. This is a non-potential vortex and its characteristics change with time. A simplified version was introduced by Mendenhal [32] which uses an average radius for the vortex core, r_c. In this case the tangential velocity is

$$\vartheta_\theta = \frac{\Gamma}{2\pi r}\left(1 - e^{-1.256\left(\frac{r}{r_c}\right)^2}\right) \tag{4.20}$$

This is a non-potential vortex and it is not a solution to the Laplace equation. Consequently, boundary conditions are not satisfied. This is a severe limitation only in the region near the core of the vortex. For distances larger than 2 r_c the difference in ϑ_θ calculated from Equation 4.20 and the one given by a potential vortex is less than 0.7%. This justifies using this vortex model provided that care is taken in choosing the radius r_c small enough that the boundary conditions are still satisfied.

The vortex model of Equation 4.20 was implemented in the program and the vortex core radius, r_c , is specified by the user. Proper selection of the radius r_c alleviates numerical problems and allows use of more stringent criteria for merging and removing vortices. Vortices Γ_i and Γ_k are combined if their distance is less than d_{ik}. Vortex Γ_i is removed from the flow if its distance to the surface is less than d_i. Table 4.1 lists guidelines for selecting r_c , and the criteria used for merging and removing vortices from the flow.

Parameter	Suggested Values
r_c	0.05c to 0.10c
d_{ik}	0.01c
d_i	0.05c to 0.15c

Table 4.1: Suggested values for parameters used in the program.

4.3.3 Laminar Versus Turbulent Separation

For sections along the forebody, it is necessary to determine if the boundary layer separation is laminar or turbulent. Reference [33] indicates that it is possible to correlate the type of separation, *i.e.* laminar or turbulent, with the Reynolds number defined as

$$\mathrm{Rey}_{\eta} \equiv \frac{V_{\infty} \sin\alpha\, \eta}{\nu} \tag{4.21}$$

Where η is the distance from the cross-section to the tip of the forebody and $\nu = 14.4 \times 10^{-6}$ m^2/sec is the kinematic viscosity. Laminar separation occurs for lower values of the Reynolds number, Rey_{η} , and turbulent separation for Rey_{η} larger than 700,000. It should be noted that this criteria is approximate, it was obtained through correlation of a limited number of experimental results. Therefore it should be used only as a guideline.

For the experiments conducted in this research the freestream velocity was 19.5 m/sec and the nominal incidence angle, α_0 , was 45 degrees. The maximum value of η is 0.144 m (5.65 inches) and corresponds to the forebody station most distant from the nose. Using these values results in

$$\mathrm{Rey}_{\eta}\Big|_{\mathrm{max.}} \cong 140{,}000 \tag{4.22}$$

This result indicates that according to the criteria of Reference [33] laminar separation should occur at the forebody. Moreover, since the maximum value of Rey_{η} is significantly smaller than the value suggested in the criteria, laminar separation was assumed. Unless otherwise specified, the results that follow were obtained using the separation criteria for a laminar boundary-layer.

4.4 Results

The results presented in this section were obtained using the discrete vortex model, DVM, for $\alpha_0 = 45$ degrees and $U_\infty = 19.5$ m/sec, which are the same as the experimental test conditions.

4.4.1 Predicted Flow Structure

The position of the vortices and the pressure distribution on various cross-sections are shown in Figure 4.7 for $\phi = \gamma = 0$. Each circle represents a clockwise rotating vortex and each cross a counter-clockwise one. Solid squares are used to represent the centers of vorticity of clockwise and of counter-clockwise vortices. Dashed lines show the calculated pressure coefficient in the pressure side of model and solid lines on the leeside.

The DVM indicates that separation occurs at all cross-sections on the forebody which is, in fact, observed experimentally. The calculated position of the separation lines differs from experiments. As seen, the method predicts symmetric flow for symmetric flight conditions. This is in disagreement with experimental data presented in Chapter 3, which clearly shows asymmetric flow for $\phi = \gamma = 0$. The reason for asymmetry is attributed to small geometric imperfections near the apex of the otherwise symmetric forebody[2]. Therefore, it is not surprising that the DVM will not predict asymmetric flow. This is not a limitation of the current modeling approach, more sophisticated methods will predict symmetric flow unless some asymmetry is introduced into the problem, *e.g.* Degani [21].

Figures 4.8 and 4.9 show the vortex positions and cross-sectional pressure distribution for $\phi = 10$ degrees and $\gamma = 0$, and for $\phi = 0$ and $\gamma = 10$ degrees respectively.

[2] See Section 3.2.1.

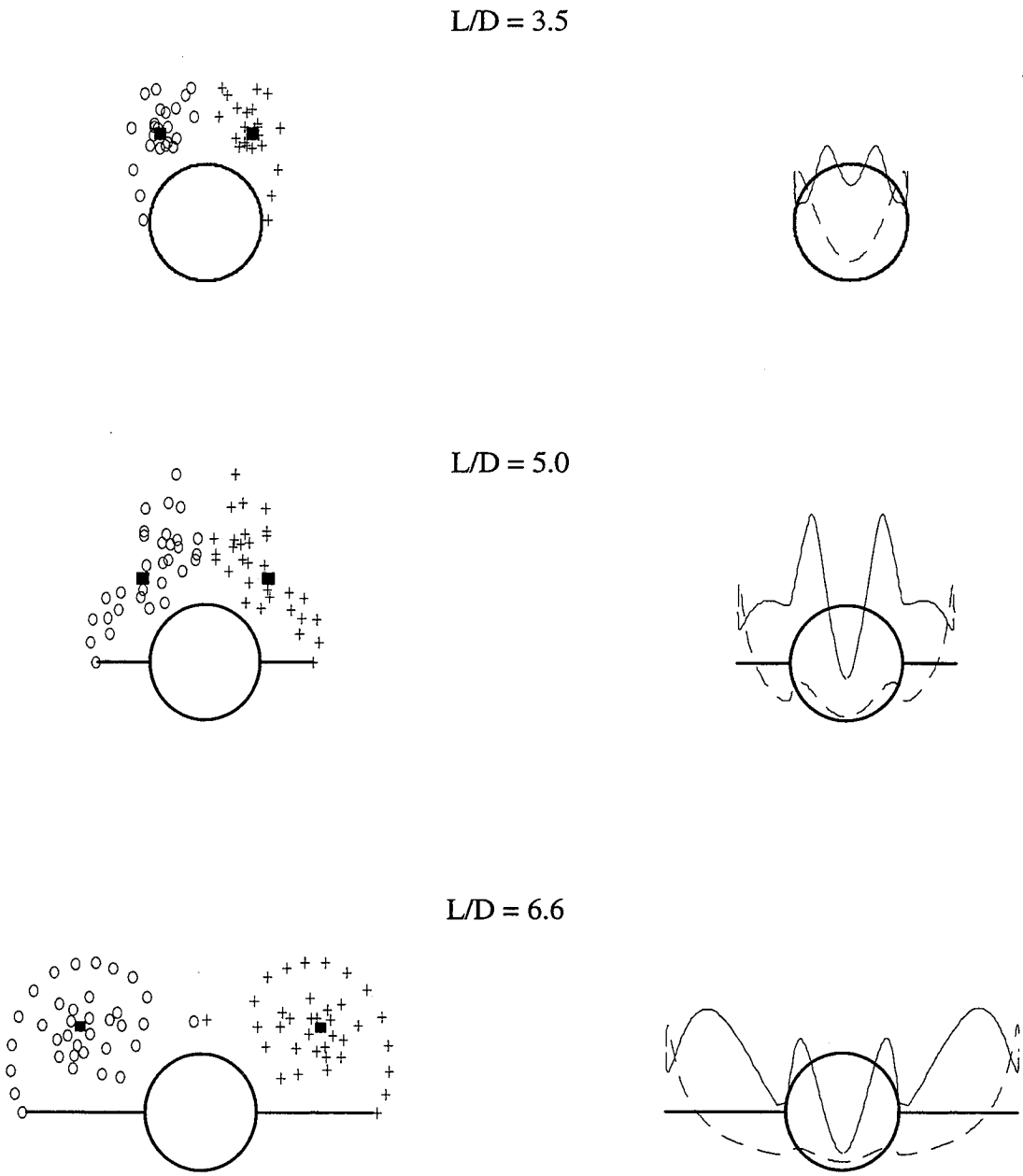

Figure 4.7: Positions of discrete vortices and C_p distribution for various cross-sections. $\phi = \gamma = 0$. $U_\infty = 19.5$ m/sec and $\alpha_0 = 45$ degrees.

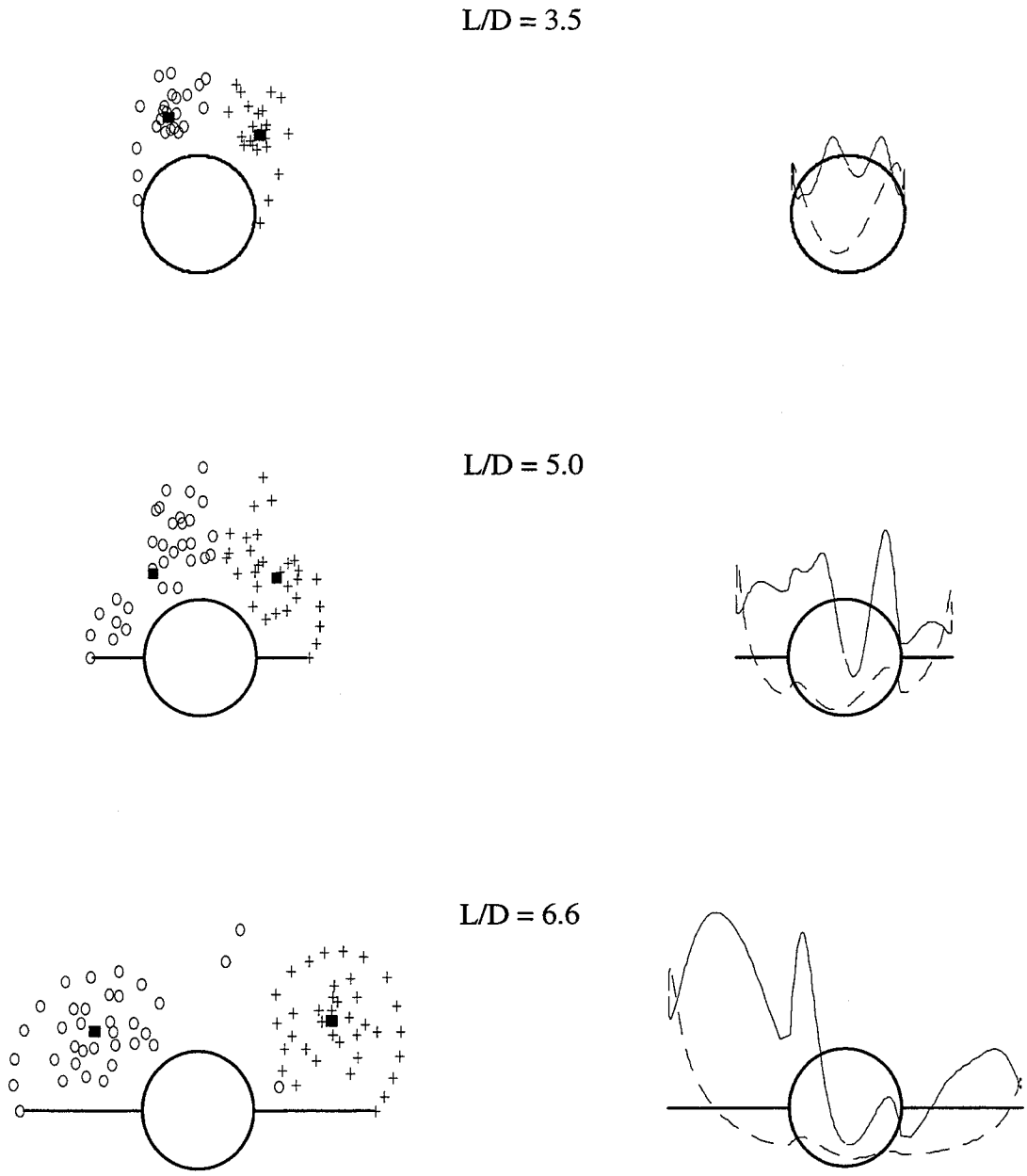

Figure 4.8: Positions of discrete vortices and C_p distribution for various cross-sections. ϕ = 10 degrees, γ = 0. U_∞ = 19.5 m/sec and α_0 = 45 degrees.

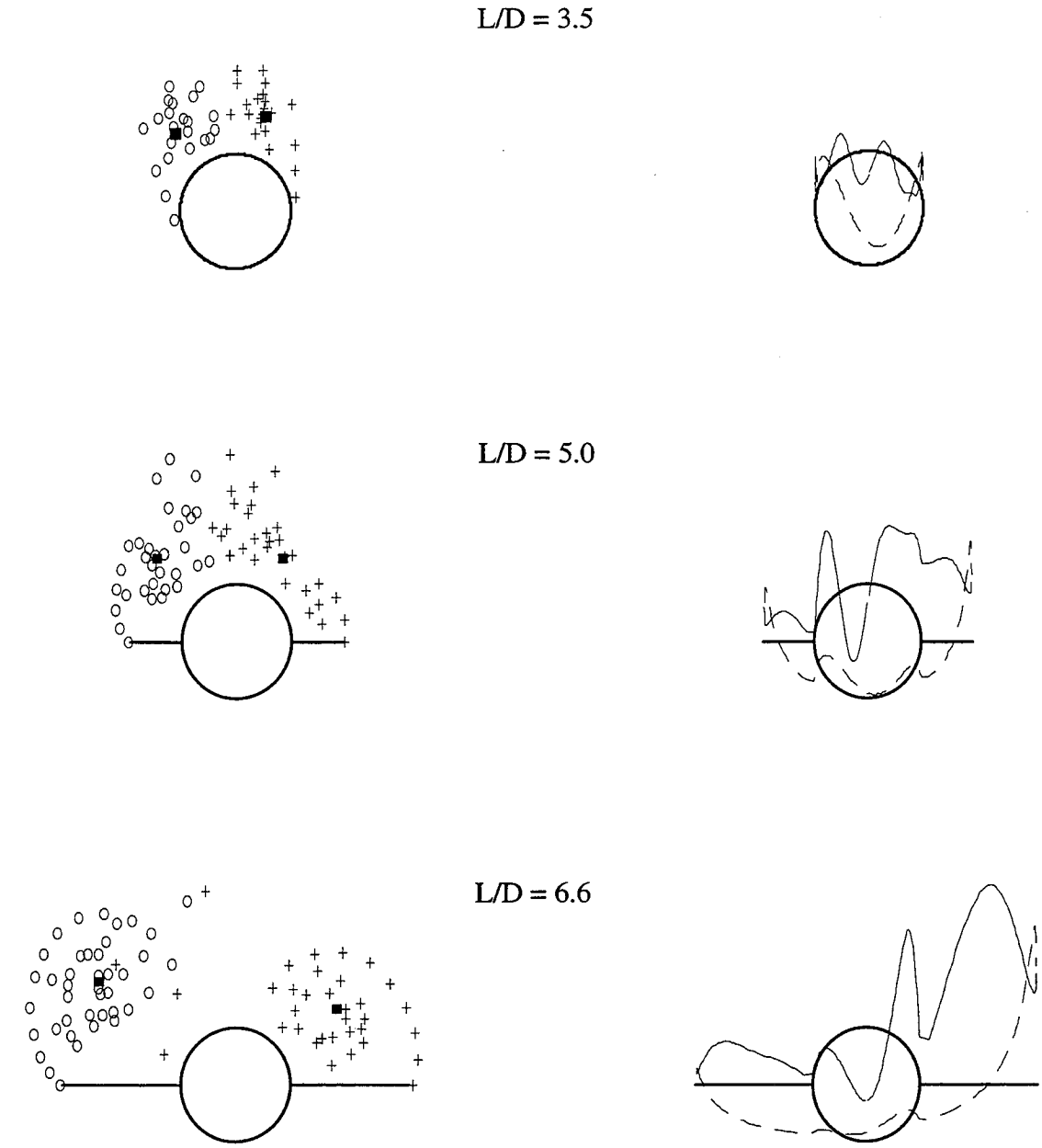

Figure 4.9: Positions of discrete vortices and C_p distribution for various cross-sections. $\phi = 0$, $\gamma = 10$ degrees. $U_\infty = 19.5$ m/sec and $\alpha_0 = 45$ degrees.

4.4.2 Aerodynamic Loads

It was shown in Chapter 3 that the use of a blunt forebody tip brings symmetry to the flow. It seems proper to use data for the model with a blunt tip to validate the DVM because it avoids the difficulties introduced by the pointed forebody tip. The roll and yaw moment coefficients calculated with the DVM are plotted in Figure 4.10 versus roll angle, for $\gamma = 0$. Experimental values measured for the model with the blunt tip are shown for comparison. The predicted values for the yaw moment agree reasonably well with experiments but large differences are observed for the roll moment. These are due to the fact that the DVM does not incorporate the effects of vortex diffusion and dissipation. Inclusion of these effects would decrease the roll moment but would have minor effects in the yaw moment because, as discussed in Chapter 3, roll moment is only generated at stations further downstream where the wings are present, and yaw moment is mainly generated at stations at the forebody.

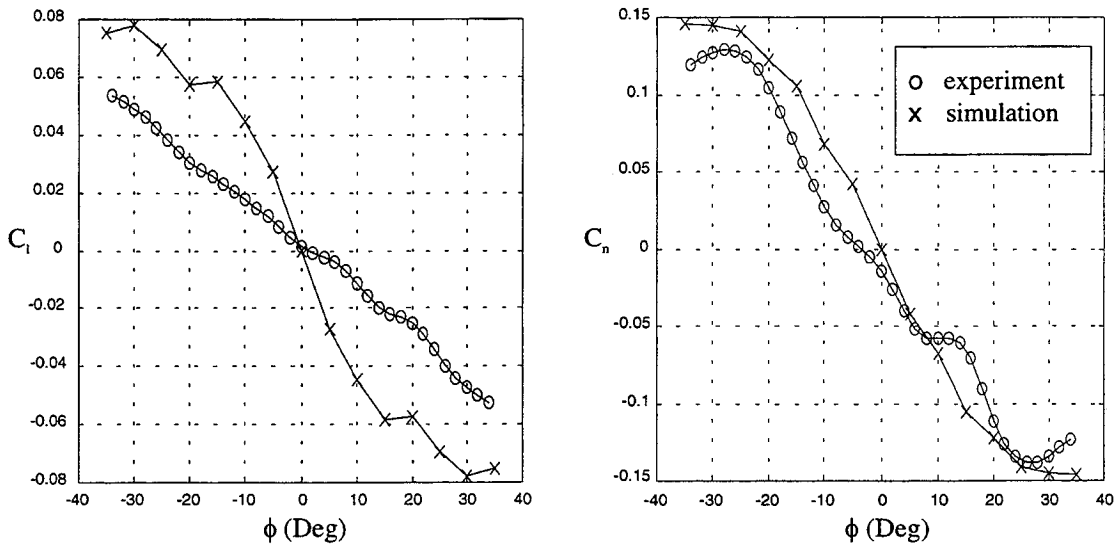

Figure 4.10: Roll and yaw moment coefficients, C_l and C_n respectively, versus roll angle. Comparison of DVM results and experimental data for the wind tunnel model with blunt forebody tip.

4.4.3 Forced Asymmetry

Experiments conducted using the wind tunnel model with the conical forebody tip, showed that the separation lines and the flow are asymmetric even for a condition where $\phi = \gamma = 0$ and $C_\mu = 0$. As demonstrated by the flow visualization results, the flow is characterized by three dominant vortical structures. To explore the capabilities of the discrete vortex method in capturing the interaction of forebody and wing vortices and producing results that are in agreement with the experimental observations, asymmetry was introduced into the flow. Figure 4.11 shows the results of the DVM for the model at $\phi = 20.5$ degrees and $\gamma = 0$ for the case where no blowing is applied. Both experimental and simulation results are shown for the flow structure at two stations along the length of the vehicle. In this case asymmetry was introduced by forcing asymmetric separation lines at a few stations along the forebody. By forcing the separation points at the first few stations of the forebody to be similar to the ones observed in the experiments, the flow will develop in a way that resembles the three vortical structures observed experimentally for stations further downstream. In the simulation results three clusters of vortices can be identified at positions similar to those observed in the flow visualization experiments. This indicates that although the discrete vortex method entails strong assumptions such as potential flow and does not account for phenomena such as vortex breakdown it retains the main physics of the flow and can be used to provide insight into the flow structure.

4.4.4 Forebody Tangential Blowing

As discussed in Chapter 3, the experimental observations showed that the most notable effect of forebody tangential blowing is to change the separation lines along the forebody of the vehicle. Associated with this are changes in the amount of vorticity that is shed into the flow. In this research, forebody tangential blowing is included in the discrete vortex method by forcing a change in the separation lines. The results of the previous section show that qualitatively the changes in flow structure can be captured by this simple approach. A quantitative approach would require the solution of the boundary layer

equations in the presence of a wall-jet, in a way similar to the approach taken by Mourtos [41], and is not pursued here.

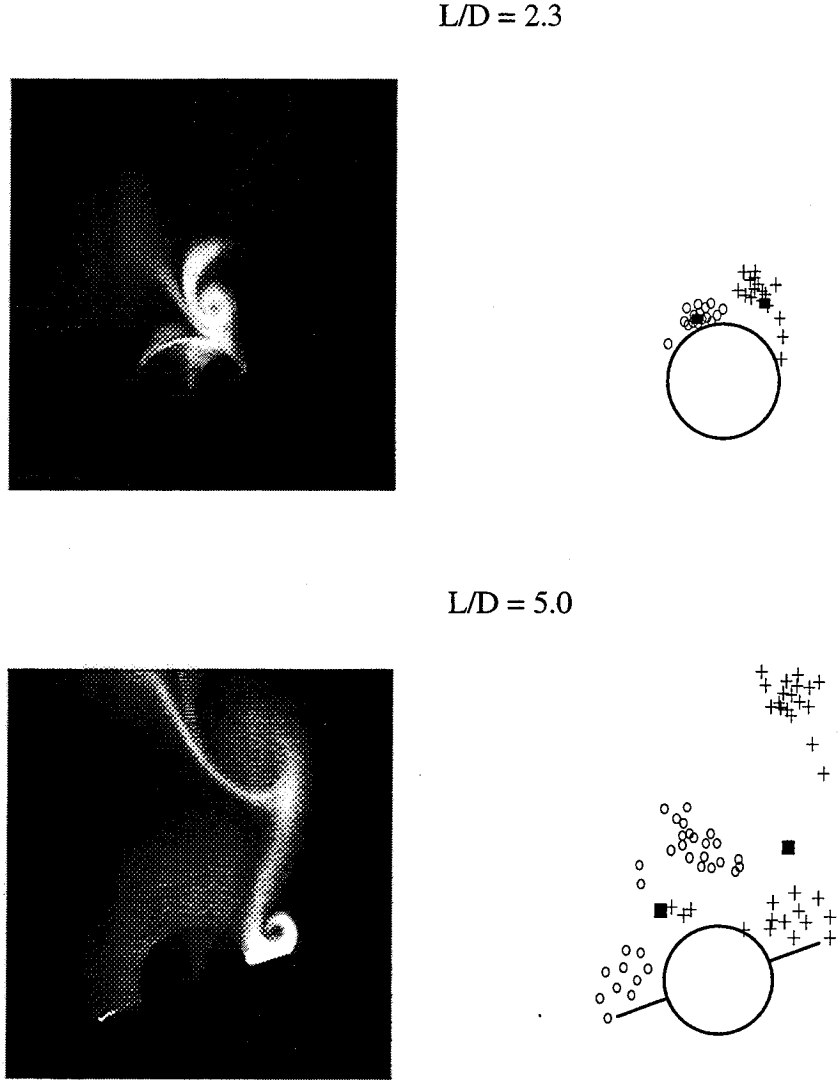

Figure 4.11: Flow structure obtained experimentally and through simulation by forcing asymmetric separation on part of the forebody. $\phi = 20.5$ degrees, $\gamma = 0$ and $C_\mu = 0$. Nominal incidence angle, α_0, is 45 degrees and $U_\infty = 19.5$ m/sec.

4.5 Conclusions

In this chapter the development of a steady-state aerodynamic model based on first principles has been presented. The form of the model resulted from an effort to obtain a simple formulation that entailed the main physics of the flow. Simplifying assumptions made in developing the model were justified by experimental results and observations. The discrete vortex model provides adequate results for the yaw moment when compared with experimental data for a wind tunnel model with a blunt forebody tip. Results for the roll moment agree only qualitatively and the simulation overestimates the slope of the roll moment versus roll angle curve by as much as a factor of two. This large error is attributed to the fact that the aerodynamic model does not account for the effects of vortex diffusion and dissipation. The discrete vortex model produces a flow structure that resembles the one observed experimentally, provided that the forebody separation lines are similar to the experimental ones. This shows that large scale interactions between forebody and wing vortices are properly represented.

In summary, the discrete vortex model allows the investigation of the effects of various parameters into the flow and agrees qualitatively with experimental results. On the other hand, the model is too simplified to generate reliable quantitative results and it does not include transient effects; both are necessary to study the dynamics of the system. To address these issues a different modeling approach, that trades fundamental understanding and derivation on first principles against accuracy and faster execution time, is presented in the next chapter

Chapter 5

Unsteady Aerodynamic Loads

This chapter focuses on the modeling of transient aerodynamic loads during vehicle maneuvers. A description of the transient loads is required for simulation of the system dynamic behavior and for control law design and implementation. A semi-empirical model is presented that includes the effects of vehicle motion and of blowing on the aerodynamic loads. A semi-empirical approach is taken because, as discussed in the previous chapter, the computation time intensive characteristic of state of the art numerical methods preclude their use for control law design and implementation. On the other hand, the developed semi-empirical model provides a compact representation of the unsteady effects which is suitable for controls. Static loads are an integral part of the unsteady aerodynamic model developed here, and can be obtained using the discrete vortex method of Chapter 4 or using data from experiments. A basic physical representation of the main dynamic effects is used to augment the steady state aerodynamics and calculate the non-steady loads. Parameters of the model are identified from experimental data and the model is validated using independent data sets. Roll-yaw motion of the wind tunnel model predicted from simulations are in agreement with experiments.

The semi-empirical aerodynamic model is presented first. The form of the model and its various components are discussed and justified based on experimental observations and

the basic physics of the flow. The aerodynamic model is then merged with the equations of motion of the two degrees-of-freedom system. The resulting equations are used together with measured dynamic data to identify the parameters of the semi-empirical model. The chapter concludes with the validation of the aerodynamic model.

5.1 Unsteady Aerodynamic Model

The form of the unsteady aerodynamic model was determined by considering dynamic effects that were observed experimentally and that can be justified based on the fundamental physics of the flow. Figure 5.1 shows the structure of the model in block diagram form. In the figure 's' is the Laplace transform variable. Inputs to the model are the attitude of the vehicle, ϕ and γ, and the amount of blowing, C_μ. The outputs are the unsteady aerodynamic moments about ϕ and γ, M_ϕ^A and M_γ^A respectively.

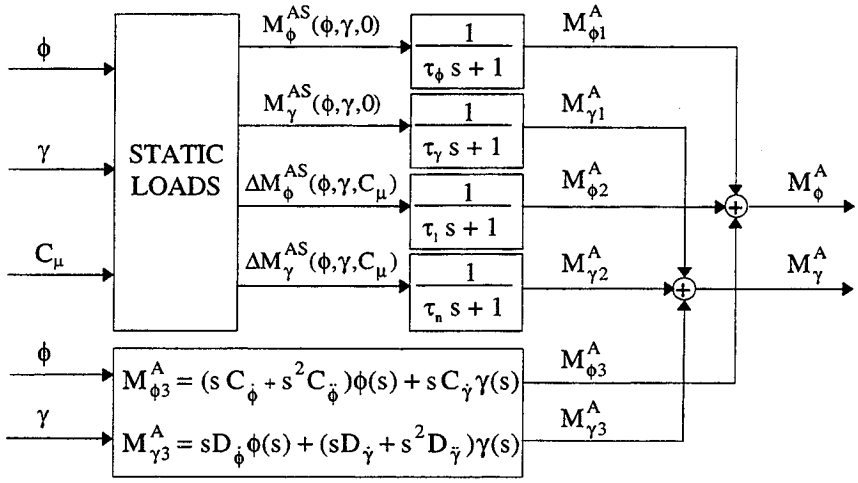

Figure 5.1: Structure of the unsteady aerodynamic model.

The unsteady aerodynamic moments are given by

$$M_\phi^A = M_{\phi 1}^A + M_{\phi 2}^A + M_{\phi 3}^A$$
$$M_\gamma^A = M_{\gamma 1}^A + M_{\gamma 2}^A + M_{\gamma 3}^A \qquad (5.1)$$

$M^A_{\phi 1}$ and $M^A_{\gamma 1}$ represent the lagged static moments for zero blowing. The effects of blowing are included through terms $M^A_{\phi 2}$ and $M^A_{\gamma 2}$. $M^A_{\phi 3}$ and $M^A_{\gamma 3}$ account for the effects of aerodynamic damping, rate cross-coupling and apparent mass of the fluid. A discussion of each of these terms is presented next.

$M^A_{\phi 1}$ and $M^A_{\gamma 1}$: During the motion of the vehicle, the vortex dynamic positions lag with respect to their static positions. This has been observed experimentally for the current model [16] and for delta wings [42] undergoing roll oscillations. Results from studies that model the flow over delta wings also support the existence of a vortex lag. For example, Arena and Nelson [43] developed an unsteady potential model for a delta wing that indicates the lag in the vortex position during wing-rock. Wong [9] successfully used a lag in the static roll moment to account for unsteady effects during roll oscillations of a delta wing at high angle of attack.

The idea of lagging the static roll moment is extended to the roll-yaw motion of the wing-body vehicle used in this research. It is assumed that the static roll and yaw moments are each subject to a lag during the motion of the wind tunnel model in two degrees-of-freedom. It is known that the strength of the vortices is also affected by the motion of the vehicle. The current approach lumps position and strength effects by lagging the static loads to represent their combined effect. In the time domain, the lagged static moments, shown in Figure 5.1 as $M^A_{\phi 1}$ and $M^A_{\gamma 1}$, are given by

$$\tau_\phi \dot{M}^A_{\phi 1} + M^A_{\phi 1} = M^{AS}_\phi(\phi, \gamma, C_\mu{=}0)$$
$$\tau_\gamma \dot{M}^A_{\gamma 1} + M^A_{\gamma 1} = M^{AS}_\gamma(\phi, \gamma, C_\mu{=}0) \qquad (5.2)$$

The lag represented by time constants τ_ϕ and τ_γ is associated with the motion of the vehicle and occurs even when no blowing is applied.

$M^A_{\phi 2}$ and $M^A_{\gamma 2}$: These terms account for the effect of forebody tangential blowing. As shown in Chapter 3, the transient response of the roll and yaw moment lag the blowing input. The physical explanation for this characteristic is that blowing modifies the flow

near the apex of the forebody, and convection is required for the changes to affect sections of the vehicle which are further downstream. These effects were discussed in detail in Section 3.5.

The time histories for the roll and yaw moment responses to blowing indicate that, the observed lag can be represented by first order models characterized by time constants τ_l and τ_n. Note that, in contrast to the time constants due to the vortex lag, these are not caused by the motion of the vehicle. In fact, the experiments used to determine τ_l and τ_n were conducted with the wind tunnel model fixed at a given roll and yaw angles[1]. In the time domain the moments, $M^A_{\phi 2}$ and $M^A_{\gamma 2}$, obtained with the first order models are

$$\begin{aligned} \tau_l \dot{M}^A_{\phi 2} + M^A_{\phi 2} &= \Delta M^{AS}_{\phi}(\phi, \gamma, C_\mu) \\ \tau_n \dot{M}^A_{\gamma 2} + M^A_{\gamma 2} &= \Delta M^{AS}_{\gamma}(\phi, \gamma, C_\mu) \end{aligned} \tag{5.3}$$

Where the terms on the right side of the equations represent the static moment due to blowing, *i.e.*

$$\Delta M^{AS}(\phi, \gamma, C_\mu) = M^{AS}(\phi, \gamma, C_\mu) - M^{AS}(\phi, \gamma, C_\mu = 0) \tag{5.4}$$

$M^A_{\phi 3}$ and $M^A_{\gamma 3}$: Unsteady effects are included to account for aerodynamic damping, roll-yaw rate cross-coupling and the apparent mass of the fluid. It is assumed that the aerodynamic damping and the rate cross-coupling are linear in $\dot{\phi}$ and $\dot{\gamma}$. The apparent mass effect reflects the added inertia of the fluid and is assumed proportional to the angular accelerations in ϕ and γ. The resulting expressions for $M^A_{\phi 3}$ and $M^A_{\gamma 3}$ in the time domain are

$$\begin{aligned} M^A_{\phi 3} &= C_{\dot{\phi}} \dot{\phi} + C_{\dot{\gamma}} \dot{\gamma} + C_{\ddot{\phi}} \ddot{\phi} \\ M^A_{\gamma 3} &= D_{\dot{\phi}} \dot{\phi} + D_{\dot{\gamma}} \dot{\gamma} + D_{\ddot{\gamma}} \ddot{\gamma} \end{aligned} \tag{5.5}$$

[1] See Section 3.5.

The coefficients in Equations 5.5 are called dynamic stability derivatives. The unsteady aerodynamic moments about ϕ and γ are given by Equations 5.1 through 5.5. If the static moments, M_{ϕ}^{AS} and M_{γ}^{AS}, the time constants, and the dynamic stability derivatives are known, the unsteady aerodynamic loads, M_{ϕ}^{A} and M_{γ}^{A}, can be calculated from measured time histories of ϕ, γ and C_{μ}.

As indicated in Figure 5.1 and Equations 5.2 and 5.3, the static loads are an integral part of the unsteady model. Different methods can be used, within the framework of the unsteady aerodynamic model, to provide the static loads. They can be obtained from a look-up table, from the discrete vortex method described in Chapter 4, or using more sophisticated theoretical methods. Which method to use depends on the availability of experimental data and the required accuracy and computational time. The design of control logic and its real-time implementation requires fast and accurate computation of the roll and yaw moments. To meet these requirements properly, the static loads were obtained from a look-up table containing experimental data.

5.2 Equations of Motion

The equations of motion for the two degrees-of-freedom system were derived in Chapter 2 and are repeated here as they are used in the determination of the various parameters of the unsteady aerodynamic model.

$$I_{M_x}\ddot{\phi} + (I_{M_z} - I_{M_y})\sin\phi\cos\phi\,\dot{\gamma}^2 + I_{M_{xz}}\cos\phi\,\ddot{\gamma} = M_{\phi}^{A} - C_F\dot{\phi}$$

$$(I_A + I_{M_y}\sin^2\phi + I_{M_z}\cos^2\phi)\,\ddot{\gamma} + (I_{M_y} - I_{M_z})2\sin\phi\cos\phi\,\dot{\phi}\,\dot{\gamma}$$

$$+I_{M_{xz}}(\ddot{\phi}\cos\phi - \dot{\phi}^2\sin\phi) = M_{\gamma}^{A} - D_F\dot{\gamma} - K_T\gamma - K_G\sin\gamma + M_{\gamma}^{M} \qquad (5.6)$$

In these equations, the unsteady aerodynamic moments M_{ϕ}^{A} and M_{γ}^{A} are given by Equations 5.1 through 5.5. M_{γ}^{M} is the torque applied by the active cancellation system and is given by Equation 2.11. The inertia components of the model and of the support

system, as well as other parameters of the experimental apparatus were measured independently and are given in Appendix B. In Equations 5.6, the only unknowns are the parameters that characterize the unsteady aerodynamic moments M_{ϕ}^{A} and M_{γ}^{A}. The procedure used to identify these parameters is described on the following section and makes use of the equations of motion (Equations 5.1 through 5.6) and measured time histories for ϕ and γ.

5.3 Parameter Identification

In order for the unsteady aerodynamic model to be used, it is necessary to determine the numerical values of the following parameters:

$$\tau_l, \tau_n, \tau_\phi, \tau_\gamma, C_{\dot{\phi}}, C_{\dot{\gamma}}, C_{\ddot{\phi}}, D_{\dot{\phi}}, D_{\dot{\gamma}}, D_{\ddot{\gamma}} \tag{5.7}$$

Time constants τ_l and τ_n, that characterize the roll and yaw moment transient responses to blowing, were determined by fitting the data from the experiment described in Section 5 of Chapter 3 to Equations 5.3. In the experiment the model was fixed at zero roll and yaw angles and a step input blowing was applied. Data were recorded for the roll and yaw moment responses as well as the blowing intensity, C_μ. It should be noted that, in these experiments miniature presure sensors located inside each plenum were used to measure C_μ. This was required to isolate the aerodynamic effects from the dynamics of the air supply system. A non-linear least squares algorithm, described in Appendix C, was used to identify the time constants τ_l and τ_n. Their values are given in Table 5.1.

Parameter	Converged value $\pm \sigma$	Units
τ_l	0.018 ± 0.001	sec
τ_n	0.005 ± 0.001	sec

Table 5.1: Time constants characterizing the transient response to blowing.

The results of the first order models, as well as the measured time histories for roll and yaw moment responses are presented in Figure 5.2. It is seen that the models adequately represent the response of roll and yaw moments to blowing.

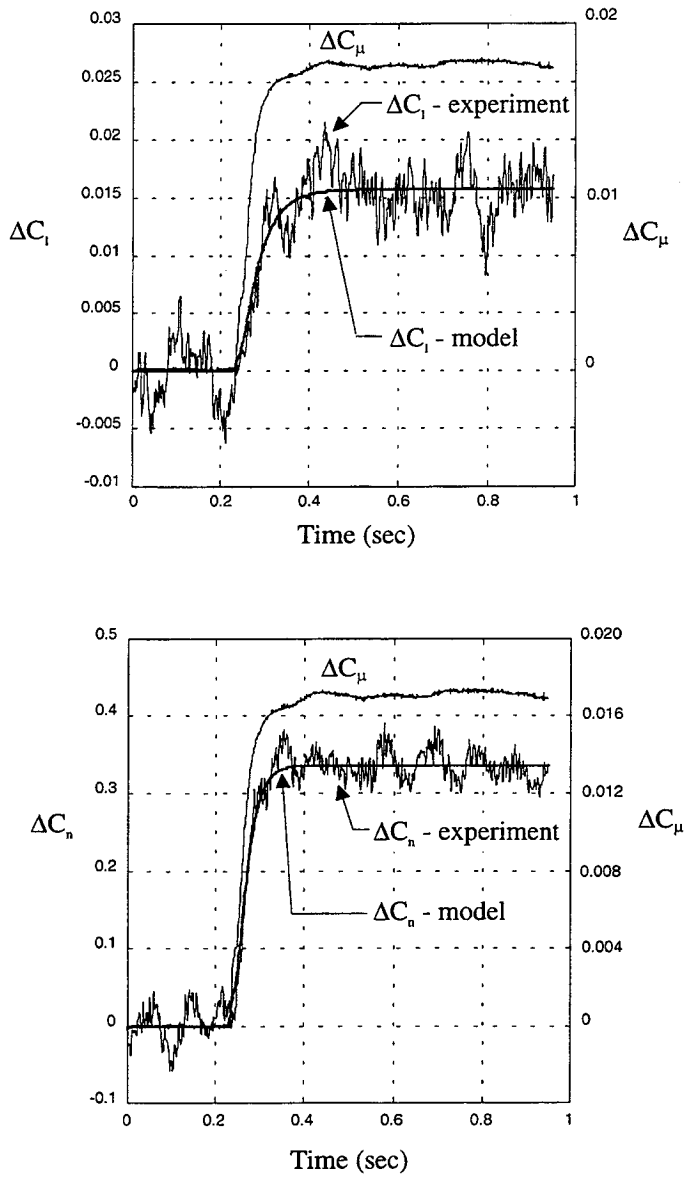

Figure 5.2: Roll and yaw moment transient responses to blowing. Comparison between first order model and experiment. $\phi = \gamma = 0$. $\alpha_0 = 45$ degrees and $U_\infty = 19.5$ m/sec.

Figure 5.3 illustrates the procedure used in identifying the remaining eight parameters of the unsteady aerodynamic model. In this case, a dynamic experiment was conducted, and data for the natural motion of the two degrees-of-freedom system recorded. A non-linear least squares algorithm was used to identify the missing parameters. The equations of motion coupled with the expressions for the unsteady aerodynamic model were used to simulate the dynamic response of the system. The parameters were varied in order to minimize the difference between the time histories obtained from simulation $\phi_s(t)$ and $\gamma_s(t)$ and the measured time histories $\phi_m(t)$ and $\gamma_m(t)$ obtained during dynamic experiments in the wind tunnel. The torque applied by the motor to the γ-axle to cancel external effects, M_γ^M, was measured during the experiments and was used as input during the simulations. In this way the errors due to the imperfect cancellation did not affect the identification of the parameters. The non-linear least squares algorithm is described in Appendix C.

Two distinct time histories, obtained from two independent experiments, were used simultaneously in the identification of the parameters of the unsteady aerodynamic model. The identified values are presented in Table 5.2 along with the corresponding standard deviation.

Parameter	Converged value $\pm \sigma$	Units
τ_ϕ	0.035 ± 0.006	sec
τ_γ	0.023 ± 0.007	sec
$C_{\dot{\phi}}$	$(-0.44 \pm 0.34) \times 10^{-3}$	Nm.sec
$C_{\dot{\gamma}}$	$(-1.02 \pm 0.02) \times 10^{-3}$	Nm.sec
$C_{\ddot{\phi}}$	$(0.4 \pm 0.1) \times 10^{-4}$	Nm.sec^2
$D_{\dot{\phi}}$	$(1.03 \pm 0.70) \times 10^{-3}$	Nm.sec
$D_{\dot{\gamma}}$	$(-2.5 \pm 0.7) \times 10^{-3}$	Nm.sec
$D_{\ddot{\gamma}}$	$(-1.18 \pm 1.0) \times 10^{-3}$	Nm.sec^2

Table 5.2: Identified values for parameters describing the unsteady aerodynamic effects.

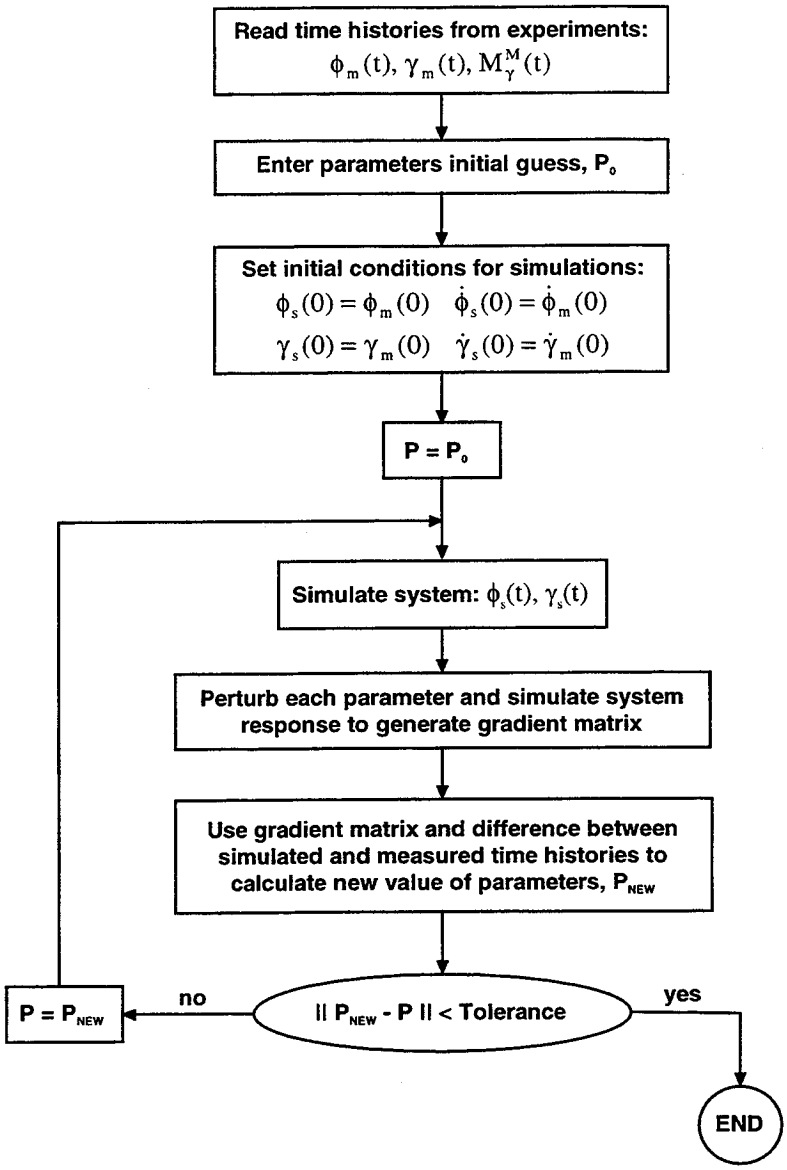

Figure 5.3: General procedure used for identification of the parameters describing the unsteady aerodynamic effects.

The simulation results and the measured time histories for the two experiments used in the parameter identification are shown in Figure 5.4. In performing the simulations the static aerodynamic loads have been obtained from a look-up table containing experimental data. Measured data for the static loads was used because it is more accurate

than the values obtained using the discrete vortex method of Chapter 4. This is specially important because the use of the conical forebody tip has a difficult to model effect on the aerodynamics[2].

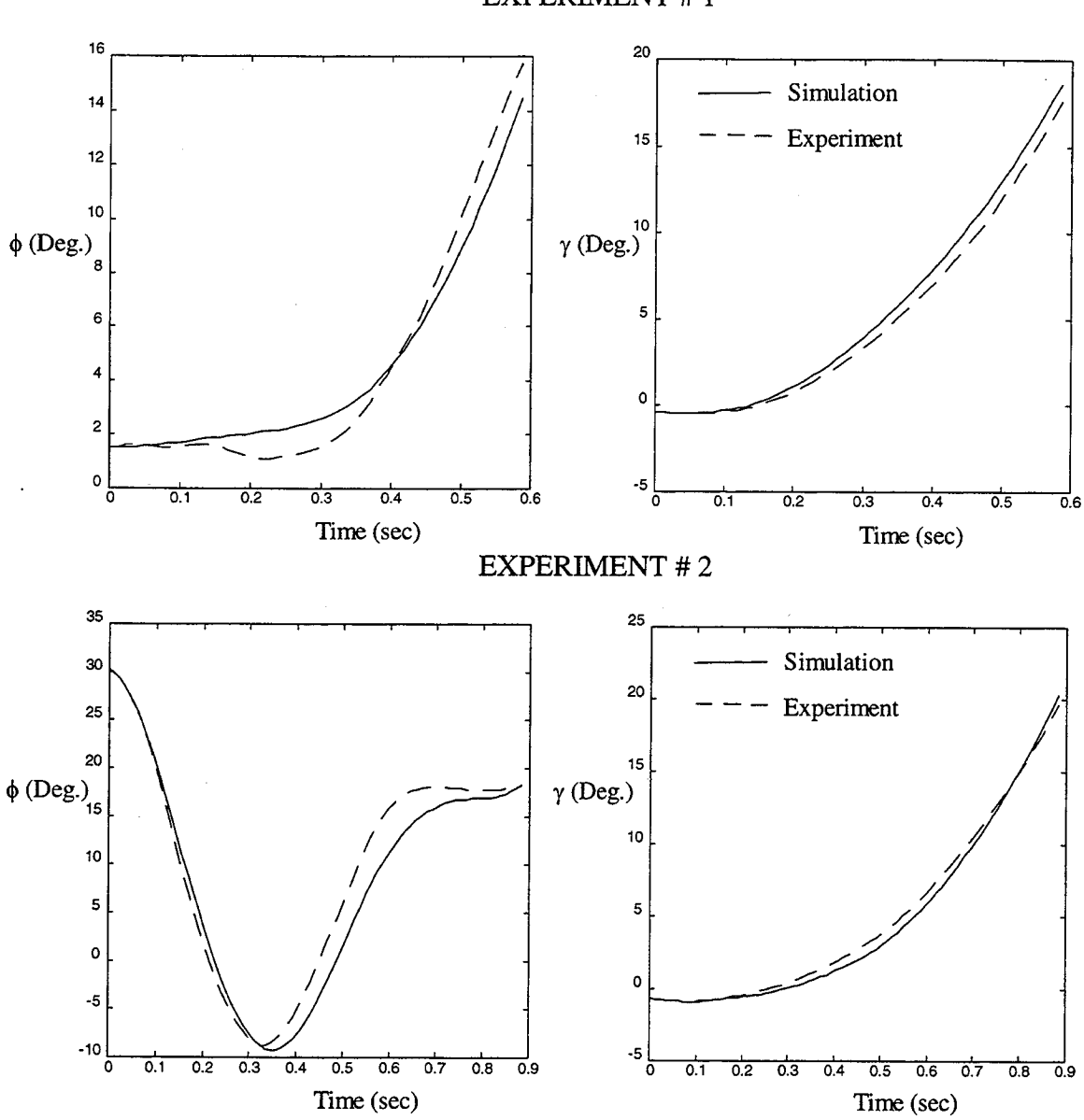

Figure 5.4: Results from parameter identification.

[2] See Section 3.2.1.

5.4 Model Validation

In order to validate the unsteady aerodynamic model several independent experiments were conducted. Measured data from these experiments were compared with results from simulations using the parameter values of Table 5.2. The results for two of those experiments and the corresponding simulations are shown in Figure 5.5.

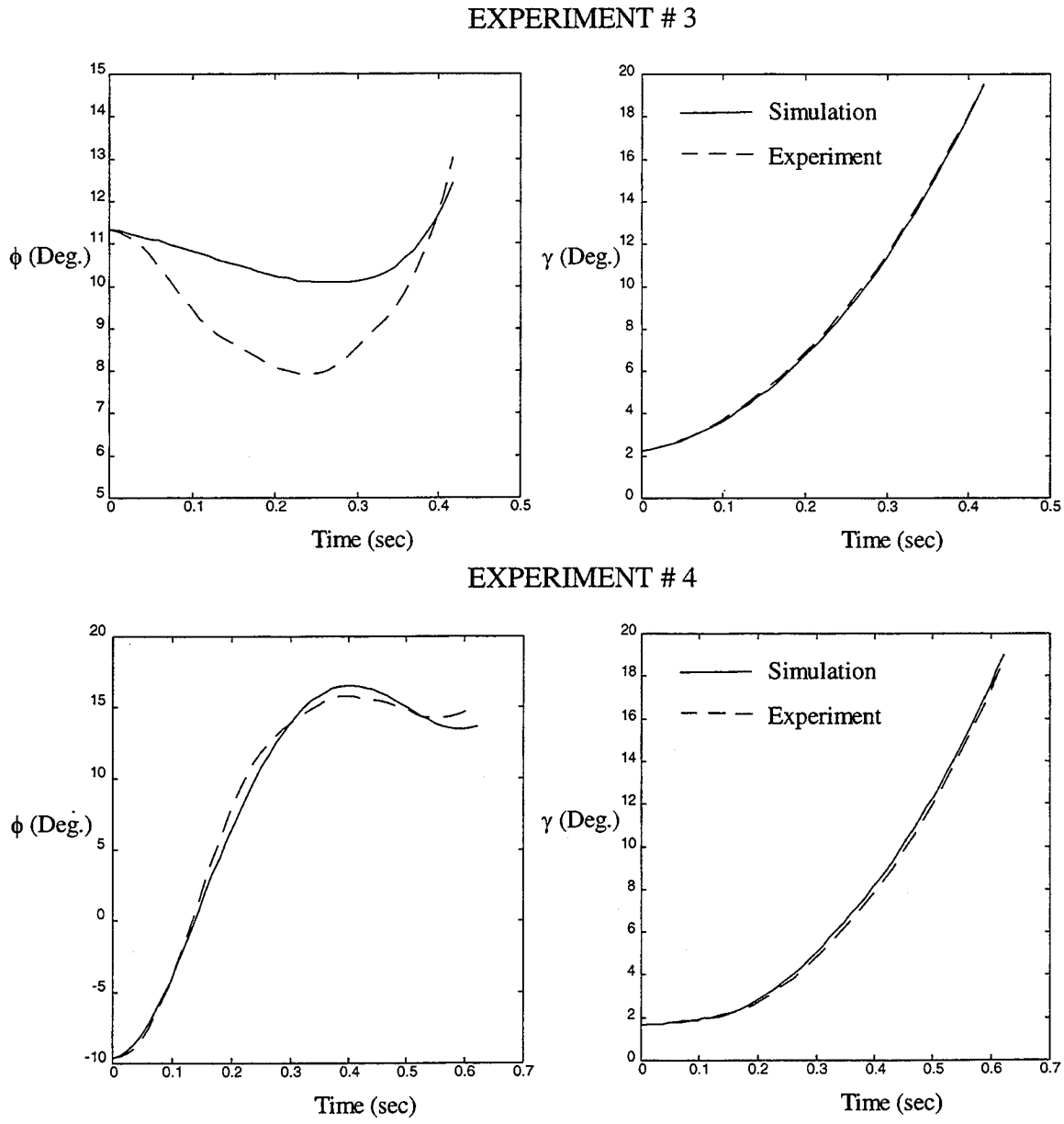

Figure 5.5: Validation of the unsteady aerodynamic model.

The simulation results are in reasonable agreement with the measured time histories. This indicates that the aerodynamic model provides a proper representation of the unsteady loads.

5.5 Summary

The development of a semi-empirical model for the unsteady aerodynamic loads has been presented in this chapter. A semi-empirical approach was taken in order to develop a model that could be used in the design and real-time implementation of control laws, which require fast and accurate calculation of the aerodynamic loads. The model developed here uses static aerodynamic loads that can be obtained through different methods, such as measurements or the discrete vortex method developed in Chapter 4. Non-linearities are introduced in the unsteady aerodynamic model by the static aerodynamic loads. Dynamic effects are included in the form of time constants and dynamic stability derivatives which are assumed linear in $\dot{\phi}$, $\dot{\gamma}$, $\ddot{\phi}$ and $\ddot{\gamma}$. The relatively small number of parameters used to represent the unsteady effects and the simple form of the model provide for fast calculation of the aerodynamic loads. Parameters of the model were identified using experimental data and a non-linear least squares algorithm.

Simulation results obtained using the unsteady aerodynamic model and the equations of motion of the system are in agreement with measured time histories for roll and yaw angles. As a result, a complete description of the two degrees-of-freedom system is obtained, and the feasibility of using forebody tangential blowing as a control device can be investigated. This problem is addressed in the next chapter.

Chapter 6

Control

As discussed in previous chapters, at high angles of attack the need exists for augmented control due to the reduced effectiveness of conventional control surfaces and the onset of lateral loads that can cause departure from controlled flight. This requirement for control was clearly demonstrated in Chapter 3, where the natural motion of the wind tunnel model was shown to be unstable.

The approach developed to control the wind tunnel model in roll and yaw using forebody tangential blowing as the only actuator is described in this chapter. The objective is to demonstrate the feasibility of using forebody tangential blowing to control the motion of the wind-tunnel model in two degrees-of-freedom. The unsteady aerodynamic model developed in Chapter 5 was used to complete the equations of motion of the two degrees-of-freedom system. A control strategy was devised that allows for linearization of the equations of motion. In this context, a linear quadratic regulator, LQR, design was used to generate a closed-loop control logic. It was demonstrated experimentally that forebody tangential blowing can be used to control the naturally unstable system. A linearized version of the unsteady aerodynamic model was used during the real-time control experiments to provide an estimate of the states required by the LQR controller. Results from simulation are in reasonable agreement with measured closed-loop response of the system.

6.1 Review of Objectives and Issues

One of the objectives of this research was to demonstrate the feasibility of using forebody tangential blowing, FTB, to control the roll-yaw motion of an aircraft. To achieve this objective, it is necessary to develop a control approach which uses FTB as the actuator. This is illustrated in Figure 6.1 as the problem of determining the proper logic to be used in the control box.

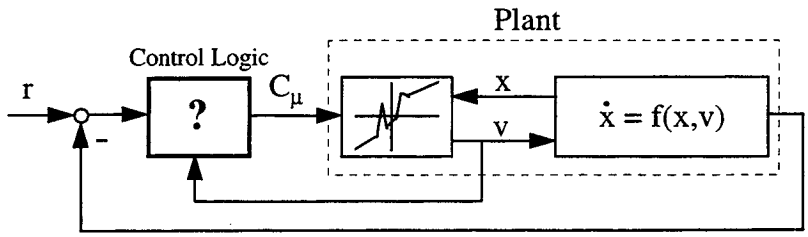

Figure 6.1: Statement of control problem.

One of the main difficulties in designing such a control logic is to provide a proper description of the aerodynamic loads. This problem has been addressed in Chapters 4 and 5. Once the equations of motion are known, the next step is to develop an approach that uses FTB to control the system. In general, this is a challenging problem because, as seen in Chapter 3:

1. The characteristics of the vehicle vary with blowing.
2. The blowing effects depend on the attitude of the vehicle.
3. Roll and yaw moment dependence on blowing are highly non-linear.

The development of a control approach which was successfully used to demonstrate the feasibility of using forebody tangential blowing to control the roll-yaw motion of the wind tunnel model is presented in the following sections.

6.2 Dynamics of the Air Supply System

A description of the system that uses the commanded value of blowing, $C_{\mu_{CMD}}$, as input is desired for the purposes of control. This description can be obtained by adding the dynamics of the air supply system, which consists of the valves, the flowmeters, the tubing, and the plena to the equations of motion given in Chapter 5. This added dynamics is illustrated in Figure 6.2 where C_μ is the jet momentum coefficient.

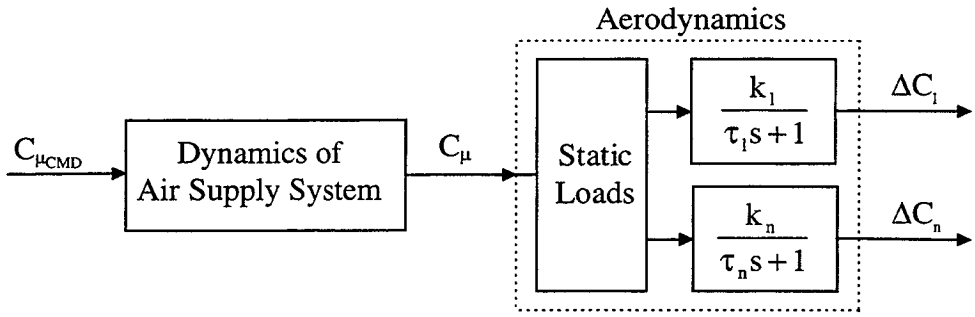

Figure 6.2: Dynamics of transient response to blowing command.

As shown in Chapter 5, the roll and yaw moment transient responses to blowing can be represented by first order lags with time constants τ_1 and τ_n respectively. Note that, in determining these time constants a measurement of pressure inside the plena were used to calculate the actual value of C_μ. This allowed relating τ_1 and τ_n with the physics of the flow because the dynamics of the air supply system were not included in the measurements[1].

It was verified that the overall dynamics from $C_{\mu_{CMD}}$ to the roll and yaw moments could be approximated by first order lags, characterized by time constants τ_{lc} and τ_{nc} respectively. This is illustrated in Figure 6.3.

[1] See Section 5.3 for a description of the experiment used to determine τ_1 and τ_n.

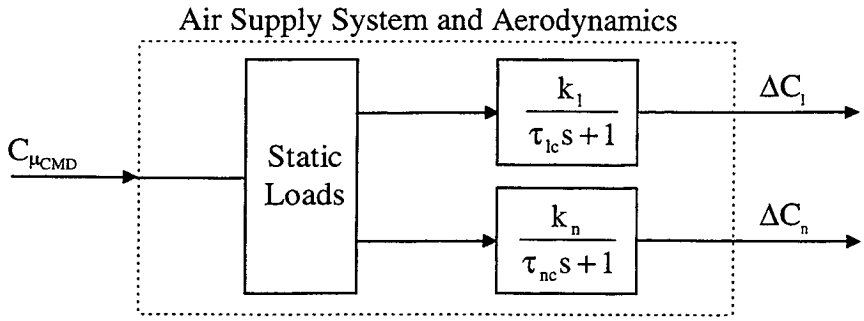

Figure 6.3: Assumed form for transient response to blowing command.

Similarly to the procedure used in Chapter 5, a non-linear least squares method was used to determine these new time constants from experimental data. The experiment that was conducted is similar to the one described in Section 3 of Chapter 5. The model was clamped at a given ϕ and γ and input was applied in terms of a commanded blowing coefficient, $C_{\mu_{CMD}}$. Data were recorded for the roll and yaw moments. The identified values for the new time constants are shown in Table 6.1.

Parameter	Converged value $\pm \sigma$	Units
τ_{lc}	0.040 ± 0.001	sec
τ_{nc}	0.023 ± 0.001	sec

Table 6.1: Time constants characterizing the transient response to blowing command.

τ_{lc} and τ_{nc} include both the effects of the air supply system dynamics and the unsteady aerodynamics. Their values are larger than their counterparts τ_l and τ_n which represent only the effect of the aerodynamics[1].

In Figure 6.4 the results of the first order models are compared with experimental data. Curves are shown for the commanded value of the blowing coefficient, $C_{\mu_{CMD}}$, the measured values of C_l and C_n and the results of the first order models for the roll and yaw

[1] See Table 5.1.

moment coefficients. It is seen that, except for the higher frequency components, which are attributed to the unsteadiness of the flow and compliance of the force-torque sensor, the form assumed for the model provides a good representation of the transient response of roll and yaw moments to $C_{\mu_{CMD}}$.

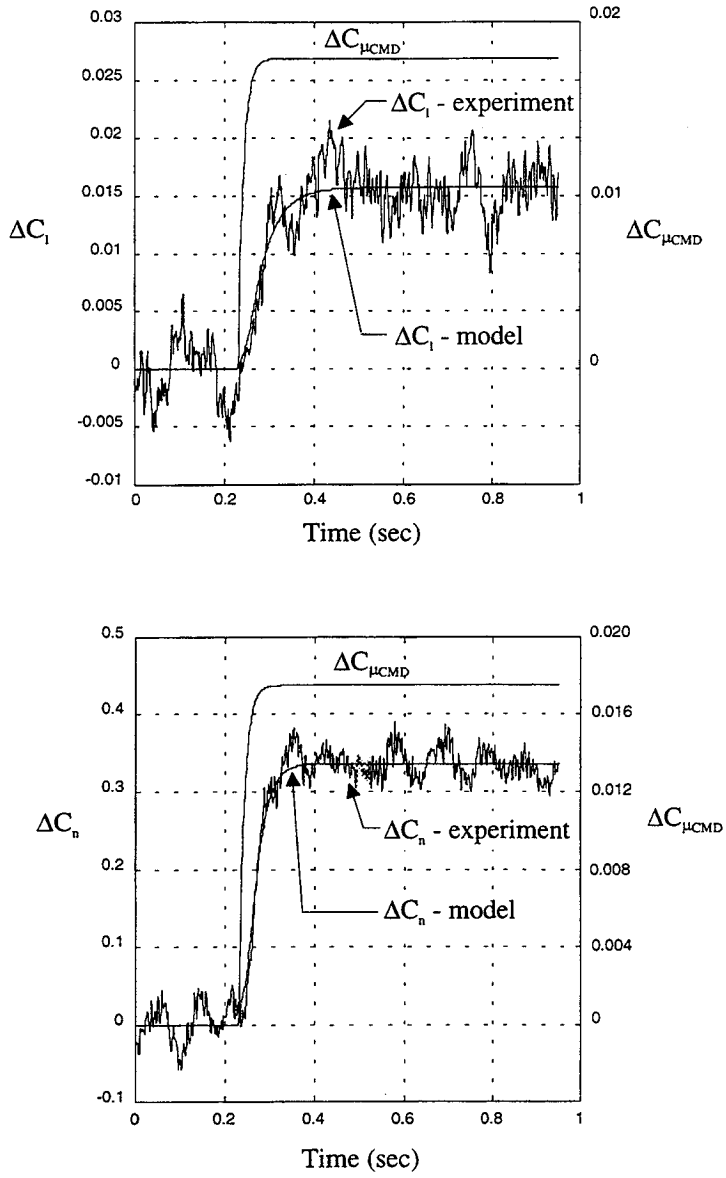

Figure 6.4: Transient responses of roll and yaw moments to blowing command.

6.3 The Two Degrees-of-Freedom System

A complete description of the two degrees-of-freedom system is given by the equations of motion derived in Chapter 2, the unsteady aerodynamic model developed in Chapter 5 and the dynamics of the air supply system as described in the previous section. Collecting the equations results

$$I_{M_x}\ddot{\phi} + (I_{M_z} - I_{M_y})\sin\phi\cos\phi\,\dot{\gamma}^2 + I_{M_{xz}}\cos\phi\,\ddot{\gamma} = M^A_{\phi 1} + M^A_{\phi 2} + (C_{\dot{\phi}} - C_F)\dot{\phi} + C_{\dot{\gamma}}\dot{\gamma} + C_{\ddot{\phi}}\ddot{\phi}$$

$$(I_A + I_{M_y}\sin^2\phi + I_{M_z}\cos^2\phi)\ddot{\gamma} + (I_{M_y} - I_{M_z})2\sin\phi\cos\phi\,\dot{\phi}\dot{\gamma} + I_{M_{xz}}(\ddot{\phi}\cos\phi - \dot{\phi}^2\sin\phi)$$
$$= M^A_{\gamma 1} + M^A_{\gamma 2} + D_{\dot{\phi}}\dot{\phi} + (D_{\dot{\gamma}} - D_F)\dot{\gamma} + D_{\ddot{\gamma}}\ddot{\gamma} - K_T\gamma - K_G\sin\gamma + M^M_\gamma$$

$$\tau_\phi \dot{M}^A_{\phi 1} + M^A_{\phi 1} = M^{AS}_\phi(\phi, \gamma, C_\mu{=}0)$$

$$\tau_\gamma \dot{M}^A_{\gamma 1} + M^A_{\gamma 1} = M^{AS}_\gamma(\phi, \gamma, C_\mu{=}0)$$

$$\tau_{lc} \dot{M}^A_{\phi 2} + M^A_{\phi 2} = \Delta M^{AS}_\phi(\phi, \gamma, C_{\mu CMD})$$

$$\tau_{nc} \dot{M}^A_{\gamma 2} + M^A_{\gamma 2} = \Delta M^{AS}_\gamma(\phi, \gamma, C_{\mu CMD})$$

$$M^M_\gamma = I_A\hat{\ddot{\gamma}} + K_T\hat{\gamma} + K_G\sin\hat{\gamma} \qquad (6.1)$$

The torque applied by the active cancellation system, M^M_γ, is calculated from the estimates of γ and its angular acceleration, $\hat{\gamma}$ and $\hat{\ddot{\gamma}}$ respectively, which in this case are equal to their measured values, *i.e.* $\hat{\gamma} \equiv \gamma_m$ and $\hat{\ddot{\gamma}} \equiv \ddot{\gamma}_m$. Note that, in contrast to Equations 5.3, τ_{lc}, τ_{nc} and $C_{\mu_{CMD}}$ are used in the expressions that account for the effect of blowing, $M^A_{\phi 2}$ and $M^A_{\gamma 2}$.

6.4 Control Approach

For control purposes the system comprised of the wind tunnel model and its active support mechanism is a multi-input, multi-output system. The inputs are the forebody tangential blowing which can be independently applied to the right and to the left side of the forebody. This is the only actuation available for control purposes in the experiments.

In this work, blowing was considered as a single actuator, *i.e.* for the purpose of control blowing was applied either to the right or to the left side of the model. Therefore, in the current work the system has only one input. The two degrees-of-freedom, ϕ and γ, are the sensed outputs of the system.

Equations 6.1, that describe the two degrees-of-freedom system, are nonlinear. The approach taken in this research has been to linearize those equations, and design a control logic for the linearized system. The conditions required for the linearization are discussed in the following paragraphs.

Linearization of the left hand side of the first and second equations of 6.1 poses no difficulty. On the other hand, linearization of the terms that represent the static aerodynamic loads, M_{ϕ}^{AS} , M_{γ}^{AS} , ΔM_{ϕ}^{AS} and ΔM_{γ}^{AS}, require assumptions regarding the flight envelope and the control strategy to be used.

About the static equilibrium position, defined by ϕ_E and γ_E, the static aerodynamic moments for zero blowing, M_{ϕ}^{AS} and M_{γ}^{AS}, can be written as

$$M_{\phi}^{AS} = C_{\phi}(\phi - \phi_E) + C_{\gamma}(\gamma - \gamma_E)$$

$$M_{\gamma}^{AS} = D_{\phi}(\phi - \phi_E) + D_{\gamma}(\gamma - \gamma_E) \qquad (6.2)$$

Where C_{ϕ} ,C_{γ} , D_{ϕ} and D_{γ} are the static stability derivatives obtained from the curves for the roll and yaw moments versus ϕ and γ, and are given in Table 6.2.

Parameter	Value	Units
C_{ϕ}	–0.025	Nm/rad
C_{γ}	0.022	Nm/rad
D_{ϕ}	–0.143	Nm/rad
D_{γ}	0.143	Nm/rad

Table 6.2: Values for the static stability derivatives.

It is convenient to rewrite the equations in terms of δ_ϕ and δ_γ defined as

$$\delta_\phi \equiv \phi - \phi_E$$
$$\delta_\gamma \equiv \gamma - \gamma_E \tag{6.3}$$

For $\delta_\phi << 1$ and $\delta_\gamma << 1$ it is possible to linearize the first four expressions in 6.1. The results are shown next for the current case where the product of inertia, $I_{M_{xz}}$, is zero, and ϕ_E and γ_E are small.

$$I_{M_x}\ddot{\delta}_\phi = M^A_{\phi 1} + M^A_{\phi 2} + (C_{\dot{\phi}} - C_F)\dot{\delta}_\phi + C_{\dot{\gamma}}\dot{\delta}_\gamma + C_{\ddot{\phi}}\ddot{\delta}_\phi$$
$$I_{M_z}\ddot{\delta}_\gamma = M^A_{\gamma 1} + M^A_{\gamma 2} + D_{\dot{\phi}}\dot{\delta}_\phi + (D_{\dot{\gamma}} - D_F)\dot{\delta}_\gamma + D_{\ddot{\gamma}}\ddot{\delta}_\gamma + M^{error}_\gamma$$
$$\tau_\phi \dot{M}^A_{\phi 1} + M^A_{\phi 1} = C_\phi \delta_\phi + C_\gamma \delta_\gamma$$
$$\tau_\gamma \dot{M}^A_{\gamma 1} + M^A_{\gamma 1} = D_\phi \delta_\phi + D_\gamma \delta_\gamma \tag{6.4}$$

M^{error}_γ is the error due to the active cancellation and is treated as a disturbance to the system[1].

$$M^{error}_\gamma \equiv M^M_\gamma - I_A\ddot{\gamma} - K_T\gamma - K_G \sin\gamma \tag{6.5}$$

To complete the linearization, it is necessary to investigate a proper method of including the effect of forebody tangential blowing, *i.e.* linearize the fifth and sixth expressions of Equations 6.1.

6.4.1 Linearization of Actuator Characteristics

As shown in Chapter 3, superimposing symmetric and asymmetric blowing produces almost linear responses of roll and yaw moments to blowing. If this blowing strategy is

[1] See Section 2.3.3.

used, the fifth and sixth expressions of Equations 6.1 are linear, and a complete linearized representation of the system is available that can be used in the design of a compensator. Although this represents one possible method to solve to the problem, this control strategy is not pursued here because of its potential larger use of air as compared to a strategy that uses only asymmetric blowing.

The dependency of roll and yaw moments on asymmetric blowing is highly non-linear. For small values of C_μ it is not possible to linearize the roll and yaw moment responses to blowing. The approach taken here consists of avoiding the small values of C_μ where the non-linearities are difficult to model. A minimum value of blowing, $C_{\mu_{MIN}}$, is chosen and the control strategy consists of applying this minimum value of blowing plus an amount, ΔC_μ, determined by the control logic to be designed. This control strategy is represented by

$$\left|C_{\mu_{CMD}}\right| = \left|C_{\mu_{MIN}}\right| + \left|\Delta C_\mu\right| \tag{6.6}$$

Blowing is applied either to the right or to the left side of the vehicle. Positive values of ΔC_μ indicate blowing on the starboard side and negative values on the port side. The sign convention is given in Table 6.3.

	Starboard Blowing - C_{μ_R}	Port Side Blowing - C_{μ_L}
$\Delta C_\mu > 0$	$C_{\mu_{MIN}} + \Delta C_\mu$	0
$\Delta C_\mu = 0$	0	0
$\Delta C_\mu < 0$	0	$C_{\mu_{MIN}} + \left\|\Delta C_\mu\right\|$

Table 6.3: Control strategy using asymmetric blowing.

The dependency of the roll and yaw moment coefficients with ΔC_μ is illustrated in Figure 6.5. It is seen that, the effect of using the control strategy of Equation 6.6 is to substitute

the difficult to model non-linearity by a known non-linearity. The resulting dependency of C_l and C_n on ΔC_μ is almost linear except for a discontinuity at the origin.

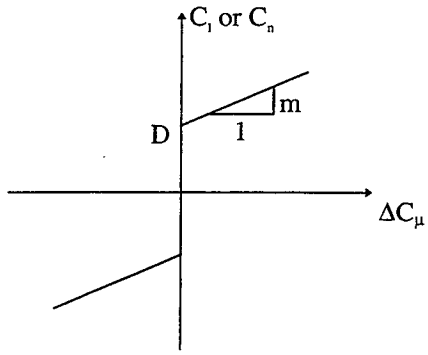

Figure 6.5: Approximate characteristic of roll and yaw moment coefficients as a function of ΔC_μ for the proposed blowing strategy.

For the purposes of demonstrating the feasibility of using blowing to control the system, the resulting non-linearity (Figure 6.5) was linearized. A describing function approach was used to determine equivalent gains for the curves C_l and C_n versus ΔC_μ. The actual gain, N(A), depends on the amplitude of the input, *i.e.* the amplitude of ΔC_μ , A, and is given by

$$N(A) = \frac{4D}{\pi A} + m \tag{6.7}$$

D and m are defined in Figure 6.5. An average amplitude was selected for ΔC_μ and used to calculate C_B and D_B the equivalent gains for the roll and yaw moments respectively. This approach yields the following linearized expressions for the static roll and yaw moments caused by blowing

$$\Delta M_\phi^{AS}(\phi, \gamma, C_{\mu_{CMD}}) = C_B \Delta C_\mu$$
$$\Delta M_\gamma^{AS}(\phi, \gamma, C_{\mu_{CMD}}) = D_B \Delta C_\mu \tag{6.8}$$

Where C_B and D_B are the linearized actuator gains and are given in Table 6.4 for the case where the minimum value of blowing, $C_{\mu_{MIN}}$, is equal to 0.01.

Parameter	Value	Units
C_B	0.28	Nm
D_B	5.05	Nm

Table 6.4: Linearized actuator gains for $C_{\mu_{MIN}} = 0.01$.

In the above equations, ΔM_ϕ^{AS} and ΔM_γ^{AS} are assumed independent of ϕ and γ. This is valid for a limited range of ϕ and γ and because the small values of blowing are avoided[1]. Substituting 6.8 into the fifth and sixth equations of 6.1 results in the following linearized equations for the effect of blowing.

$$\begin{aligned} \tau_{lc}\dot{M}_{\phi 2}^{A} + M_{\phi 2}^{A} &= C_B \Delta C_\mu \\ \tau_{nc}\dot{M}_{\gamma 2}^{A} + M_{\gamma 2}^{A} &= D_B \Delta C_\mu \end{aligned} \tag{6.9}$$

6.4.2 Compensator Design

Equations 6.4 and 6.9 provide a linearized representation of the system. They can be written in the form $\dot{\boldsymbol{x}} = \boldsymbol{Ax} + \boldsymbol{Bu}$, where the state vector and the input are defined as

$$\begin{aligned} \boldsymbol{x} &\equiv \left[\dot{\delta}_\phi \quad \dot{\delta}_\gamma \quad \delta_\phi \quad \delta_\gamma \quad M_{\phi 1}^{A} \quad M_{\gamma 1}^{A} \quad M_{\phi 2}^{A} \quad M_{\gamma 2}^{A}\right]^T \\ \boldsymbol{u} &\equiv \Delta C_\mu \end{aligned} \tag{6.10}$$

And the resulting $\boldsymbol{A}$ and $\boldsymbol{B}$ matrices are

[1] See Section 3.2.3.

$$\boldsymbol{A} = \begin{bmatrix} -7.0 & -4.64 & 0 & 0 & 4545.45 & 0 & 4545.45 & 0 \\ 0.24 & -2.51 & 0 & 0 & 0 & 228.31 & 0 & 228.31 \\ 1 & 0 & 0 & 0 & 0 & 0 & 0 & 0 \\ 0 & 1 & 0 & 0 & 0 & 0 & 0 & 0 \\ 0 & 0 & -0.71 & 0.63 & -28.57 & 0 & 0 & 0 \\ 0 & 0 & -6.22 & 6.21 & 0 & -43.48 & 0 & 0 \\ 0 & 0 & 0 & 0 & 0 & 0 & -25.00 & 0 \\ 0 & 0 & 0 & 0 & 0 & 0 & 0 & -43.48 \end{bmatrix} \tag{6.11}$$

$$\boldsymbol{B} = \begin{bmatrix} 0 & 0 & 0 & 0 & 0 & 0 & 7.0 & 220.0 \end{bmatrix}^{\mathrm{T}} \tag{6.12}$$

A linear quadratic regulator design was used to calculate the gain matrix $\boldsymbol{K}$ used to compute the control,

$$\boldsymbol{u} = -\boldsymbol{K}\boldsymbol{x} \tag{6.13}$$

that minimizes the quadratic cost function J,

$$J = \int_0^{\infty} \left(\boldsymbol{x}^T \boldsymbol{Q} \boldsymbol{x} + \boldsymbol{u}^T \boldsymbol{R} \boldsymbol{u} \right) \mathrm{dt} \tag{6.14}$$

subject to the dynamic equations $\dot{\boldsymbol{x}} = \boldsymbol{A}\boldsymbol{x} + \boldsymbol{B}\boldsymbol{u}$.

The weighting matrix $\boldsymbol{Q}$ was chosen to be diagonal, moreover only the degrees-of-freedom and their first-order derivatives were weighted, *i.e.*

$$\boldsymbol{Q} = Diagonal \left(Q_{\dot{\delta}_\phi} \quad Q_{\dot{\delta}_\gamma} \quad Q_{\delta_\phi} \quad Q_{\delta_\gamma} \quad 0 \quad 0 \quad 0 \quad 0 \right) \tag{6.15}$$

In the current case $\boldsymbol{R}$ is a scalar, it places a penalty in the control usage.

The resulting gain matrix is

$$\boldsymbol{K} = [0.00102 \quad 0.03198 \quad 0.00271 \quad 0.25156 \quad -0.29918 \quad 0.11332 \quad -0.29918 \quad 0.11332] \quad (6.16)$$

6.4.3 Implementation of Closed-Loop Control Logic

The designed closed-loop control logic as given by Equation 6.13 assumes that all the components of the state vector, $\boldsymbol{x}$, are known. Measurements, ϕ_m and γ_m , are available for the two degrees-of-freedom from which estimates $\hat{\delta}_\phi$ and $\hat{\delta}_\gamma$ are obtained for δ_ϕ and δ_γ respectively.

$$\hat{\delta}_\phi = \phi_m - \phi_e$$
$$\hat{\delta}_\gamma = \gamma_m - \gamma_e \quad (6.17)$$

Estimates for the angular rates are obtained from the measurements of ϕ and γ as follows,

$$\hat{\dot{\delta}}_\phi(s) = \frac{s}{\frac{s^2}{\omega_n^2} + 2\zeta\frac{s}{\omega_n} + 1}\phi_m(s)$$
$$\hat{\dot{\delta}}_\gamma(s) = \frac{s}{\frac{s^2}{\omega_n^2} + 2\zeta\frac{s}{\omega_n} + 1}\gamma_m(s) \quad (6.18)$$

Where ζ and ω_n are chosen to represent a Butterworth filter with cutoff frequency of 40 Hertz.

$M_{\phi 1}^A$ and $M_{\gamma 1}^A$ are estimated using $\hat{\delta}_\phi$ and $\hat{\delta}_\gamma$ in the last two expressions of Equations 6.4. The remaining elements of the state vector, $M_{\phi 2}^A$ and $M_{\gamma 2}^A$, are estimated from Equations 6.9.

Figure 6.6 shows in block diagram form the compensator as implemented in the real-time system. $\hat{x}$ is the estimated or reconstructed state vector obtained as described in the previous paragraphs. Also shown is the effective characteristic that results from using the described blowing strategy. In the figure, **v** represents the static roll and yaw moments due to blowing.

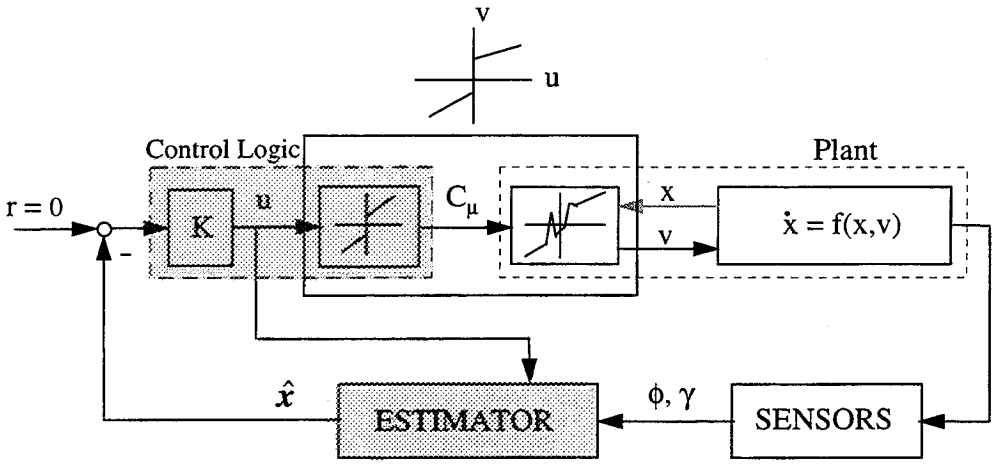

Figure 6.6: Real-time implementation of closed-loop control logic.

6.5 Results

The response of the closed-loop system to an initial condition is shown in Figure 6.7. In this case the control logic described in Section 6.4.1 was used with $C_{\mu_{MIN}} = 0.01$. Time histories for ϕ and γ are presented for the case where the system was released from $\phi \approx 37$ degrees and $\gamma \approx 14$ degrees. Both experimental data and simulation results are shown for comparison. It is seen that the control logic stabilizes the system. This result validates the developed control approach and demonstrates the feasibility of using forebody tangential blowing as an actuator in the high angle of attack regime.

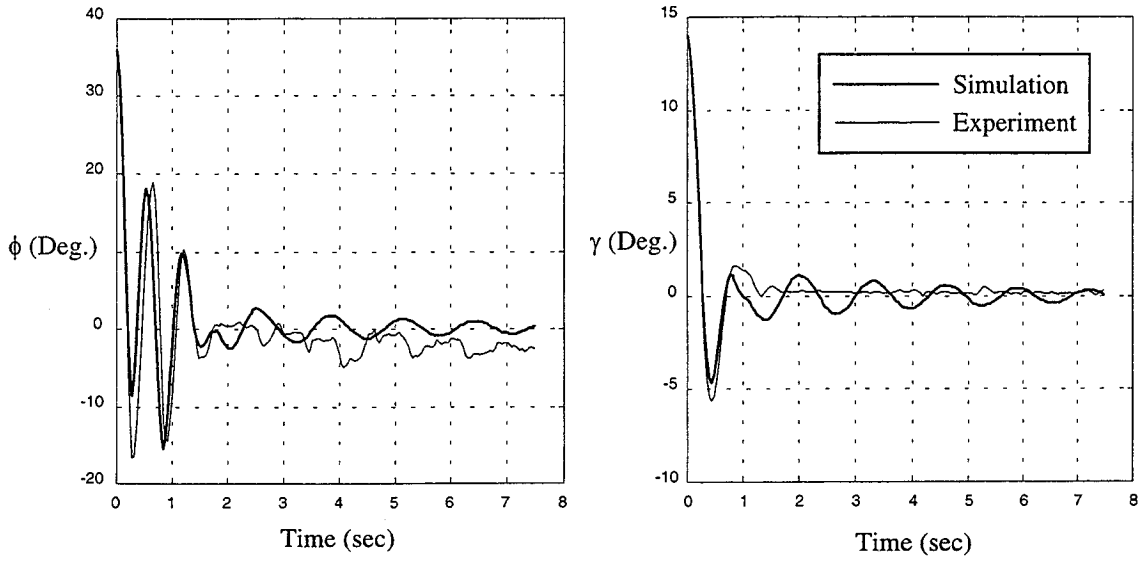

Figure 6.7: Response of closed-loop system to initial condition. Control strategy given by Equation 6.6 with $C_{\mu_{MIN}} = 0.01$.

Comparison of experimental data and results from the simulation indicate that the aerodynamic model captures the characteristics of the motion but quantitative differences exist. A possible cause of these differences is that a small leakage occurred on the left valve. This can be seen in Figure 6.8 where the measured values of C_μ are plotted as a function of time. Negative values are used to represent port side blowing. As shown, the value of C_μ never reached zero for the left side which indicates a leakage on the left valve. Although small, the leakage causes differences in the roll and yaw moments that were not accounted for in the aerodynamic model.

The peak and average values of C_μ provide a good measure of the control effort required to stabilize the system. These values, computed for the length of the time history shown in Figure 6.8, are summarized in Table 6.5.

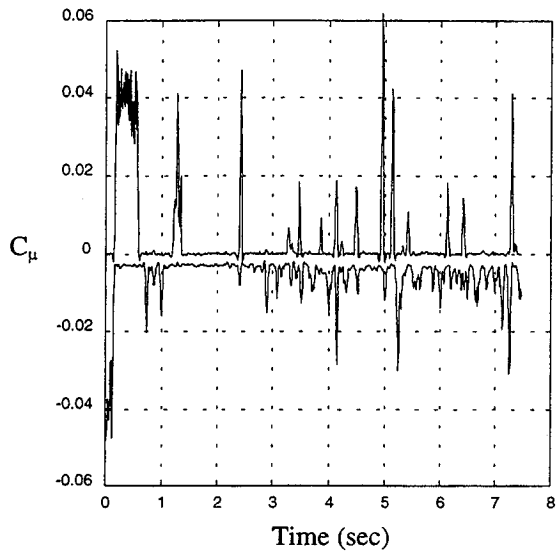

Figure 6.8: Control effort during closed-loop response to initial condition. Control strategy given by Equation 6.6 with $C_{\mu_{MIN}} = 0.01$. $C_\mu > 0$ for starboard blowing and $C_\mu < 0$ for port side blowing.

Although the peak values of C_μ are relatively high, the plot in Figure 6.8 shows that these values were applied during very short time intervals, this is reflected in the very small average values. The mean of the left and right side average values of C_μ is 0.005 and gives a measure of the required air flow rate. This air flow rate is within the capabilities of current fighter aircraft if air is bleed from the engines [44].

	Peak Value	Average Value[1]
$\|C_{\mu_R}\|$	0.062	0.0038
$\|C_{\mu_L}\|$	0.048	0.0059

Table 6.5: Control effort required to stabilize the model in two degrees-of-freedom.

[1] Computed for time between 0 and 7.5 seconds, Figure 6.8.

As mentioned previously in this chapter, superimposed symmetric and asymmetric blowing can also be used to control the system with the advantage that the characteristics of actuator are linearized by the physics of the flow and the resulting closed-loop system would probably be more robust. As seen in Chapter 3, significant linearization occurs for $C_{\mu_{SYM}} \cong 0.01$, if this value is used the mean value of C_μ results larger than 0.02. This value is four times the one required if only asymmetric blowing is used.

6.6 Summary

A control approach was developed that uses forebody tangential blowing as the only actuator to control the roll-yaw motion of a wind tunnel model at high angle of attack. The designed closed-loop control logic was demonstrated experimentally in the wind tunnel using a unique two degrees-of-freedom apparatus. The closed-loop system is stable in contrast to the open-loop system which presents a divergent motion.

In developing the control logic, a linearized version of the equations of motion was used. Although linearization of the actuator characteristics can be achieved by superimposing symmetric and asymmetric blowing, this strategy was not used because of its larger demand for air. Instead, an asymmetric blowing strategy was devised that allows the linearization of the roll and yaw moment responses to blowing. A linear quadratic regulator design was used to obtain the closed-loop gain vector. This control design assumes full knowledge of the states, but measurements were available only for the two degrees-of-freedom, ϕ and γ. For real-time implementation, the other elements of the state vector were estimated from the measurements of ϕ and γ and the linearized equations which describe the system dynamics.

Results from the simulation captured the general characteristics of the closed-loop response obtained experimentally, but quantitative differences are observed which are attributed to experimental difficulties associated with bringing the blowing to zero (due to leakage in one of the servo-valves).

~

Chapter 7

Conclusions

In this final chapter the results of this research are summarized and the main conclusions of the study presented. Recommendations for future research are included motivated by the findings of this work and the need for advancement in aircraft control at high angles of attack.

7.1 Summary of Results

In this research the feasibility of using forebody tangential blowing to control the roll-yaw motion of aircraft has been demonstrated. Specifically the high angle of attack regime has been investigated using a delta wing-body wind tunnel model and a novel apparatus that allows roll and yaw degrees-of-freedom. Research contributions were presented in Chapter 1. Following is a summary of results and conclusions.

7.1.1 Aerodynamics

Flow Structure: The unique attributes of the high angle-of-attack aerodynamics over the delta wing-body wind tunnel model have been determined through flow visualization and measurement of the aerodynamic loads. Flow asymmetries that start at the forebody determine the structure of the flow downstream. In particular, for the current configuration, a dominant three-vortex structure was observed for stations where the wing

was present. This stable asymmetric flow structure can be changed to its mirror-image configuration by a change in roll angle. This fact is attributed to geometric imperfections on the tip of the forebody. The flow structure is less affected by changes in the yaw angle. As a result of the flow asymmetry, large roll and yaw moments are present even for the model at wings level and zero-side slip angle.

Asymmetric FTB: The dominant three-vortex structure can be changed into its mirror-image configuration by asymmetric forebody tangential blowing. A minimum amount of blowing is required to cause this change. The effect of asymmetric FTB on roll and yaw moments is highly non-linear, specially for small amount of blowing. These experimental observations correlate well with a numerical study by Degani [21, 22], indicating that a small amount of blowing has a similar effect as the minute geometric imperfections on the forebody tip and triggers a convective-type instability of the flow.

Symmetric FTB: Application of symmetric forebody tangential blowing brings symmetry to the flow. The dominant three-vortex structure over the wing is replaced by a more symmetric two-vortex structure. Also, lateral load alleviation is achieved for relatively small values of symmetric blowing. Moreover, it was demonstrated that roll and yaw moment dependence on blowing can be made approximately linear by superimposing symmetric and asymmetric blowing.

Transient Response to FTB: The roll and yaw moment responses to a step input blowing have been characterized in terms of time constants, $\tau_\phi = 0.018$ and $\tau_\gamma = 0.005$ seconds respectively. Their comparison with a characteristic convective time of 0.016 seconds was used to explain the different mechanisms through which roll and yaw moments are generated. For the delta wing-body model, roll moment is generated mainly on sections where the wing is present because the fuselage is of circular cross-section and the direct jet momentum small. The small value of τ_γ as compared to τ_ϕ indicates that the wall-jet effect and the reattachment of the flow on the region of the slot are important mechanisms in the creation of yaw moment.

Steady State Aerodynamics: The discrete vortex method, developed in Chapter 4, has proven to be a useful tool in helping understand the interaction between forebody and wing vortices. It provides good qualitative results regarding the flow structure and correctly predicts the trends in the static aerodynamic loads. The dominant three-vortex structure observed experimentally can be obtained using the discrete vortex method by forcing asymmetric separation on a few sections of the forebody. The use of the method as a prediction tool is limited by the fact that flow structure and aerodynamic loads are strongly dependent on minute geometric imperfections on the forebody tip and small asymmetries in the upstream flow. This fact poses a limitation even for more sophisticated numerical methods.

Aerodynamic Model for Controls: The unique goals of this research required the development of an aerodynamic model suitable for controls. In particular, the model form had to be amenable for use in control law design and its real-time implementation in the wind tunnel. These requirements translated into the need for a method to calculate the loads that was both fast and that incorporated the main non-linear and transient aerodynamic effects. To meet these needs, a semi-empirical model was developed for the unsteady aerodynamic loads. The structure of the model was formulated based on the results of flow visualization experiments, measurements of the static loads, and basic physical representation of the main dynamic effects. The static aerodynamic loads are an integral component of the aerodynamic model. Parameters of the model characterizing the transient effects were determined from dynamic experiments. Results from simulations are in agreement with measured responses of the system.

7.1.2 Control Approach

The need for control was demonstrated through dynamic experiments which showed that the two degrees-of-freedom system was unstable and presented a divergent motion. Moreover, the only available actuator was forebody tangential blowing since the wind tunnel model had no movable control surfaces.

To investigate the control problem, the semi-empirical aerodynamic model was incorporated into the equations of motion of the system and the resulting equations were written in a form appropriate for use in a control framework. In particular, two control approaches have been devised that validate the inclusion of blowing as an incremental effector. It was demonstrated that linearization is not possible for arbitrary values of roll angle, yaw angle and blowing. Conditions under which linearization, with respect to roll and yaw angles, is applicable have been presented.

It was shown that, in general the characteristics of the vehicle depend on the blowing intensity, and the effect of blowing depend on the roll and yaw angles. As a consequence the equations of motion of the system are of the form $\dot{x} = f(x,u)$.

Asymmetric Minimum Blowing: In this case small values of blowing were avoided by applying a minimum amount of asymmetric blowing. This transformed the highly non-linear characteristics of blowing into a simpler non-linear characteristic. Also, if the roll and yaw angles are limited to a certain region, the characteristics of the vehicle can be assumed constant and the effect of blowing independent of the roll and yaw angles. It was shown that under these conditions the equations of motion can be simplified to $\dot{x} = f(x) + g(u)$ and linearized. A linear quadratic regulator (LQR) design was performed using the linearized equations. It was experimentally demonstrated that the designed closed-loop control logic stabilized the system and regulated roll and yaw angles to close to zero. Disturbance rejection was also demonstrated and results from simulation agree with closed-loop experimental data.

Symmetric Blowing: This control strategy relies on superimposing symmetric and asymmetric blowing. It was demonstrated that this technique has the effect of linearizing the actuator characteristics. It was shown that for a limited range of roll and yaw angles the characteristics of the vehicle can be assumed independent of blowing and the equations of motion linearized. This control strategy was not pursued in detail in this research because of its larger use of air when compared to the asymmetric blowing case.

7.2 Recommendations for Future Work

The results of this research represent one step towards enabling the ultimate goal of aircraft control at high angles of attack. In this context several areas have been identified in which further investigation is required.

Large Angle Maneuvers: The results presented in this dissertation pertaining to control are limited to regulation. The possibility of commanding roll and yaw angles is a logical next step. In particular, the feasibility of large angle command should be investigated as it translates directly into increased maneuverability of the vehicle.

Small Blowing Rates: As shown, large roll and yaw moments are generated by small amounts of asymmetric blowing. The control laws developed in this research avoid this region of small blowing values because of its highly non-linear characteristics. The use of more sophisticated control approaches, such as adaptive and robust control, should be explored as a means to investigate the possibility of operation in this region.

Degrees-of-Freedom: This work has addressed the case of two degrees-of-freedom, roll and yaw. The six degrees-of-freedom case represents the final objective. It is known that FTB affects the pitch moment, as well as the forces acting on the vehicle. A study encompassing additional degrees-of-freedom is necessary before FTB can be used in real aircraft.

Various Flight Conditions and Different Configurations: In this study, aerodynamics and control issues have been addressed at a nominal angle of attack of 45 degrees, and specific Reynolds and Mach numbers. Investigation of the effects of angle of attack, Reynolds number and Mach number are necessary to determine the applicability and limitations of the methods developed. Similarly, different aircraft configurations should be investigated. Of particular interest are the effects of adding a vertical stabilizer and varying the wing sweep angle.

Interaction with Control Surfaces: Forebody tangential blowing is proposed as an extra actuator to increase vehicle controllability in the high angle of attack regime. The integration of FTB into aircraft control system requires a study to determine its effects on conventional control surfaces.

Appendix A

Wind Tunnel Model Characteristics

The dimensions and mass properties of the wind tunnel model are summarized in this appendix. Also included are the detailed geometry of the slots used to create the tangential blowing on the forebody.

A.1 Dimensions

The detailed dimensions of the wind tunnel model used in the experiments are shown in Figure A.1. Dimensions are in inches unless otherwise specified. The blunt forebody tip, used in some of the experiments, consists of a semi-sphere of radius equal to 0.00762 m (0.3 inches) and is show as a dotted line. The point at which the γ-axis intersects the longitudinal axis of the model is labeled point P and its location is shown in the drawing, as well as the location of the center of mass of the model (C.M.). The mean aerodynamic chord, MAC, shown in the figure is defined as:

$$MAC = \frac{1}{S_{ref}} \int_{-b/2}^{b/2} c^2_{(y)}\, dy \qquad (A.1)$$

where c(y) is the local chord, b is the wing span, and S_{ref} is the wing plan form area obtained by extending the wing leading and trailing edges into the fuselage. For a delta wing,

$$S_{ref} = c(0)\frac{b}{2} \tag{A.2}$$

Relevant geometric characteristics of the model are summarized in Table A.1.

Characteristic	Value
conical forebody semi-apex angle	14 deg
wing leading-edge sweep angle, Λ	70 deg
wing span, b	5.50 in
wing plan form area, S_{ref}	20.68 in^2
wing aspect ratio, $AR = b^2/S_{ref}$	1.46
mean aerodynamic chord, MAC	5.01 in
spanwise location of MAC	0.92 in
position of center of mass of the model	0.24 MAC
position of point P	0.44 MAC
model plan form area	25.19 in^2
tunnel blockage for $\alpha_0 = 45$ degrees	7%
tunnel blockage for $\alpha_0 = 90$ degrees	10%

Table A.1: Geometric characteristics of the wind tunnel model.

As indicated in Figure A.1, slots are present both at the conical and cylindrical portions of the forebody. For the experiments reported in this work, the portion of the slots located on the cylindrical portion of the forebody were not used, *i.e.* the slots were partially blocked and as a result blowing was only applied at the conical portion of the forebody.

On the cylindrical section, the slots have uniform width, given by $w_{cyl}/D = 0.0087$, where $D = 1.5$ inches is the diameter of the fuselage. On the conical section, the slots are tapered, their maximum width is $w_{max}/D = 0.0087$. The minimum width is $w_{min}/D = 0.0062$ and occurs at a station located 0.3 inches from the tip of conical forebody. The effective area of each slot, *i.e.* the area of the slot located at the conical portion of the forebody is 0.0207 in^2.

A.2 Mass Properties

The mass of the wind tunnel model is 0.6420 ± 0.0001 Kg. The model is built from aluminum 6061-T6 and anodized black to minimize reflections of the laser sheet used during flow visualization experiments. The inertia of the model with respect to a reference frame XYZ oriented as shown in Figure A.1 and with origin at the center of mass of the model was determined experimentally using a torsional pendulum [45]. Results are presented in Table A.2 which also includes the values of the inertia terms for the case where the origin of the reference frame is at point P.

Inertia Component ($Kg\ m^2$)	Origin of Reference Frame	
	C.M.	Point P
I_{XX}	$(1.76 \pm 0.09) \times 10^{-4}$	$(1.76 \pm 0.15) \times 10^{-4}$
I_{YY}	$(2.79 \pm 0.04) \times 10^{-3}$	$(3.19 \pm 0.05) \times 10^{-3}$
I_{ZZ}	$(2.83 \pm 0.01) \times 10^{-3}$	$(3.22 \pm 0.02) \times 10^{-3}$
I_{XY}	0	0
I_{XZ}	≈ 0	≈ 0
I_{YZ}	0	0

Table A.2: Inertia properties of the wind tunnel model.

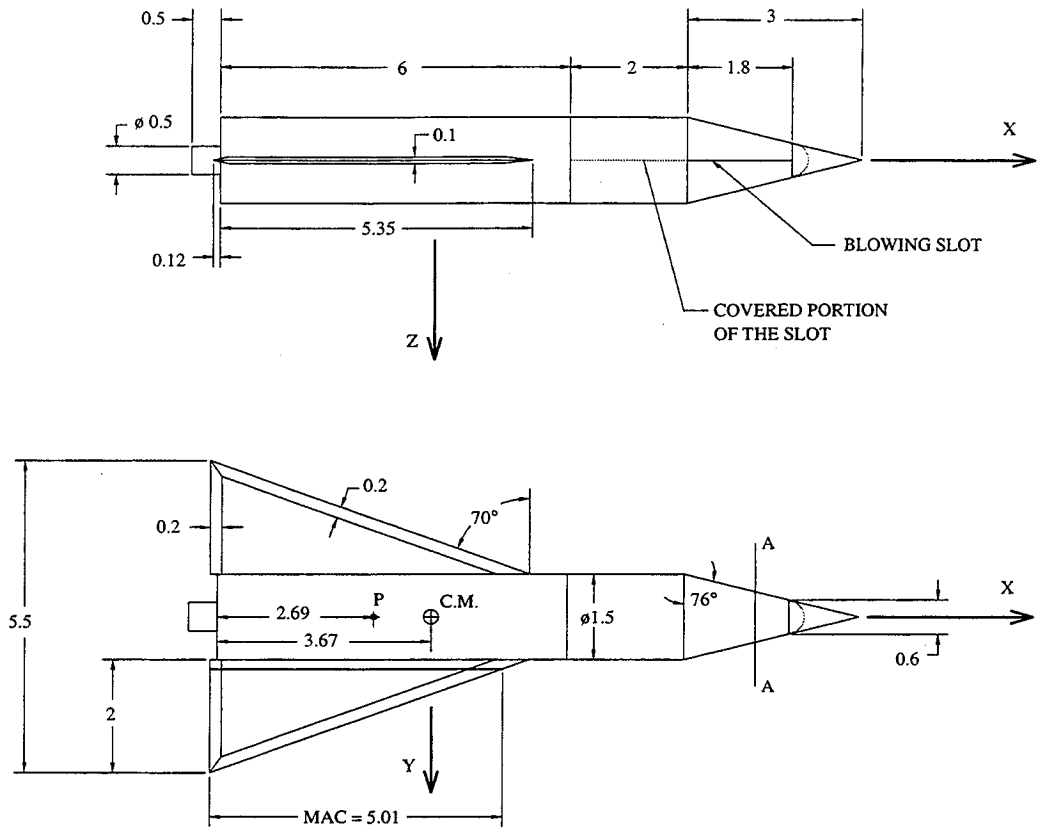

CROSS-SECTION AA

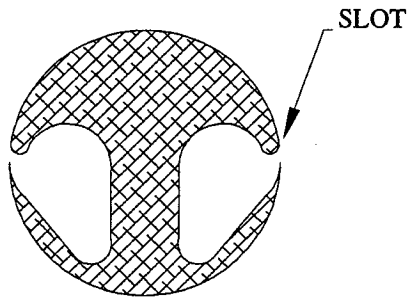

Figure A.1: Geometry of the wind tunnel model. Dimensions are in inches.

Appendix B

Model Support System Characteristics

In this appendix the values of the parameters used to characterize the two degrees-of-freedom model support system are given. A summary of all sensors and actuators used in the apparatus with references to further documentation is also presented. A general description of the system including conceptual design, main system components and performance evaluation is presented in Chapter 2. Detailed mechanical design drawings and data on the calibration of the various sensors and actuators are not included in this appendix, those can be found in Reference [19].

B.1 Dimensions and Mass Properties

The main components of the roll system are shown in Figure B.1. All parts are made of aluminum 6061-T6 except for the roll shaft and the bearings which are made of steel. The roll shaft is mounted on bearings to allow rotation about the longitudinal axis of the model. The inertia of the moving parts about the ϕ-axis excluding the model is labeled I_{ϕ}^{R} and is listed in Table B.1. It includes contributions from the roll shaft, bearings, collars, fixtures, potentiometer and air supply tubing. The total inertia in roll is obtained by

adding to this value the inertia of the model which is given in Appendix A. The resulting total inertia about the ϕ-axis is equal to 2.61×10^{-4} Kg m^2.

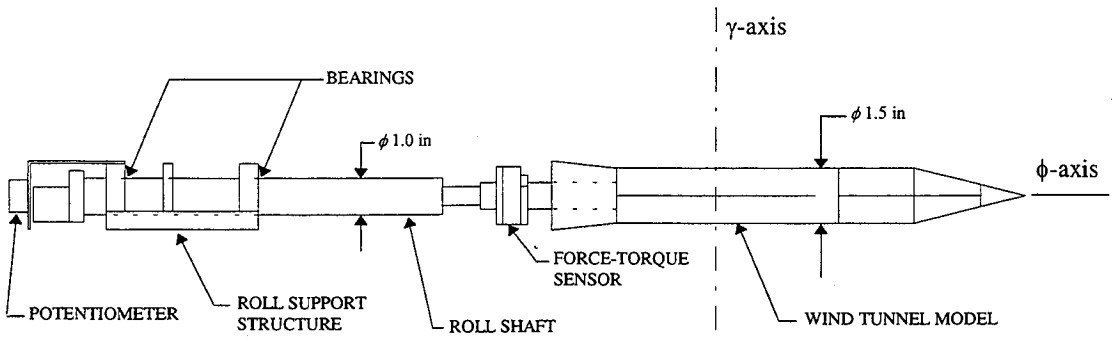

Figure B.1: Implementation of rotation about the ϕ-axis.

Characteristic	Value	Units
I_ϕ^R	$(8.4 \pm 0.5) \times 10^{-5}$	Kg m^2
m_S	3.91 ± 0.01	Kg
d_{CM}^S	$(119.6 \pm 0.8) \times 10^{-3}$	m
I_γ^S	$(155.8 \pm 1.0) \times 10^{-3}$	Kg m^2
C_F	$(1.1 \pm 0.3) \times 10^{-3}$	Nm sec
D_F	$(8.5 \pm 2.6) \times 10^{-3}$	Nm sec

Table B.1: Main parameters of the model support system.

Figure B.2 illustrates the implementation of the second degree-of-freedom. Rotation about the γ-axis is made possible by a mechanical assembly consisting of two co-axial shafts connected through bearings. The inner shaft can rotate while the outer shaft is fixed to the test section. The yaw support structure is connected to the inner shaft and can rotate about the γ-axis. In the figure the location of the bearings and of the torque sensor are

indicated by shaded areas. The gravity restoring moment about the γ-axis due to the support system is given by:

$$M_{\gamma}^{G}\Big|_{S} = -m_S g\, d_{CM}^{S} \sin(\gamma) \tag{B.1}$$

Where the quantities in the equation refer to a system S formed by the moving parts of the support system about the γ-axis, *i.e.* m_S is the mass of the moving parts of the support system and does not include the model and d_{CM}^{S} is the distance from the center of mass of S to the γ-axis. In the equation, g represents the acceleration of gravity. In Figure B.2 the center of mass of S is at some point on line CC. Measured values for m_S and d_{CM}^{S} as well as for the inertia of the support system about the γ-axis, I_{γ}^{S}, are given in Table B.1. Also included are the values of the friction coefficients C_F and D_F defined in Chapter 2[1], to approximate the effect of friction on the bearings and potentiometers.

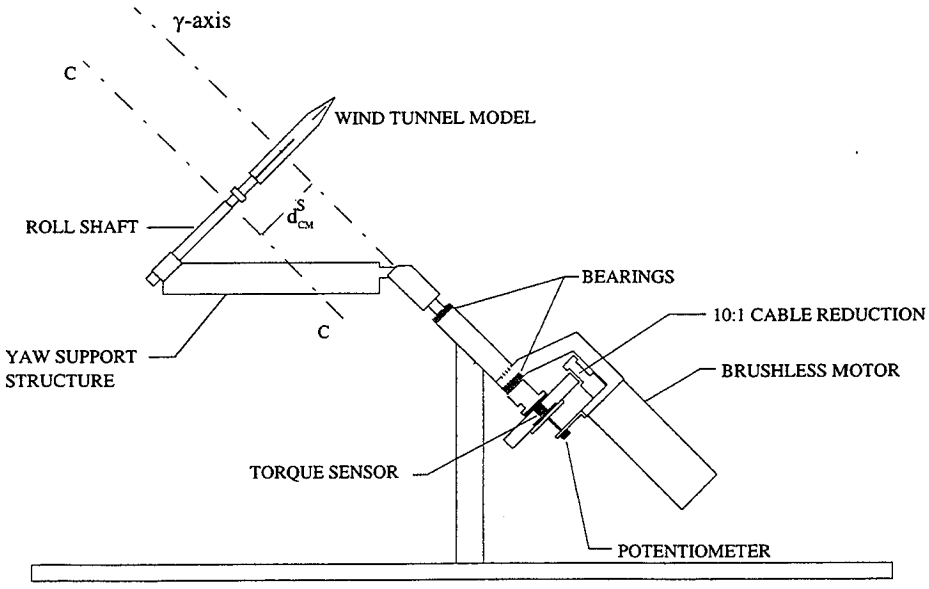

Figure B.2: Implementation of rotation about the γ-axis

[1] Section 2.3.2.

B.2 Sensors and Actuators

Table B.2 contains a list of the sensors and actuators which are an integral part of the experimental apparatus. Details on sensor and actuator physical properties, calibration and linearity can be found in Reference [19].

Measured Quantity	Sensor
Degrees-of-freedom, ϕ and γ	Precision potentiometer MKV-F78S. Conductive plastic RESISTOFILM®. New England Instrument Company. Woonsocket, RI 02895-1129.
Angular acceleration, $\ddot{\gamma}$	Systron Donner 4310A-1-P116 Linear Servo Accelerometer. Systron Donner Company. Inertial Division. Concord, CA 94518.
Blowing coefficient, C_μ	Custom designed flowmeters.
Torque applied to the γ-axle	Custom designed torque sensor.
Loads acting on the model	Mini 90N/4.2Nm. Serial #FT3253. Assurance Technologies, Inc. Garner, NC 27529.

Application	Actuator
Air injection	Servo valves designed by Wong [9].
Torque cancellation	Electro-Craft® Brushless Servo System: DM-30 drive, S-4075-R-H00AA motor. Reliance Motion Control, Inc. Enden Prairie, MN 55344.

Table B.2: List of sensors and actuators used in the experimental apparatus.

Appendix C

Parameter Identification Method

The parameter identification method used in Chapter 5 is presented in this appendix. The method consists of a standard non-linear least squares algorithm.

C.1 Least Squares

Consider the vector $\mathbf{V} = [\mathbf{v}_1\ \mathbf{v}_2\ \mathbf{v}_3\ \ldots\ \mathbf{v}_m]^T$ and the known measurements of the variables at instants $t_1, t_2, \ldots t_n$

$$\mathbf{v}_k = \mathbf{v}(t_k) = [v_1(t_k)\ \ v_2(t_k)\ \ \ldots\ v_m(t_k)]^T \qquad 1 \le k \le n \tag{C.1}$$

Let $\mathbf{f}(t, \mathbf{p})$ be a mathematical representation of $\mathbf{v}$, where $\mathbf{p} = [p_1\ p_2\ \ldots\ p_p]^T$ is a vector of parameters which defines the mathematical model. Using $\mathbf{e}(t_k,\mathbf{p})$ to represent the equation errors results,

$$\mathbf{v}(t_k) = \mathbf{f}(t_k,\mathbf{p}) + \mathbf{e}(t_k,\mathbf{p}) \tag{C.2}$$

If it is assumed that the function $\mathbf{f}$ is linear in the parameters then

$$\mathbf{f}(t,\mathbf{p}) = \mathbf{F}(t)\,\mathbf{p} \tag{C.3}$$

And the solution to the least squares problem is given by:

$$\mathbf{p}_{LS} = (\mathfrak{I}^T \mathfrak{I})^{-1} \mathfrak{I}^T \mathbf{V} \tag{C.4}$$

Where $\mathfrak{I} = [\mathbf{F}(t_1)\ \mathbf{F}(t_2)\ \ldots\ \mathbf{F}(t_n)]^T$ has nm rows and p columns and $\mathbf{V} = [\mathbf{v}(t_1)\ \mathbf{v}(t_2)\ \ldots\ \mathbf{v}(t_n)]^T$ is a column vector with nm rows containing the measurements of $\mathbf{v}$ at the n time instants. The parameter vector $\mathbf{p}_{LS}$ minimizes the sum of the errors squared, J_e, defined as:

$$J_e = \sum_{k=1}^{n} \mathbf{e}^T(t_k, \mathbf{p})\, \mathbf{e}(t_k, \mathbf{p}) \tag{C.5}$$

C.2 Non-Linear Least Squares

If $\mathbf{f}(t,\mathbf{p})$ is not a linear function of the parameters the problem can be formulated by considering the first order expansion of the function $\mathbf{f}$.

$$\mathbf{f}(t,\mathbf{p}) = \mathbf{f}(t,\mathbf{p}_0) + \left.\frac{\partial \mathbf{f}}{\partial \mathbf{p}}\right|_{\mathbf{p}_0} \delta\mathbf{p} + \varepsilon(t,\mathbf{p}_0) \tag{C.6}$$

where $\delta\mathbf{p} = \mathbf{p} - \mathbf{p}_0$ and $\varepsilon(t,\mathbf{p}_0)$ is the error due to the exclusion of higher order terms.

Defining $\mathbf{w}(t,\mathbf{p}_0) \equiv \mathbf{v}(t) - \mathbf{f}(t,\mathbf{p}_0)$, results:

$$\mathbf{w}(t,\mathbf{p}) = \left.\frac{\partial \mathbf{f}}{\partial \mathbf{p}}\right|_{\mathbf{p}_0} \delta\mathbf{p} + \varepsilon(t,\mathbf{p}_0) \tag{C.7}$$

The above equation is similar to Equation C.2 and can be solved in the least squares sense for $\delta\mathbf{p}$,

$$\delta\mathbf{p}_{LS} = (\Upsilon^T \Upsilon)^{-1} \Upsilon^T \mathbf{W} \tag{C.8}$$

Where $\Upsilon = [\partial \mathbf{f}/\partial \mathbf{p}(t_1,\mathbf{p}_0)\ \ \partial \mathbf{f}/\partial \mathbf{p}(t_2,\mathbf{p}_0)\ \ldots\ \partial \mathbf{f}/\partial \mathbf{p}(t_n,\mathbf{p}_0)]^T$ has nm rows and p columns and the column vector $\mathbf{W} = [\mathbf{w}(t_1)\ \mathbf{w}(t_2)\ \ldots\ \mathbf{w}(t_n)]^T$ has nm rows. The parameter vector $\delta\mathbf{p}_{LS}$ minimizes the sum of the errors squared, J_ε , defined as:

$$J_\varepsilon = \sum_{k=1}^{n} \varepsilon^T(t_k,\mathbf{p})\,\varepsilon(t_k,\mathbf{p}) \tag{C.9}$$

In this case $\mathbf{w}$ and $\partial \mathbf{f}/\partial \mathbf{p}$ are functions of $\mathbf{p}_0$ and iterations are required until convergence is achieved for the parameter $\mathbf{p}$. Matrix $\partial \mathbf{f}/\partial \mathbf{p}(t_k,\mathbf{p}_0)$ has m rows and p columns and its elements are obtained by varying one parameter at a time by an amount Δp_j and calculating the partial derivatives numerically. Once $\delta\mathbf{p}_{LS}$ is obtained according to Equation C.8 the value of $\mathbf{p}_0$ is updated as follows:

$$\mathbf{p}_0\big|_{i+1} = \mathbf{p}_0\big|_i + \xi\,\delta\mathbf{p}_{LS} \tag{C.10}$$

where i indicates the iteration number and ξ is a scalar chosen in association with the disturbances Δp_j to assure convergence.

~

Bibliography

[1] Ericson, L. E. and Reding, J. P., "Alleviation of Vortex Induced Asymmetric Loads," Journal of Spacecraft and Rockets, Vol. 17, Nov.-Dec. 1980, pp. 546-553.

[2] Rao, D. M., Moskovitz, C. and Murri, D. G., "Forebody Vortex Managements for Yaw Control at High Angles of Attack," Journal of Aircraft, Vol. 24, No. 4, April 1987, pp. 248-254.

[3] Wood, N. J. and Roberts, L., "Experimental Results of the Control of a Vortical Flow by Tangential Blowing," NASA JIAA TR-71, Stanford University, May 1986.

[4] Wood, N. J. and Roberts, L., "Control of Vortical Lift on Delta Wings by Tangential Leading-Edge Blowing," Journal of Aircraft, Vol. 25, No. 3, March 1988, pp. 236-243.

[5] Wood, N. J., Roberts, L. and Celik, Z. Z., "Control of Asymmetric Vortical Flows over Delta Wings at High Angles of Attack," Journal of Aircraft, Vol. 27, No. 5, May 1990, pp. 429-435.

[6] Yeh, D. T., Tavella, D. A. and Roberts, L., "Numerical Simulation of the Flowfield over Delta Wings with Leading Edge Blowing," Ph.D. Thesis, Department of Aeronautics and Astronautics, Stanford University, Stanford CA, 1988.

[7] Craig, K. J., "Computational Study of the Aerodynamics and Control by Blowing of Asymmetrical Vortical Flows over Delta Wings," Ph.D. Thesis, Department of Aeronautics and Astronautics, Stanford University, Stanford CA, August 1993.

[8] Mittelman, Z., "Prediction of Unsteady Aerodynamics and Control of Delta Wings with Tangential Leading Edge Blowing," Ph.D. Thesis, Department of Aeronautics and Astronautics, Stanford University, Stanford CA, June 1989.

[9] Wong, G. S., "Experiments in the Control of Wing Rock at High Angle of Attack Using Tangential Leading Edge Blowing," Ph.D. Thesis, Department of Aeronautics and Astronautics, Stanford University, Stanford CA, December 1992.

[10] Wong, G. S., Rock, S. M., Wood, N. J. and Roberts, L., "Active Control of Wing Rock Using Tangential Leading-Edge Blowing," Journal of Aircraft, Vol. 31, No. 3, May-June 1994.

[11] Skow, A. M., Moore, W. A. and Lorincz, D. J., "Forebody Vortex Blowing - A Novel Control Concept to Enhance Departure/Spin Recovery Characteristics of Fighter and Trainer Aircraft," AGARD CP-22, No. 24, May 1979, pp. 24-1 to 24-17.

[12] Celik, Z. Z. and Roberts, L., "Vortical Flow Control on a Slender Body at High Angles of Attack," AIAA Paper 91-2868, 1991.

[13] Celik, Z. Z. and Roberts, L., "Aircraft Control at High-Alpha by Tangential Blowing," AIAA Paper 91-0021, 1991.

[14] Celik, Z. Z. and Roberts, L., "Vortical Flow Control on a Wing-Body Combination Using Tangential Blowing," AIAA Paper 92-4430, 1992.

[15] Celik, Z. Z., Roberts, L. and Pedreiro, N., "The Control of Wing Rock by Forebody Blowing," AIAA Paper 93-3685, 1993.

[16] Celik, Z. Z., Roberts, L. and Pedreiro, N., "Dynamic Roll and Yaw Control by Tangential Forebody Blowing," AIAA Paper 94-1853, 1994.

[17] Font, G. I., "Tangential Fuselage Blowing on an Ogive Cylinder," Ph.D. Thesis, Department of Aeronautics and Astronautics, Stanford University, Stanford CA, June 1992.

[18] Adams, R. J., Buffington, J. M. and Banda, S. S., "Active Vortex Flow Control for VISTA F-1 Envelope Expansion," AIAA Paper 94-381, 1994.

[19] Pedreiro, N., "Development of an Apparatus for Wind Tunnel Dynamic Experiments at High-α," NASA JIAA TR-119, Stanford University, February 1997.

[20] Prandtl, L., and Tietjens, O. G., "Applied Hydro- and Aeromechanics," Dover Publications, Inc., New York, 1934.

[21] Degani, D., "Numerical Investigation of the Origin of Vortex Asymmetry,", AIAA Paper 90-0593, 1990.

[22] Degani, D., "Instabilities of Flows over Bodies at Large Incidence,", AIAA Journal, Vol. 30, No. 1, January 1992, pp. 94-100.

[23] Rom, J., "High Angle of Attack Aerodynamics," Springer-Verlag, New York, 1992.

[24] Sarpkaya, T., "Computational Methods With Vortices - The 1988 Freman Scholar Lecture," Journal of Fluids Engineering, Vol. 111, March 1989, pp. 5-52.

[25] Munk, M. M., "The Aerodynamic Forces on Airship Hulls," NACA Report No. 184, 1924.

[26] Jones, R. T., "Properties of Low-Aspect-Ratio Pointed Wings at Speeds Below and Above the Speed of Sound," NACA Report No. 835, 1946.

[27] Spreiter, J. R., "The Aerodynamic Forces on Slender Plane and Cruciform-Wing and Body Combinations," NACA Report No. 962, 1950.

[28] Ashley, H. and Landahl, M., "Aerodynamics of Wings and Bodies," Dove Publications, Inc., New York, 1985.

[29] Wedemeyer, E., "Vortex Breakdown," AGARD LS-121, March 1982.

[30] Hummel, D. and Srinivasan, P. S., "Vortex Breakdown Effects on the Low-speed Aerodynamic Characteristics of Slender Delta Wings in Symmetrical Flow," Journal of the Royal Aeronautical Society, Vol. 71, April 1967, pp. 319-322.

[31] Sacks, A. H., Lundberg, R. E. and Hanson, C. W., "A Theoretical Investigation of the Aerodynamics of Slender Wing-Body Conbinations Exhibiting Leading-Edge Separation," NASA CR-719, March 1967.

[32] Mendenhall, M. R. and Lesieutre, D. J., "Prediction of Vortex Shedding from Circular and Noncircular Bodies in Subsonic Flow," NASA CR-4037, 1987.

[33] Mendenhall, M. R., Perkins, S. C., Jr. and Lesieutre, D. J., "Vortex Cloud Model for Body Vortex Shedding and Tracking," Tactical Missile Aerodynamics: Prediction Methodology, edited by M. R. Mendenhall, Vol. 142, Progress in Astronautics and Aeronautics, AIAA, Washington, DC, 1992, pp. 225-285.

[34] Stratford, B. S., "The Prediction of Separation of the Turbulent Boundary Layer," Journal of Fluid Mechanics, Vol. 5, 1959, pp. 1-16.

[35] Milne-Thomson, L. M., "Theoretical Hydrodynamics," The Macmillan Company, New York, 1960.

[36] Bryson, A. E., Jr., "Stability Derivatives for a Slender Missile with Application to a Wing-Body-Vertical-Tail Configuration," Journal of the Aeronautical Sciences, Vol. 20, No. 5, 1953, pp. 297-308.

[37] Bryson, A. E., Jr., "Evaluation of the Inertia Coefficients of the Cross Section of a Slender Body," Journal of the Aeronautical Sciences, Vol. 21, No. 6, 1954, pp. 424-427.

[38] Skulsky, R. S., "A Conformal Mapping Method to Predict Low-Speed Aerodynamic Characteristics of Arbitrary Slender Re-Entry Shapes," Journal of Spacecraft and Rockets, Vol. 3, No. 2, Febuary, 1966.

[39] Kuette, A. M. and Chow, C. Y., "Foundations of Aerodynamics," John Wiley & Sons, Inc., 1986.

[40] Marshall, F. J. and Deffenbaugh, F. D., "Separated Flow Over Bodies of Revolution Using an Unsteady Discrete-Vorticity Cross Wake - Part I - Theory and Applications," NASA CR-2414, 1974.

[41] Mourtos, N. J., "Control of Vortical Separation on Conical Bodies,", Ph.D. Thesis, Department of Aeronautics and Astronautics, Stanford University, Stanford CA, 1987.

[42] Ng, T. T., Malcolm, G. N. and Lewis, L. C., "Flow Visualization Study of Delta Wings in Wing-Rock Motion," AIAA Paper 89-2187, 1989.

[43] Arena, A. S. and Nelson, R. C., "A Discrete Vortex Model for Predicting Wing Rock of Slender Wings," AIAA Paper 92-4497, 1992.

[44] Kroo, I. and Roberts, L., "Forebody Tangential Blowing for Control at High Angles of Attack - Feasibility Study Final Report," NASA JIAA TR-101, Stanford University, June 1991.

[45] Ims, S., "Inertia Measuring System," Stanford Aerospace Robotics Laboratory Memo 75, Stanford University, July 1991.